Identification of Stimulation waveforms for high C-fiber nerve selectivity for chronic neurological pain relief, and their gate mechanism and parameter analysis

August 2021

Siyu He

Graduate School of Engineering

CHIBA UNIVERSITY

（千葉大学審査学位論文）

Identification of Stimulation waveforms for high C-fiber nerve selectivity for chronic neurological pain relief, and their gate mechanism and parameter analysis

August 2021

Siyu He

Graduate School of Engineering

CHIBA UNIVERSITY

Abstract

With the aging of the population, treatment of chronic neurological pain is becoming an important field of neurology. Few investigations have been conducted on the selective stimulation of small-radius unmyelinated C nerves, which are critical to both the recovery of damaged nerves and chronic pain suppression. It has been reported that stimulating nociceptive unmyelinated C nerves near the sarcolemma could induce the secretion of endogenous opioids that relieve chronic pain. However, a substantial concern remains: concomitant stimulation might cause acute pain from nociceptive myelinated Aδ nerves, which generally have a lower activation threshold than the C nerves. It is difficult to stimulate the C nerves before the Aδ nerves by the percutaneous stimulus.

In this study, the C and Aδ nerves were modeled by two mathematical models to analyze the underlying ion dynamics and the influence of relevant stimulation waveforms. Three potential waveforms were analyzed, including 1) an anodal-first stimulation which reduces the threshold of C nerves; 2) a high frequency sine pre-stimulation which inhibits the excitability of the Aδ nerves; 3) a combination of the two stimulus waveforms. For the result, it was made clear that anodal-first polarity asymmetric stimulations are more likely to stimulate unmyelinated nerves because the preceding anodal stimulation could decrease their potassium ion current for the subsequent cathodal stimulation. On the other hand, high frequency sine pre-stimulations significantly increase the potassium ion current of the myelinated nerves. It makes the myelinated nerves more difficult to generate action potentials than unmyelinated nerves. Moreover, it has also been verified that carrier waves could help deep nerve stimulation. The optimal parameters for C nerves selective stimulation have been identified, remarkably benefiting the design of selective stimulation waveforms for long-term pain relief.

Acknowledgements

I would like to acknowledge all the people who have accompanied me in this journey and given their support during these five years.

First at all, I take this opportunity to express deepest gratitude to my advisor Professor Wenwei Yu for his time, motivation, and patience throughout the time. His immense knowledge and guidance helped me in all the time of research and also in writing this thesis. I would also be grateful to Professor Huang from Singapore University of Technology and Design for assisting in my research and publications. I would like to thank my review board members, Professor Nakagawa, Professor Shimomura, Professor Nakaguchi, and Professor Orita, for their comments for helping me accomplish my thesis.

I also want to thank to our laboratory's secretary Osugi. She supports in acquiring materials for research and helps my life in Japan.

I am grateful to Chiba University and its staff for enabling my research. Also, I give my gratitude to the financial support of China Scholarship Council.

I would like to thank Shozo Takamatsu for his help and support in my research. I also like to thank all our lab members, especially Enomoto, Tripanpitak, Yoshida, Tapio, Guo and Zhou, for giving their useful comments, ideas and providing a pleasant research environment.

Finally, I would like to thank my family for their support to complete my PhD in Japan.

List of Publications

Publications

- He S., Yoshida Y., Tripanpitak K., Takamatsu S., Huang S. Y., and Yu W. “Gate mechanism and parameter analysis of anodal-first waveforms for improving selectivity of C-fiber nerves”, Journal of Pain Research, volume 14, pages 1785-1807, June 2021.
- He S., Yoshida Y., Tripanpitak K., Takamatsu S., Huang S. Y., and Yu W. "A simulation study on selective stimulation of C-fiber nerves for chronic pain relief." IEEE Access, volume 8 pages 101648-101661, May 2020.
- He S., Gomez-Tames J., and Yu W. "Three-dimensional needle-tip localization by electric field potential and camera hybridization for needle electromyography exam robotic simulator." Medical Devices, volume 9, pages 143-150, Jun 2016.
- Tripanpitak K., He S., Sönmezışık I., Morant T., Huang S. Y., and Yu W. "Granger Causality-Based Pain Classification Using EEG Evoked by Electrical Stimulation Targeting Nociceptive Aδ and C Fibers". IEEE Access, volume 9, pages 10089-10106, Jan 2021.
- Gomez-Tames J., Fukuhara Y., He S., Saito K., Ito K., and Yu W. "A human-phantom coupling experiment and a dispersive simulation model for investigating the variation of dielectric properties of biological tissues". Computers in biology and medicine, volume 61, pages 144-149, Jun 2015.

Conferences

- He S., Gómez-Tames J., and Yu W. "Needle detection by electro-localization for a needle EMG exam robotic simulator." 2015 IEEE International Symposium on Medical Measurements and Applications (MeMeA) Proceedings. IEEE, 2015.
- He S., Tripanpitak K., and Yu W. "Selective Stimulation of C fibers for Chronic Pain Relief." 2020 IEEE International Conference on Computational Electromagnetics (ICCEM). IEEE, 2020.
- Imamoglu N., Gomez-Tames J., He S., Gu D. Y., Kita K., and Yu W. "Unsupervised muscle region extraction by fuzzy decision based saliency feature integration on thigh MRI for 3D modeling". In 2015 14th IAPR International Conference on Machine Vision Applications (MVA). IEEE, 2015.

Contents

List of Figures

List of Tables

List of Abbreviations

BMAC	Burst-modulated alternating current
BSW	Bipolar square waves
SNAPs	Sensory nerve action potentials
MRG	McIntyre, Richardson, and Grill model
HH	Hodgkin-Huxley model
MYSA	Myelin sheath attachment segments
FLUT	Fluted region segments
STIN	Stereotyped internode segments
FH	Frankenhaeuser, Huxley model
S-D	Strength-duration
ISI	Interstimulus interval
PAR	Polarity asymmetry ratio
A.F	Anode first
C.F	Cathode first
R_{th}	Ratio of the excitation threshold of C to that of Aδ.

Chapter 1
Introduction

In this chapter, I introduced the background, motivation, challenge and the objective for my doctor project. First, I introduced what chronic pain is and the conduction theory of the nerve which transfer chronic pain. Then, I summarized the motivation and challenge of this research. Next, I gave and discussed related research on nerve selective stimulation. Finally, I stated the objective and structure of this thesis.

1.1 Background

Pain was defined by International Association for the Study of Pain (IASP) as an unpleasant sensory and emotional experience associated with, or resembling that associated with, actual or potential tissue damage in 1979 [1]. It is useful as a signal to protect oneself. In general, pain will gradually diminish and disappear as the injury heals, this is defined as acute pain. On the other hand, the pain that did not disappeared after the injury heals is defined as chronic pain. Because the condition is poorly understood and minimally treatable using existing therapies [2], chronic pain is one of the significant factors that reduce patients' quality of life (QOL). The most notable feature of chronic pain is its uncontrolled continuous pain sensation even without external stimulation. Moreover, a survey showed that the retention rate of chronic pain increases with age [3]. In most countries, there are 9.6% people suffer from chronic pain [4]. In Japan, this value is as high as 22.5% [5]. For countries facing rapidly aging populations, the treatment of chronic pain is an essential medical and even social issue [6].

Chronic pain can be classified into two types according to the pathological mechanism: nerve injury pain and functional disease pain [7]. The nerve injury pain is caused by abnormal pain transmission and control mechanisms.

1.1.1 Sensory nerve conduction theory

The pain transmission is achieved by the conduction of action potentials on the afferent sensory nerves. The sensory nerve structure and action potential are defined as follow:

(1) Sensory nerve structure

The anatomy of peripheral nerves consists of nerve fibers, supporting connective tissue, and blood supply. Sensory neurons are the afferent limb of somatosensory neural pathways. The sensory neuron consists of a soma, axon, receptor and axon terminal.

The receptor is finger-like projections that receive sensory input and transmit the signal through the axon. The axon terminal has a similar structure but is used to send signals to a next receptor. There are different types of receptors for differing stimuli: thermoreceptors, mechanoreceptors, nociceptors, photoreceptors, and chemoreceptors. Nociceptors mainly include the C nerve (C) for chronic pain and the Aδ nerve (Aδ) for acute pain [8]. Different from Aδ, C does not have a myelin sheath structure, so it cannot transmit signals through saltatory conduction.

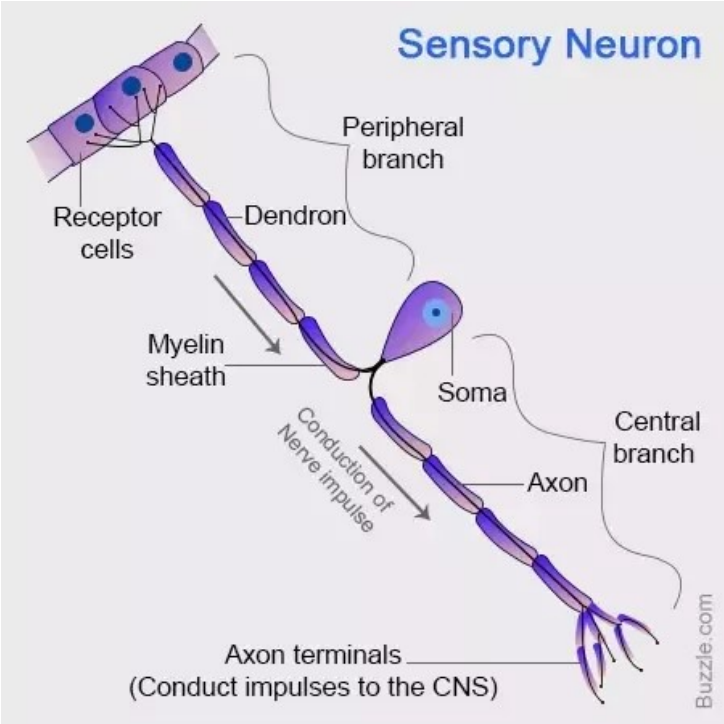

Figure 1.1 Sensory neuron structure [9]

(2) Action potential

Action potential provides a key role for cell-to-cell communication in nerves. It is generated by special types of voltage-gated ion channels embedded in a cell's plasma membrane [10]. In this study, there are three channels sodium channel, potassium channel and the current leakage for C, and four channels fast sodium channel, persistent sodium channel, slow potassium channel and the current leakage for Aδ.

Special attention was paid to the dynamics of each ion channel prior to the generation of action potential. In general, sodium channels start to open and most potassium channels keep closed when giving a stimulus smaller than the threshold strength. Potassium channels start to open after reaching the threshold [10]. This difference in

open time of ion channels causes nerves to generate an action potential.

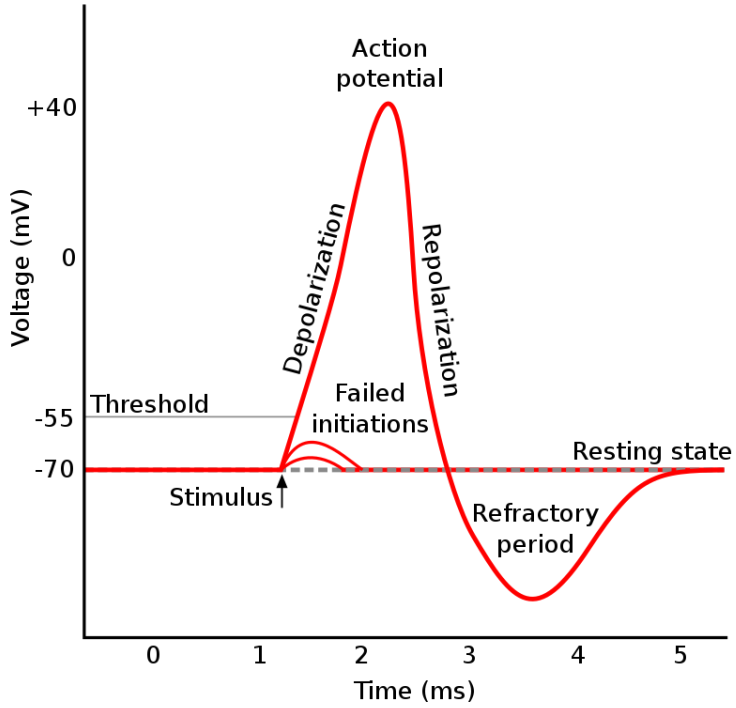

Figure 1.2 Action potential and its different phases [11].

1.1.2 Treatment methods for chronic pain

The treatment methods for patients with chronic pain include drug therapy, stimulation therapy and psychological therapy.

The total effect of psychological therapy still needs to be verified [6], even though it can improve pain treatment by, such as developing treatment willingness and good interpersonal relationships, to facilitate positive subjective attitudes [12]. Two main methods are available for chronic pain relief: 1) stimulation therapy (such as massage, physical therapy, and acupuncture) and 2) drug therapy [6]. For mild pain, stimulation therapy reduces pain by evacuation of substances that cause pain in the affected areas. For more severe pain, stimulation therapy can improve the inhibition of projection neurons that transmit noxious information by stimulating large-diameter non-nociceptive afferent nerves, such as Aβ, thereby blocking the signaling of nociceptive nerves and relieving the pain [13]. However, this treatment based on gate control theory cannot achieve a long-lasting analgesic effect. Generally, it is more effective to take medication for chronic pain treatment and use non-drug therapy to assist the medication. Opioid analgesics are used for very serious chronic pain, and highly

addictive, thus, likely to produce a broad spectrum of adverse effects [14].

It was reported in [15] that a pain immunity mechanism could cause spontaneous secretion of opioid substances which bind to opioid receptors to inhibit the transmission of strong pain signals into the brain. These opioid substances, which is called endogenous opioids, have the same analgesic effect as synthetic opioid drugs but lack addictive properties [15]. Later, researchers found that electroacupuncture stimulation could release endogenous opioids [16] and that needle electrodes could be used to stimulate peripheral nociceptive afferent nerves [17], prompting the nervous system to secrete opioids that act on the μ-receptor for analgesia [18]. Since then, treatments using laser [19], heat [20], and electrical stimulation [21] to induce endogenous opioids, called the endogenous opioid theory for sustained analgesia, have been developed. The following two facts are well documented.

1) Different endogenous opioid substances will be induced by different types of pain, and bind to their corresponding receptors [22]. Also, researchers found that different types of opioids were induced by different frequencies of stimulation in some needle stimulation studies. Especially, the μ-receptor with the strongest analgesic effect corresponds to low-frequency stimulation. Moreover, the most significant analgesic effects are produced by the stimulation of C fibers [22].

2) For pain suppression, compared with the other peripheral nerve endings in the skin surface, the nociceptive afferent nerves in deep tissues (such as tissues near the sarcolemma) play a decisive role [23].

Based on these two facts, the research of endogenous opioid using needle electrodes for the stimulation of deep tissue nerve fibers has progressed further ahead of other means of stimuli, e.g. using laser or heat. Using needle electrodes to stimulate the nerve fibers at deep tissue, such as the C near the sarcolemma, has been explored to achieve long-lasting analgesic effects (upon induction with μ-related opioids) [24]. However, trauma caused by persistent acute pain elicited by concomitant stimulation of Aδ (easier to stimulate than C) represents a concern for patients receiving treatment [24]. Moreover, the specific technical skills that can only be acquired with proper training are required for the needle stimulation for the treatment. Thus, it is difficult to push this pain relief technology into daily living use. It is necessary to develop new techniques along this direction to effectively and safely stimulate nerve fibers at deep tissue for endogenous opioid to have an accessible chronic pain relief. The research and progress of using needle electrodes will show insights and guidance to the development of the techniques using other kinds of stimuli.

1.2 Motivation and challenge

Concern for patients receiving treatment was represented by the trauma caused by persistent acute pain elicited by concomitant stimulation of Aδ fibers (Aδ) [24]. Moreover, the needle stimulation for the treatment requires specific technical skills which required by professional training. There is a great demand to push this pain relief technology into daily living use. However, to achieve the objective of selective stimulate the C nerve near the sarcolemma, which helps to secrete endogenous opioid, there are some challenges to be addressed.

1) As described before, most treatment requires specific technical skills, so that it is difficult to use into daily living. The environment for selective stimulation should be as simple as possible. Thus, the selective stimulation should be achieved by almost only changing the shape of waveform.
2) In generally, when being electrically stimulated, thick Aδ that has a diameter of 1.0-5.0 μm is more likely to be excited than thin C which is normally 0.2-1.5 μm in diameter. It is because that thicker myelinated nerves are much easily excited than the thin unmyelinated nerves [25] since the bigger membrane area reduces the equivalent resistance. Nevertheless, distinct properties of the ion channels of different nerve fibers maintain the possibility of selective stimulation of C (such as grill's research [26]).
3) The internal mechanism of C-selectivite stimulation is still unclear, and some conclusions are even contradictory. Therefore, this research aimed to study the mechanism of the C selectivity over the Aδ, and find the possibility of specific method of stimulation for high C selectivity through the analysis of their mechanism.

As mentioned above, chronic pain is an important social problem in countries with an aging population, the stimulation for high C selectivity is of great significance not only academically, but also commercially.

1.3 Related studies and problems

1.3.1 Interferential current therapy and carrier wave

Therapists often use transcutaneous electrical stimulation to treat their patients. However, direct current and low-frequency alternating currents (> 1 kHz) encounter a high electrical resistance in the outer layers of the skin. To stimulate deep tissues such as muscle, therapists use two waves of slightly different frequency to occur Interference (Figure 1.3) [27]. However, high-frequency bipolar stimuli make it difficult to stimulate C fibers. This technique is not suitable for inducing endogenous opioids [28].

Moreover, the influence of low-frequency wave modulated high-frequency waves, such

as "Russian electrical stimulation" [29], which is more recently known as burst-modulated alternating current (BMAC), on C-selectivity is unclear. This influence is attributed to the fact that high-frequency carrier waves may improve the penetration of stimulus to human skin [30]. Thus, carrier waves might solve another problem for real pain-relief applications via surface stimulation to C-fiber nerves near the sarcolemma.

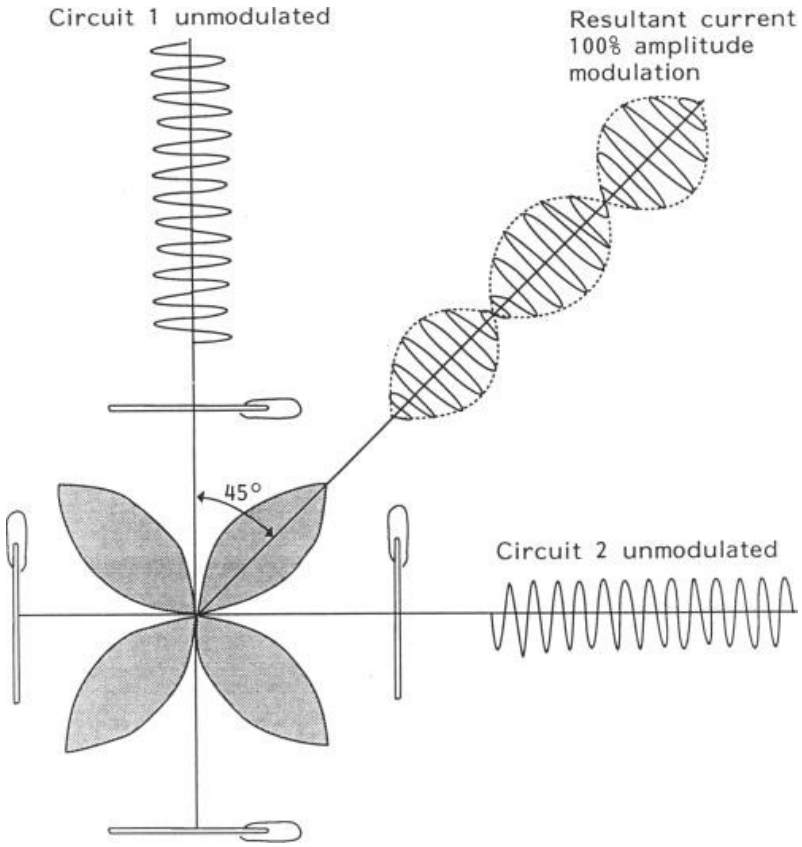

Figure 1.3 Interferential current therapy from [27]

1.3.2 Waveform for selectivity stimulation and anode break

As mentioned above, high-frequency bipolar stimuli difficult to stimulate C fibers. Neurometer (Neurotron, Baltimore, MD, USA) uses low frequency sine waves with frequencies of 2000, 250, and 5 Hz to stimulate Aβ, Aδ, and C fibers, respectively [28]. However, as has been noted, low-frequency sine waves cannot guarantee the selective stimulation of unmyelinated C fibers [31, 32]. In the low-frequency band, square waves exhibit better stimulating effects on unmyelinated nerves compared with sine waves with long pulse duration (> 8 ms) [33]. In [33], low-frequency bipolar square waves (BSW) are reported as an option for the stimulation for high C-selectivity .

The prepulsed stimulation which applies a preliminary stimulation to alter the states of

the neuromembrane and ion channel gate variables can change the activation threshold of a specific nerve responding to subsequent stimulations. A method called QTRAC© (Institute of Neurology, London) shows that a preceding cathodal pulse before a main cathodal stimulation can promote a reduction in the stimulation intensity for excitation (Figure 1.4) [34]. In 1995, a preceding square stimulation was proposed to change the neural excitation threshold of myelinated nerves, showing that cathodal prestimulation can suppress nerve excitability, and anodal prestimulation can promote nerve excitability [25]. However, the findings of the two studies on myelinated nerves are opposite. This contradiction might be caused by the different characteristics of their ion channel models. Along with this consideration, the unmyelinated fibers might show differences in response to a preceding stimulation. This has not been addressed so far in the literature and thus needs to be investigated systematically and compared with Aδ.

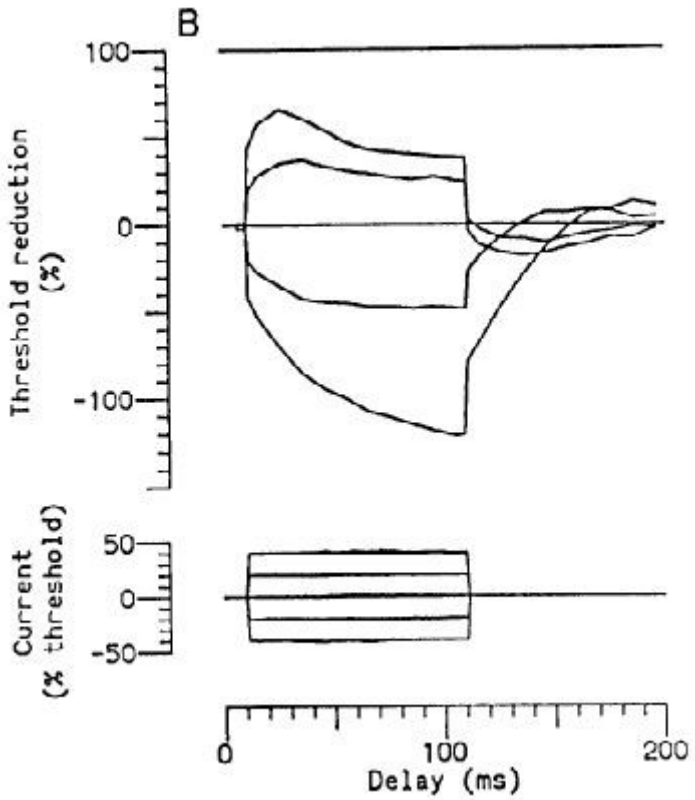

Figure 1.4 Threshold currents for five different stimulus conditions tracked in parallel from [34]. A preceding cathodal pulse before a main cathodal stimulation can promote a reduction in the stimulation intensity for excitation.

On the other hand, sensory nerve action potentials (SNAPs) can show two separate

deflections, i.e., double peak potentials, responding to nerve stimulation. Moreover, it has been discovered in animal experiments that only anodal stimulation can generate action potentials in tissues such as the myocardium, and this method is named anode break [35]. It was further investigated with an axon-level theoretical framework, showing that an inward-rectifier potassium ion current is essential for an anode break [35]. Both membrane potential and stimulation duration affect the development of an anode break. When the membrane potential is in a more depolarized position, the potassium ion current decreases, and a current flowing into the axon is generated only at the end of anodal stimulation to form an action potential. It is essential to explore the possibility of BSW with asymmetric cathodal and anodal stimuli, which has not been a focus of study in the research area of selective stimulation.

1.3.3 Conduction block

Animal experiments have demonstrated that non-pharmaceutical nerve conduction block can be achieved in mammals (Figure 1.5) [36]. However, the experiments, which used plier electrodes to stimulate nerves directly by high-frequency high-strength waves, are not suitable for human therapy. Furthermore, a simulation study [37] showed that high-frequency stimulation could gradually open potassium channels of myelinated nerves and increase its threshold, thus temporarily reducing the excitability of the myelinated nerves. This phenomenon can occur even without causing a nerve conduction block [37]. Based on this observation, a new scheme for improving C-selectivity called inhibit-Aδ (i-Aδ) was proposed and compared with the other potential schemes.

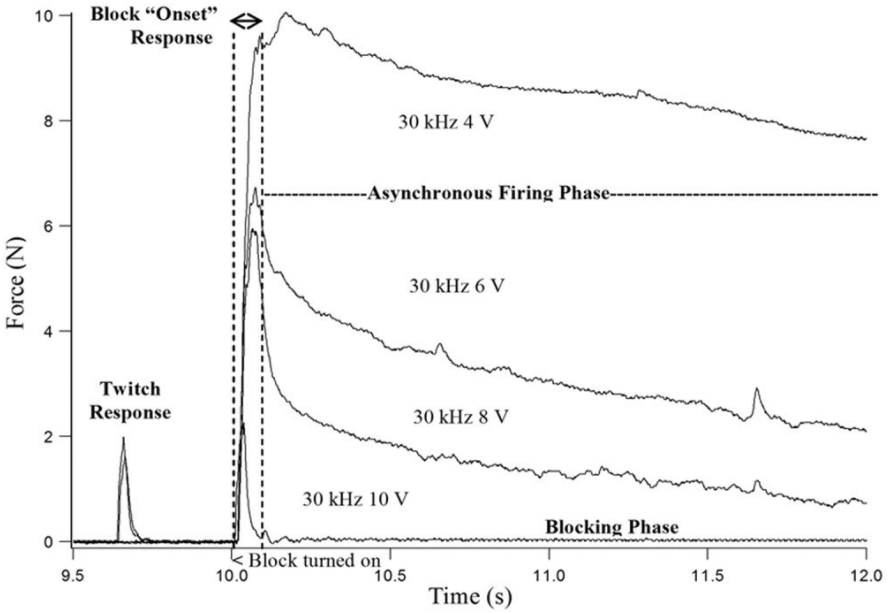

Figure 1.5 conduction block by using high-frequency alternating currents at 30 kHZ and four amplitudes from [36].

1.4 Objectives

In order to meet the needs of analgesia treatment in a family environment, I aim to realize endogenous opioid based effective chronic pain relief through surface stimulations. This requires stimulation schemes with the following features: 1) high C-selectivity over Aδ (C-selectivity), considering multiple adversarial factors in future implementations of surface stimulations, the C-selectivity needs to be as high as possible; and 2) conduction of the stimuli from the skin surface to the vicinity of nociceptive fibers.

In this study, I focused on the first issue to explore the possibility of selective stimulation of C. Moreover, the findings that are useful for the second requirement will also be addressed. Figure 1.6 shows the overall figure of this research.

In the previous section, I summarized the existing selectivity stimulation methods and the possibilities or problems in C-selectivity. To solve these problems and increase C-selectivity, 3 tasks were formulated for selectivity stimulating C fibers in deep tissues:

1) to make clear the mechanism of Anodal-first waveforms for improving selectivity of C fibers.
2) to propose high frequency sine wave pre-pulse for reducing the excitability of Aδ fibers, and make clear its mechanism
3) to confirm how high frequency carrier wave affects the stimulation for high C-selectivity.

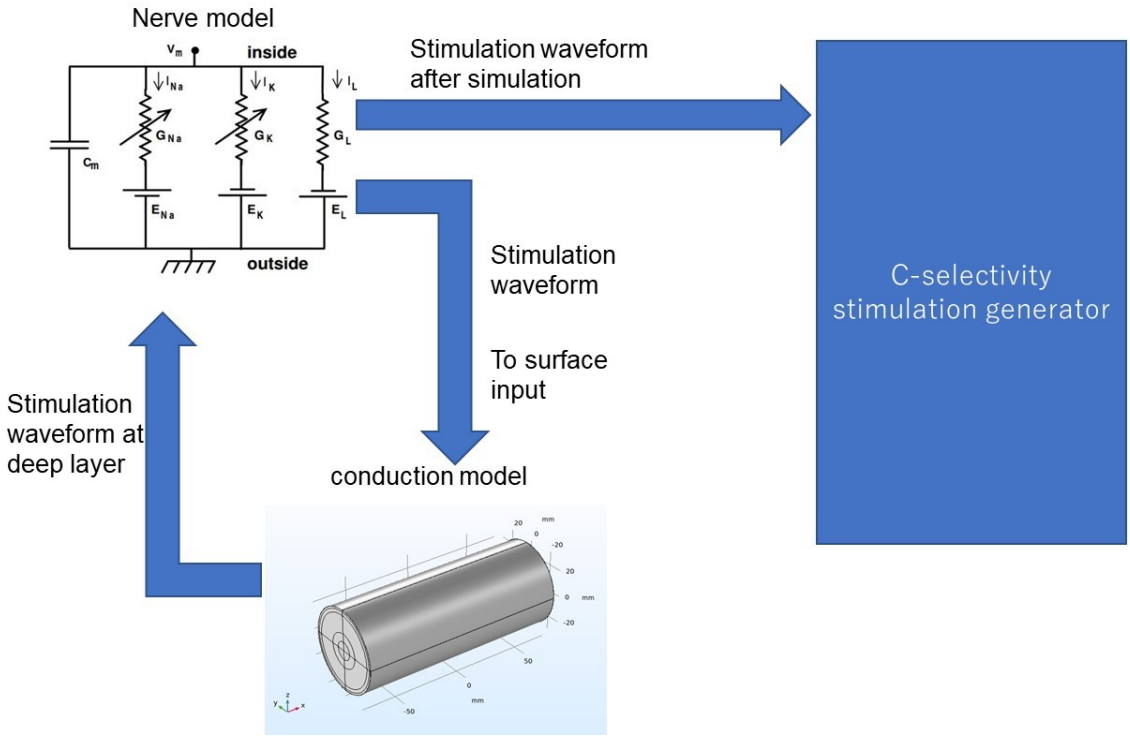

Figure 1.6 Overview of the system combine with nerve model and conduction model.

1.5 Structure of the thesis

This thesis contains six chapters, as summarized as follows.

1) In Chapter 2, I introduced two models, HH model and MRG model, that simulate C and Aδ afferent fibers. Also, I described the evaluation criterion, constraints of simulation.
2) In Chapter 3, I introduced the anodal-first stimulation for reducing the threshold of C and described the details of the stimulation wave used in experiments. The mechanism and nerve dynamic changes were studied by using phase portrait analysis when applying an anodal-first stimulation on C and Aδ fibers. The waveform parameters included frequency, duration, ISI, and polarity asymmetry ratio (PAR) were analyzed to improve the C-selectivity.
3) In Chapter 4, I introduced the high frequency pre-pulse stimulation for increasing the threshold of Aδ and described the details of the stimulation wave used in experiments. The results of current changes in ion channels were analyzed when applying a high-frequency stimulation on C and Aδ fibers. The parameters of each ion channels such as slow potassium ion channels opening variable *s* were discussed and their influence on C and Aδ fibers were compared.

4) In Chapter 5, I introduced the high frequency carrier wave for stimulating fibers in the deep layer, and it effect on C-selectivity. In order to optimize the parameters of C-selectivity, I combined the anodal-first stimulation (BSW), stimulation with high frequency carrier wave (BMAC) and high frequency sine pre-pulse (i-Aδ), and analyzed their effects on nerve activation.
5) In Chapter 6, I discussed the results of each chapter, and summarized the contributions and limitations of this research and future research directions.

Chapter 2
Research Methodology

2.1 Overview

This chapter aims to show what mathematic model used in this study and validate the two models for simulating C and Aδ fibers. Also, show the analysis method, experimental setup, and evaluation method.

2.2 Nerve model

2.2.1 HH model for C fiber

The Hodgkin-Huxley (HH) model can be used to describe the behaviors of sodium and potassium currents of the giant squid (Figure 2.1) [38, 39]. This model has been used to model the behaviors of endocrine cells, nerves, and muscles in various organisms ranging from invertebrates to mammals [37, 40, 41]. Researchers have already used the HH model to explain mammalian unmyelinated nerves [42]. A model of C that takes action potential propagation into consideration has been established to reproduce experimental data from patients and animals in earlier experiments [43].

In our study, the basic portion of the model was the same as that reported in [43] and expressed by differential equations (1) to (3). Referring to the experimental results in [44, 45], the equations have been adapted to human C fibers by reducing the resistivity, fiber diameter, etc. Equation (1) shows the change in transmembrane current by external stimulation. Equation (2) presents an expression of the ionic transmembrane current I_{ion}, and equation (3) shows the differential equation of the variables.

$$C_m \frac{dV_m}{dt} + I_{ion} = I_{ext} \tag{1}$$

$$I_{ion} = g_{Na} m^3 h (V_m - E_{Na}) - g_K n^4 (V_m - E_K) - g_l (V_m - E_l) \tag{2}$$

$$\frac{dx}{dt} = \alpha_x (V_m)(1 - x) - \beta_x (V_m) x \tag{3}$$

$$\alpha_m\ \alpha_n\ \beta_h = \frac{A(V_m - B)}{1 - e^{\left[-\frac{V_m - B}{C}\right]}} \qquad \beta_m\ \beta_n\ \alpha_h = Ae^{\left[\frac{-V_m}{C}\right]} \tag{4}$$

In equation (1), C_m is the membrane capacitance, V_m is the intracellular potential, t is time, I_{ion} is the ionic transmembrane current, and I_{ext} is the externally applied stimulation current. In equation (2), m, h, and n define the open status of those ion channel gates as the opening or closing of sodium ion channels and the opening of potassium ion channels, respectively. In addition, g_{Na}, g_K, and g_{Lk} represent the maximal conductance of sodium and potassium ion channels and the current leakage, respectively. E represents the resting potential of each channel. In equation (3), x=:{m, h, n}, , α and β are constants dependent on the transmembrane voltage, describing the transient rates of open and closed channel gates. The values of the parameters for this study are shown in Table 2.1.

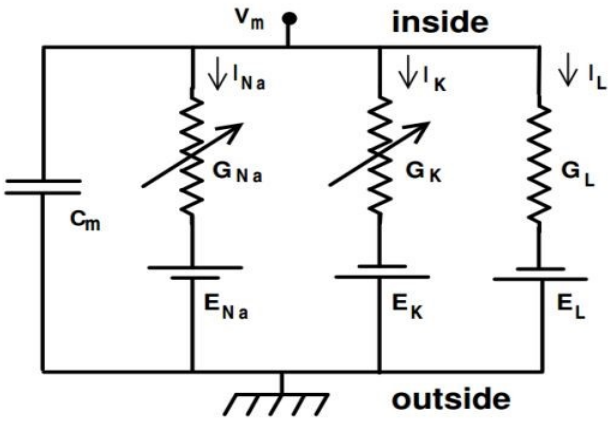

Figure 2.1 The HH double-cable axon model [38]

Table 2.1 C-fiber model parameters

Maximum Na+ channel conductance (g_{Na})	120.0 mS/cm^2
Maximum K+ channel conductance (g_K)	36.0 mS/cm^2
Leak channel conductance (g_{Lk})	0.3 mS/cm^2
Membrane capacitance (C_m)	1.0 μF/cm^2
Na+ reversal potentials (E_{Na})	50.0 mV
K+ reversal potentials (E_K)	-77.0 mV
Leak reversal potentials (E_{Lk})	-54.4 mV
Rest potentials	-65.0 mV
Fiber diameter	1 μm

Voltage and time-dependent parameters (Equation 4)	A(m/s)	B(mV)	C(mV)
α_m	0.10	25.00	10.00
β_m	4.00	0.00	18.00
α_h	0.07	0.00	20.00
β_h	1.00	30.00	10.00
α_n	0.01	10.00	10.00
β_n	0.125	0.00	80.00

2.2.2 MRG model for Aδ fiber

The models of myelinated nerve fibers have been developed by some research efforts [46, 47]. Among them, the MRG (McIntyre, Richardson, and Grill) model, which was originally a geometrically and electrically accurate model of mammalian motor nerve fibers [48], has been used to simulate myelinated afferent nerves [49-51]. The validity of MRG model has been demonstrated by a couple of mammalian motor nerve experiments [52, 53].

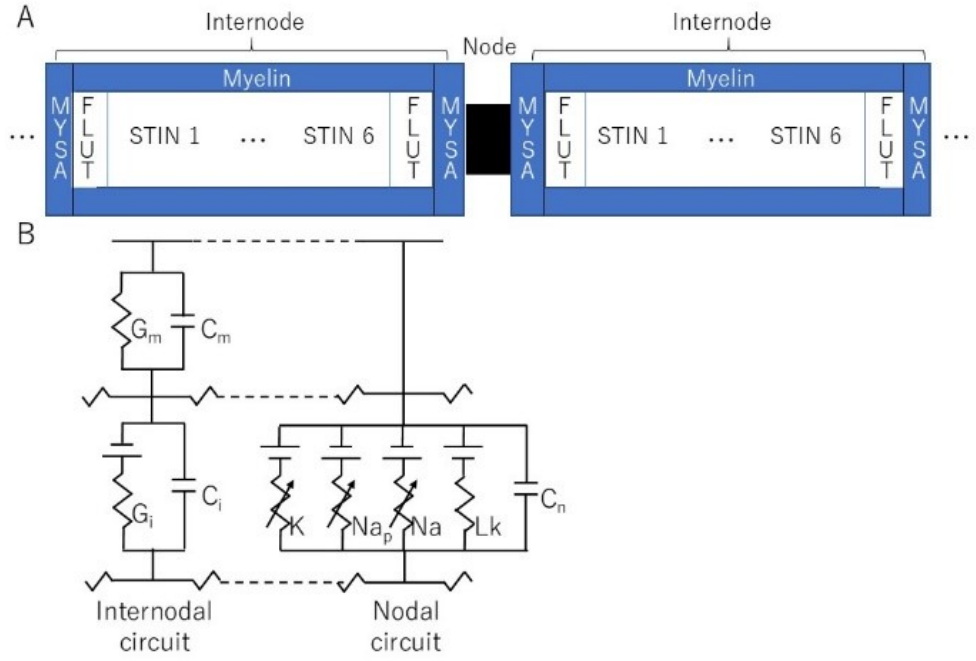

Figure 2.2 The MRG double-cable axon model

A: Two of the 20 internode segments around each Ranvier node. Two myelin sheath attachment segments (MYSA), two fluted region segments (FLUT), and six stereotyped internode segments (STIN) on each side.

B: An equivalent voltage-dependent resistor circuit model of Ion channels at nodal and inter-nodal segments. The nodal segment of the Ranvier segment (i.e., nodal circuit on the right) contains fast sodium (Na), persistent sodium (Nap), and slow potassium (K) channels, and leakage resistance (Lk) with nodal capacitance (Cn). The inter-nodal segment contains resistance and capacitance of the myelin sheath (Gm and Cm) and inter-nodal double-cable structures (Gi and Ci) [48].

The FH (Frankenhaeuser, Huxley) model was first fixed to simulate the behavior of myelinated nerve fibers, and had been demonstrated by the experimental data on the myelinated nerve fibers of frogs [47]. A neural model of mammals has been further developed, since the structure and properties of ion channels at the nodes of Ranvier in mammals are distinctly different from those of amphibians [49]. McIntyre et al developed geometrically and electrically accurate models of mammalian motor nerve fibers, which is called MRG models, to study the biophysical mechanisms of axonal excitability changes and recovery cycle regulation [48]. The MRG model can reproduce the experimental data for the excitation properties of mammalian myelinated nerve fibers.

The MRG model is a double-cable axon model consisting of nodes separated by inter-medullary segments wrapped by myelin (Figure 2.2.B). The internode is divided into ten segments: two node myelin sheath attachment segments (MYSA), two fluted region segments (FLUT), and six stereotyped internode segments (STIN) (Figure 2.2). Mathematically, the MRG model can be expressed as equation (1) based on the study of the classical HH model. However, for the different ion channels, the ionic transmembrane current I_{ion} in equation (1) should be expressed as follows:

$$I_{ion} = g_{Naf} m^3 h (V_m - E_{Na}) - g_{Nap} p^3 (V_m - E_{Na}) - g_{Ks} s (V_m - E_K) - g_l (V_m - E_l) \tag{5}$$

$$\alpha_m\ \alpha_p = \frac{A(V_m+B)}{1-e^{\left[-\frac{V_m+B}{C}\right]}} \qquad \beta_m\ \beta_p\ \alpha_h = \frac{A[-(V_m+B)]}{1-e^{\left[\frac{V_m+B}{C}\right]}}$$

$$\beta_h = \frac{A}{1-e^{\left[-\frac{V_m+B}{C}\right]}} \qquad \alpha_s\ \beta_s = \frac{A}{1+e^{\left[\frac{V_m+B}{C}\right]}} \tag{6}$$

Unlike Equation (2), in Equation (5), *Naf* indicates the nodal membrane fast sodium channel, *Nap* is the persistent sodium channel, *Ks* is the slow potassium channel, and *l* is the linear leakage conductance. Variables *m* and *h* are the same as those of the C-fiber model. Variable *p* defines the opening of persistent sodium ion channels, and *s* defines

the opening of slow potassium ion channels. The values of the parameters are shown in Table 2.2. The equivalent circuit of the MRG model is shown in Figure 2.2.B. The C-fiber and Aδ-fiber models were first validated with the existing experimental data about strength-duration (S-D) curves and conduction velocity in next section.

Table 2.2 Aδ-fiber model parameters

Maximum Na+ channel conductance (g_{Naf})		3000 mS/cm^2	
Maximum persistent Na+ channel conductance (g_{Nap})		10 mS/cm^2	
Maximum K+ channel conductance (g_K)		80 mS/cm^2	
Leak channel conductance (g_{Lk})		7 mS/cm^2	
Nodal membrane capacitance (C_m)		2 μF/cm^2	
Na+ reversal potentials (E_{Na})		50 mV	
K+ reversal potentials (E_K)		-90 mV	
Leak reversal potentials (E_{Lk})		-90 mV	
Rest potentials		-80 mV	
Fiber diameter at node of Ranvier		3.3 μm	
Voltage and time-dependent parameters (Equation 6)	A(m/s)	B(mV)	C(mV)
α_m	6.57	20.40	10.30
β_m	0.304	25.70	9.16
α_p	0.0353	27.00	10.20
β_p	0.000883	34.00	10.00
α_h	0.34	114.00	11.00
β_h	12.60	31.80	13.40
α_s	0.30	53.00	-5.00
β_s	0.03	90.00	-1.00

2.2.3 Model validation

The behavior of unmyelinated and myelinated sensory nerves has been studied by using neural models [38, 48]. The strength and duration results of the HH model for unmyelinated C fibers and the MRG model for myelinated Aδ fibers were compared with data recorded in human and animal measurement experiments. As shown in Figure 2.3, these experiments were well matched, verifying the validity of HH and MRG as models of the two sensory nerve fibers.

The implemented HH and MRG models were first validated from two different aspects: strength-duration (S-D) curves and conduction velocity. Figure 2.3.A shows the S-D curve

of the Aδ-fiber model (red dotted line) and the range of sensory axons (gray zone) measured from the human median and ulnar nerves [54]. Figure 2.3.B shows the S-D curve of the C-fiber model (red dotted line) and the range of cat nerves (gray zone) [55]. Both models matched experimental results in the literature.

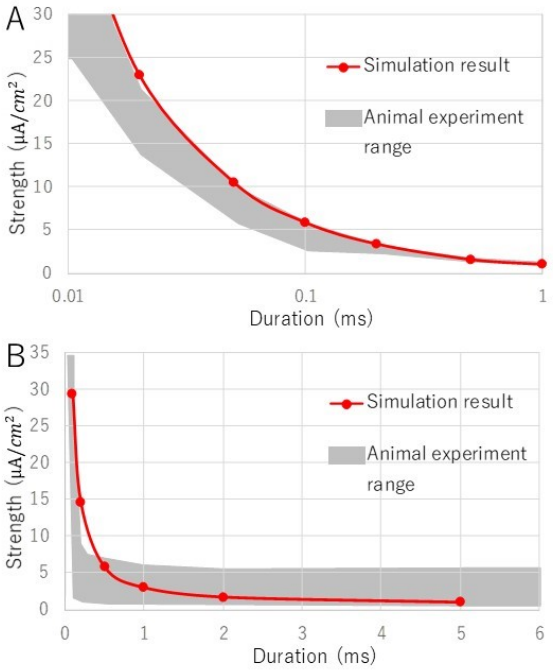

Figure 2.3 Normalized strength-duration curves from A: Aδ fibers and B: C fibers. The gray area indicates the range of animal experimental data from [51], and the red line represents the simulation result with our method.

The conduction velocity of the C-fiber model (diameter: 1 μm) and Aδ-fiber model (diameter: 3.3 μm) were 0.98 m/s and 27.5 m/s, respectively, which is consistent with measurement experimental results of 0.5-2 m/s and 5-40 m/s for C and Aδ, respectively, using the same diameters as simulation settings as reported in [56, 57].

2.3 Experimental setup and analysis

2.3.1 Experimental setup

For both nerve fibers, only a single fiber case was considered, and each fiber consisted of 40 nodes. The distance between each pair of nodes is 10 μm and 220 μm for the C-fiber and Aδ-fiber models, respectively. The cathode electrode was set at the 21th node along the radial direction, and the anode electrode was set far enough away from the object fiber along the radial direction. Stimuli with a specific current density (i.e.,

thresholds of each model) were applied to each nerve fiber model through the cathode electrode. The neural behaviors of each modeled nerve fiber were recorded and analyzed.

For the analysis, the unmyelinated and myelinated nerve models were first confirmed using past animal experimental data and then used to evaluate and compare three different stimulation schemes targeting high C-selectivity, which were evaluated using the C-selectivity index R_{th}.

Both models were implemented on MATLAB 2013a (The MathWorks, Inc., Natick, Massachusetts, USA). The 4th-order Runge–Kutta method was employed to solve differential equations of the HH and MRG models numerically. A time step of 0.1 μs was used in the numerical computation. All the computer simulations were run on a desktop computer with a quad-core, 3.4 GHz processor. It takes 240 s for the Matlab code to compute one axon.

2.3.2 Phase portrait analysis

To understand and interpret the mechanism behind high C-selectivity, phase portrait analysis of membrane potential and other important ion channel variables was employed. Phase portrait analysis has been used to analyze the behavior of the nonlinear equations of the HH model [58]. Fig.2.4 shows the change of the time constant of each variable as the membrane potential V_m increases in the HH and MRG models. It is clear that the time constant of variable m is considerably reduced compared with h and n, which means the m exerts the greatest effect on system behavior. Based on this observation, it is reasonable to set h and n constant at their resting value for the next step in phase portrait analysis. Three singular points are present in the phase portrait of (V_m, m): a stable resting point, a threshold saddle point, and an exciting stable point. In general, the closer the threshold saddle point to the stable resting point, the more susceptible the nerve is to excitation. The change in threshold saddle point also indicates changes in model excitability.

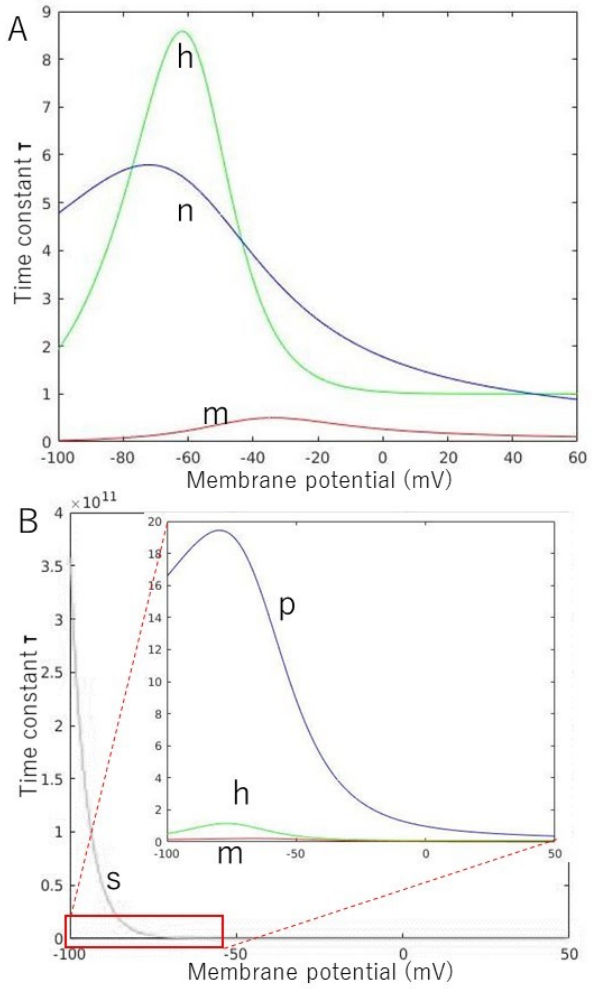

Figure 2.4 The time constants of membrane ion channel variables

A: Time constants of the HH model. Variables *m*, *h*, and *n* define the open status of those ion channel gates during the opening and closing of sodium ion channels as well as the opening of potassium ion channels, respectively.

B: The time constant of the MRG model. The variables *m* and *h* represent the opening and closing of fast sodium ion channels, respectively. In addition, *p* defines the opening of sodium persistent ion channels, and *s* defines the opening of slow potassium ion channels.

Although *h* and *n* were assumed to be constants, they are also variables, and changes in *h* and *n* cause changes in membrane potential as well as the threshold of the saddle point and exciting stable point in the phase portrait. For the convenience of discussion and given their relatively small effect on membrane potential, only constant *h* and *n* cases were analyzed and discussed.

The phase portrait analysis has been applied to myelinated nerve models, such as the

Frankenhaeuser-Huxley (FH) model [54]. However, few studies have assessed the dynamics of the MRG model in the phase portrait, which may lead to stimulation schemes favoring C-selectivity over Aδ if compared with the dynamic behavior of C. Therefore, in this study, phase portrait analysis of the HH and the MRG model responding to stimuli of different stimulation schemes with different parameters was performed to clearly define the mechanism underlying high C-selectivity.

2.4 Evaluation

To assess selective stimulation of C, the excitation threshold of C (Th_C), that of Aδ fiber nerves ($Th_{A\delta}$), and their ratio, R_{th} (Equation (7)), were used.

$$R_{\mathrm{th}} = Th_{\mathrm{C}}/Th_{\mathrm{A}\delta} \tag{7}$$

R_{th} was used to analyze which nerve fiber model was more likely to be excited by a particular stimulation waveform. $R_{th} < 1$ and $R_{th} > 1$ imply that C is more favored than Aδ and that Aδ is more favored than C, respectively.

Chapter 3

Analysis of anodal-first waveform

3.1 Overview

This chapter was written based on the publication “Gate mechanism and parameter analysis of anodal-first waveforms for improving selectivity of C-fiber nerves” [59], in which, the mechanism of an anodal-first stimulation for reducing the threshold of C was made clear. Some results from the publication paper “A simulation study on selective stimulation of C-fiber nerves for chronic pain relief” [60].

3.2 Stimulation schemes

Figure 3.1 shows a waveform example of this study. The amplitudes of the anodal and cathodal stimuli are V_a and V_c, respectively, and the durations of the anodal and cathodal stimuli are denoted using t_a and t_c, respectively. In each period, there is an interstimulus interval (ISI) between an anodal stimulus and a cathodal stimulus. In this chapter, the stimulation waveforms on C-selectivity were explored with the following effects: 1) the effect of polar precedence (ie, anodal-first or cathodal-first) of the waveform and the waveform total duration; 2) the influence of the interstimulus interval (ISI) between an anodal and a cathodal stimulus; and 3) the effect of the polarity asymmetry ratio (PAR, eg, PAR 1:9 means that the cathodal stimulus duration is 9 times larger than that of the anodal stimulus, in the case of anodal-first stimulation). In this study, the waveforms with charge-balanced of anodal stimuli and cathodal stimuli were investigated.

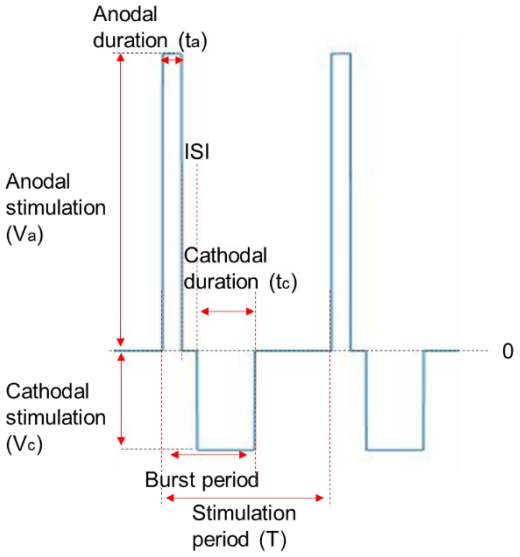

Figure 3.1 An example of the stimulation waveform.

Notes: Each period contains an anodal stimulus and a cathodal stimulus. The PAR is the quotient of the duration of the preceding stimulus and that of the following stimulus. ISI describes the no-stimulus duration between the preceding and following stimuli.

3.3 Experiment results

3.3.1 Changes in activation threshold in phase portrait

Figure 3.2 shows the phase portrait of the C-fiber model for the Na ion channel variable *m* and the membrane potential V_m, (A), in their rest state (*h*: 0.59790, *n*: 0.31708), and (B), (C), and (D), after anodal stimulation with durations of 2 ms, 6 ms and 10 ms, respectively, all at a stimulation strength of 11 μA/cm^2. The phase plane can identify the excitability of nerves. When a saddle point *b* exists, as shown in Figure 3.2.B, a smaller distance between two intersections, Δd_int (a 2-dimensional vector (ΔV_m, Δm) containing a difference in intracellular potential V_m and a difference in gate variable *m*) denotes easier excitation of the nerve. On the other hand, as shown in Figure 3.2.C-D, there is no intersection point of two isocline curves. In this case, the shortest distance between the two separate isocline curves, Δd_sep, might reflect the excitation of the nerve. For the situations shown in Figure 3.2., (A) Δd_int =(2.7, 0.01402), (B) Δd_int =(2.0, 0.00924), (C) Δd_sep =(0.1, 0.00057), and (D) Δd_sep =(0.1, 0.00089).

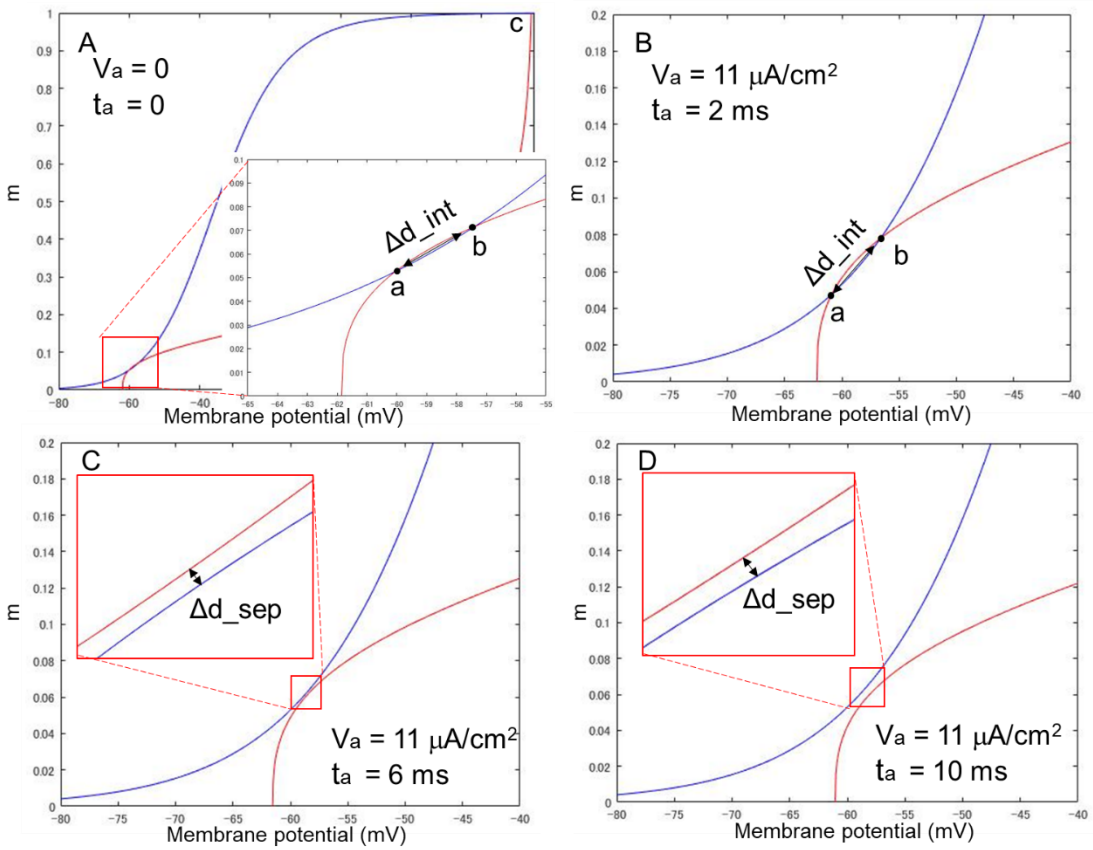

Figure 3.2 Phase portrait of the C-fiber model with anodal stimulations of different durations.

If there is no intersection between two isocline curves, as shown in (C) and (D), the shortest distance between two separate isocline curves, ie, *Δd_sep*, might reflect the excitation of the nerve.

Notes: Strength of anodal stimulations V_a = 11 μA/cm^2. (A) Phase portrait of the resting status, (B) t_a = 2 ms, (C) t_a = 6 ms, and (D) t_a = 10 ms.

3.3.2 The effect of anodal-first anodal stimulation

In order to analyze the internal mechanism of the anodal-first stimulation, two experiments were designed by the phase plane and ion channel currents:

(1) Comparing the effect of anodal-first stimulation on the C-fiber and Aδ-fiber models by the phase portrait

Figure 3.3 shows the phase portrait of the C-fiber and Aδ-fiber models with different stimulation waveforms, which are illustrated by A1-F1: (A1) no stimulus, (B1) a cathodal-only stimulus with duration 10 ms and strength 162 $\mu A/cm^2$, (C1) a stimulus with total duration (duration of anodal and cathodal stimulus) 20 ms, strength of cathodal stimulus 86 $\mu A/cm^2$ and PAR 1:1, (D1) a stimulus with total duration 100 ms, strength of cathodal stimulus 20 $\mu A/cm^2$ and PAR 1:9, (E1) a stimulus with total duration 100 ms, strength of cathodal stimulus 148 $\mu A/cm^2$ and PAR 9:1, and (F1) a pre-pulse stimulus with duration 90 ms and strength 75 $\mu A/cm^2$, and a cathodal stimulus with duration 10 ms and strength 225 $\mu A/cm^2$. Note that, the intensity of the preceding and following cathodal stimulus were set according to the experiment of Bostock in (F1) [34]. For the other waveforms, the intensities were set as their threshold strength of the node. The phase portraits of the C-fiber model with different stimulation waveform are shown in Figure 3.3.A2-F2, and the Aδ-fiber model is shown in Figure 3.3.A3-F3. Similar to Figure 3.2, while rest point *a* and saddle point *b* remain at the intersections of the two isocline curves of the Aδ-fiber model (Figure 3.3.A3-F3), they disappear in the phase portraits of the C-fiber model (Figure 3.3.C2-D2). Following the definition of distance in section 3.3.1, *Δd_int* and *Δd_sep* were used to analyze the responses of the C-fiber and Aδ-fiber models to different stimuli. Stronger anodal strength causes *Δd_sep* and its gradual increase, meaning that it causes a lower excitation threshold.

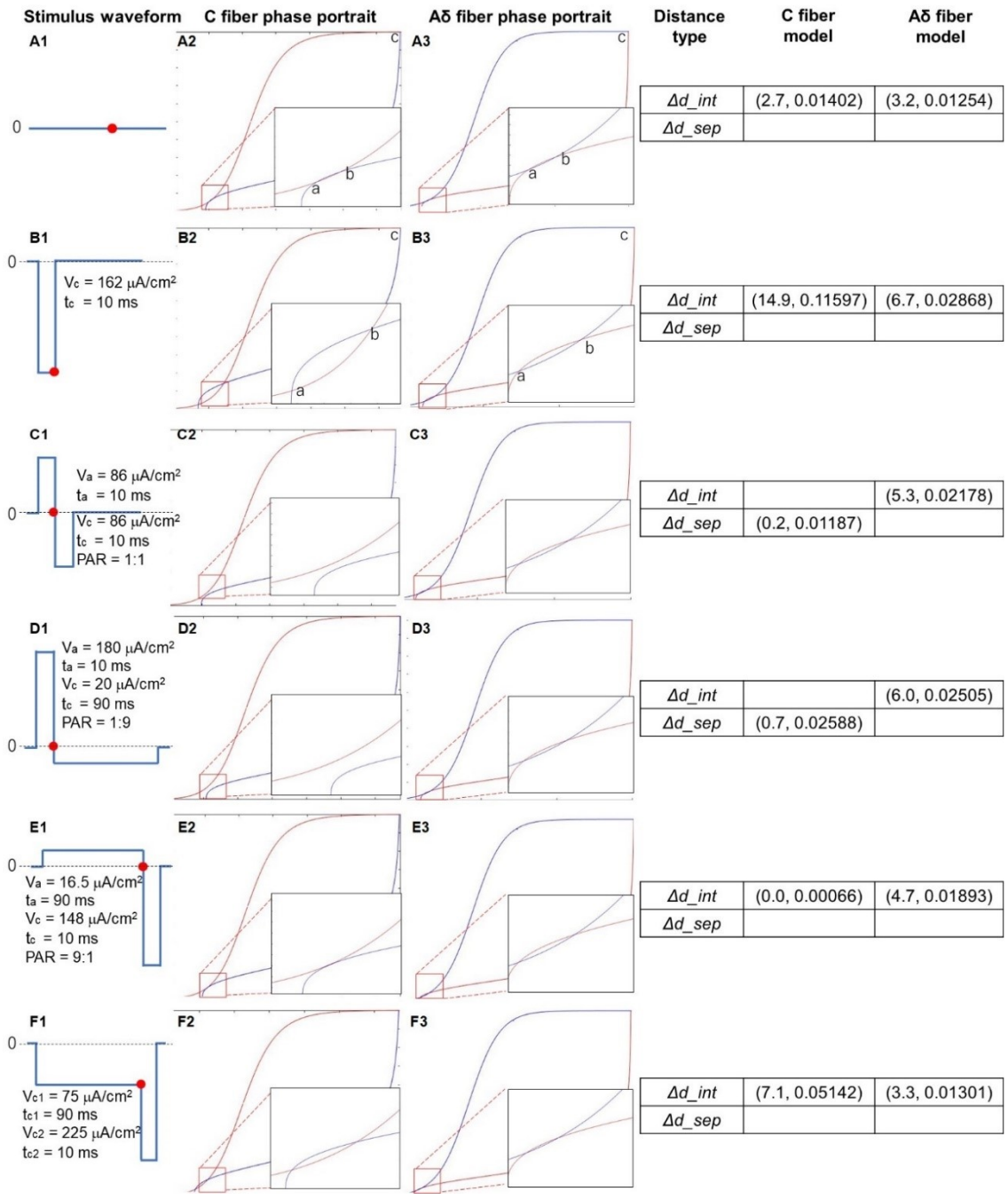

Figure 3.3 Phase portraits of the dynamic behavior of the C-fiber and Aδ-fiber models responding to different stimuli.

Δd_int and *Δd_sep* were used to analyze the responses of the C-fiber and Aδ-fiber models to different stimuli. A stronger anodal strength causes the separation of two isocline curves and increases *Δd_sep*, which indicates a lower excitation threshold. Notes: (A1)—(F1) Illustration of stimulation waves: (A1) no stimulus, (B1) a cathodal-only stimulus with duration 10 ms and strength 162 μA/cm^2, (C1) a

stimulus with total duration 20 ms, strength of cathodal stimulus 86 μA/cm^2 and PAR 1:1, (D1) a stimulus with total duration 100 ms, strength of cathodal stimulus 20 μA/cm^2 and PAR 1:9, (E1) a stimulus with total duration 100 ms, strength of cathodal stimulus 148 μA/cm^2 and PAR 9:1, and (F1) a pre-pulse stimulus with duration 90 ms and strength 75 μA/cm^2, and a cathodal stimulus with duration 10 ms and strength 225 μA/cm^2. (A2)—(F2) the phase portraits of the C-fiber model with different stimulations. (A3)—(F3) the phase portraits of the Aδ-fiber model with different stimulations. The 4th column: *Δd_int* and *Δd_sep* as a result of different stimulations.

(2) Changes in ion channel variables and ion current caused by the anodal-first stimulation

The membrane potential and the current ion channels were further examined to uncover the mechanism of anodal-first biphasic simulation. Figure 3.4 shows the changes in (A) total transmembrane ion current, (B) ion current in Na ion channel, and (C) ion current in K ion channel, about membrane potential, and (D) membrane potential change about stimulus time, responding to the same strength following the cathodal stimulus but different strength preceding anodal stimulations. The preceding anodal stimulation had the following parameters: (1) no stimulus, (2) anodal duration 10 ms, anodal strength 86 μA/cm^2 and PAR 1:1, (3) anodal duration 90 ms, anodal strength 180 μA/cm^2 and PAR 1:9, (4) anodal duration 10 ms, anodal strength 58 μA/cm^2 and PAR 2:1, (5) anodal duration 10 ms, anodal strength 21 μA/cm^2 and PAR 7:1 and (6) anodal duration 10 ms, anodal strength 16 μA/cm^2 and PAR 9:1, while the cathodal stimulus strength is identical to that described in Figure 3.3.B1 (162 μA/cm^2).

The red boxes in Figure 3.4.A-C shows the change in ion current before the threshold (prethreshold phase). The black dots denote the moment when the membrane potential reaches the threshold, *ΔI* shows the difference between the ion current of each polarity asymmetric stimulation waveform and the ion current of no anodal stimulation at its threshold strength. The results of each *ΔI* are 36.94 μA, 24.53 μA, 18.24 μA, 9.35 μA, and 5.18 μA, corresponding to simulation with PAR 1:9, 1:1, 2:1, 7:1, and 9:1, respectively. Because, as shown in Figure 3.4.B, there is no difference in the Na^+ ion currents corresponding to different stimulation waveforms (maximal ΔI_{Na}: 4.50 μA at PAR=1:9, average ΔI_{Na}: 2.58 μA), it is clear that the difference in transmembrane ion current (maximal *ΔI*: 43.98 μA at PAR=1:9, average *ΔI*: 25.24 μA) is mainly due to the change in K^+ ion current (maximal ΔI_K: 48.48 μA at PAR=1:9, average ΔI_K: 27.82 μA), as shown in Figure 3.4.C. With the same strength of cathodal stimulus, a stronger anodal

stimulus caused faster activity potential generation, as shown in Figure 3.4.D.

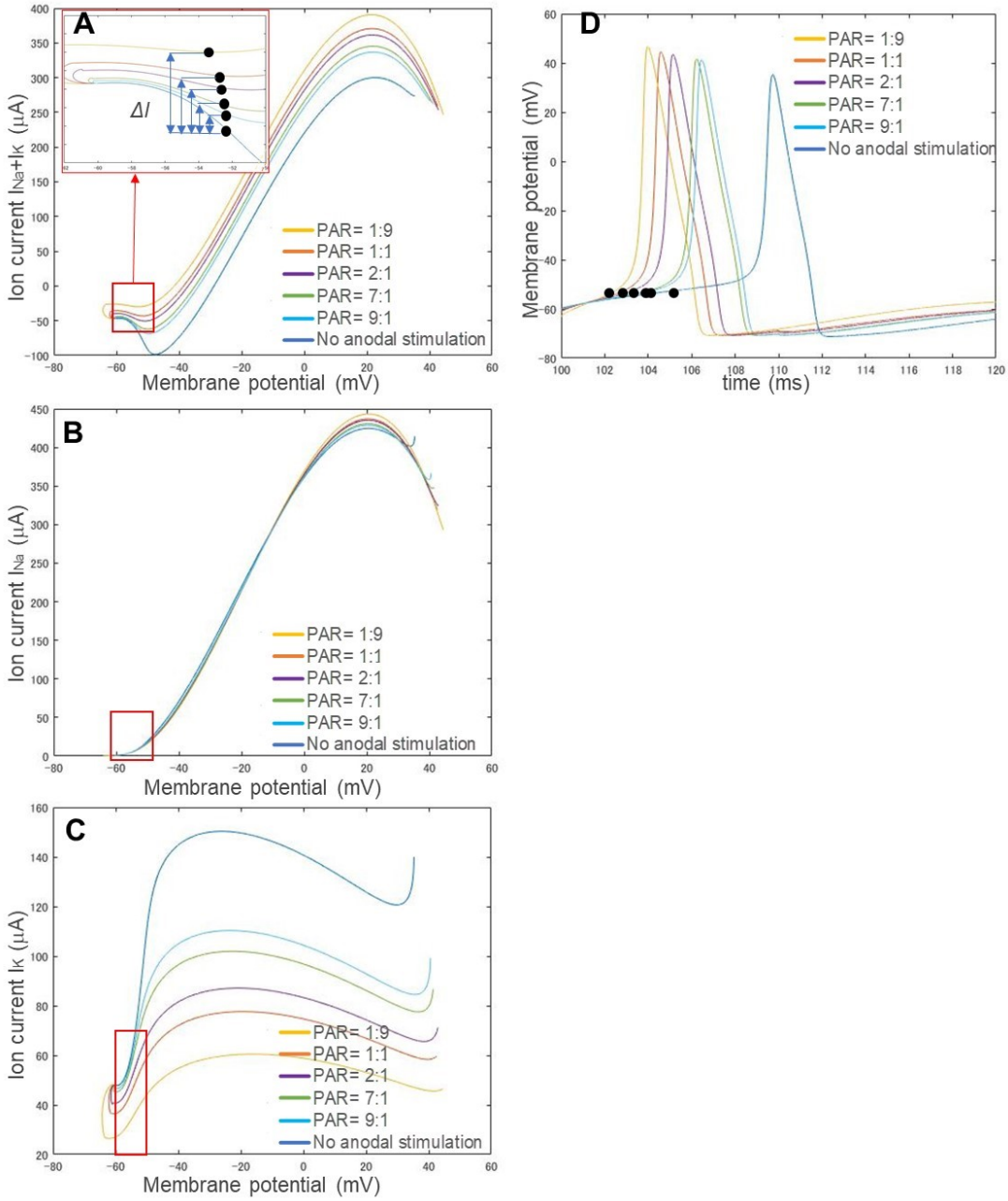

Figure 3.4 Changes in ion channel currents with respect to membrane potential responding to different preceding anodal stimuli and one identical preceding cathodal stimulus.

(A) Transmembrane ion current: I_{Na} + I_K. (B) Current of Na ion channel: I_{Na}. (C) Current of K ion channel: I_K. (D) The change in membrane potential over time. Since there is no difference between the Na^+ ion currents corresponding to different stimulation waveforms, the difference in transmembrane ion current is mainly due

to the change in K^+ ion current. Moreover, a stronger anodal stimulus accelerates the speed of activity potential generation.

Notes: The preceding anodal stimulation had the following parameters: (1) no stimulus, (2) anodal duration 10 ms, anodal strength 86 $\mu A/cm^2$ and PAR 1:1, (3) anodal duration 90 ms, anodal strength 180 $\mu A/cm^2$ and PAR 1:9, (4) anodal duration 10 ms, anodal strength 58 $\mu A/cm^2$ and PAR 2:1, (5) anodal duration 10 ms, anodal strength 21 $\mu A/cm^2$ and PAR 7:1 and (6) anodal duration 10 ms, anodal strength 16 $\mu A/cm^2$ and PAR 9:1. The cathodal stimulus strength was always 162 $\mu A/cm^2$ in all stimulation waveforms. The red box in each graph shows the change in ion current before reaching the membrane potential threshold (prethreshold phase).

The ion channel variables *h* and *n* play an important role in neural dynamics, even though they were not the focus of most simulation studies. Figure 3.5 shows the changes in the ion channel variables (A) *m*, (B) *h* and (C) *n* of the C-fiber model with respect to membrane potential, (D) membrane potential change with regard to stimulus time, responding to different stimulation waveforms: 1) a cathodal-only stimulus with duration 10 ms and strength 162 $\mu A/cm^2$, 2) a stimulus with total duration 20 ms, strength of cathodal stimulus 86 $\mu A/cm^2$ and PAR 1:1, 3) a stimulus with total duration 40 ms, strength of cathodal stimulus 46 $\mu A/cm^2$ and PAR 1:3, 4) a stimulus with total duration 70 ms, strength of cathodal stimulus 27 $\mu A/cm^2$ and PAR 1:6, 5) a stimulus with total duration 100 ms, strength of cathodal stimulus 20 $\mu A/cm^2$ and PAR 1:9, 6) a stimulus with total duration 30 ms, strength of cathodal stimulus 115 $\mu A/cm^2$ and PAR 2:1. 7) a stimulus with total duration 80 ms, strength of cathodal stimulus 145 $\mu A/cm^2$ and PAR 7:1, and 8) a stimulus with total duration 100 ms, strength of cathodal stimulus 148 $\mu A/cm^2$ and PAR 9:1.

Note that, the stimulus intensity was determined at its threshold strength for each waveform. A red dot in each curve shows the beginning of cathodal stimulus, and a black dot denotes when the membrane potential reaches the threshold, namely, the onset of excitement. As PAR decreases, the threshold is reduced. A different preceding anodal stimulation gives its following cathodal stimulus a different initial state (denoted by a red dot). A stronger anodal stimulus (ie, a lower PAR, such as 1:9) causes a larger deviation from its original position (ie, the beginning position of the no anodal stimulus case) in the phase portraits. Different from Figure 3.4.D, the time of activity potential generation was almost the same as that in Figure 3.5.D since the stimulus intensity was determined at threshold strength, in other words, with a smaller cathodal stimulus and

a stronger anodal stimulus (the difference in black dots indicates the difference in membrane potential when starting the cathodal stimulus).

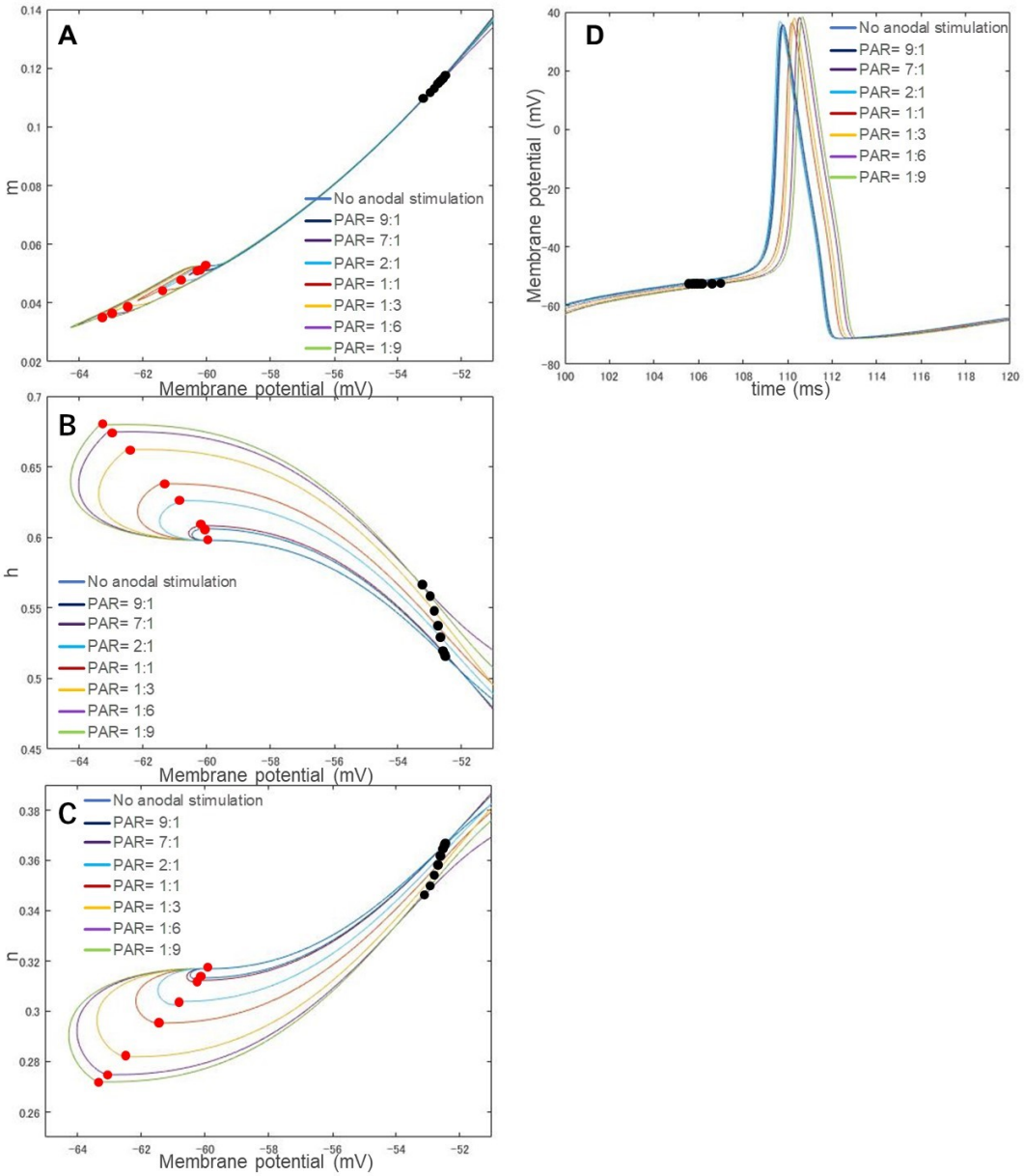

Figure 3.5 The related changes in each ion channel variable and membrane potential.

(A) Opening of Na ion channel: *m*. (B) Closing of Na ion channel: *h*. (C) Opening of K ion channel: *n*. (D) The change in membrane potential over time. A more potent anodal stimulus causes a larger deviation from its original position in the phase portraits. Alternatively, the stimulation waveforms with different PAR values have almost the same speed of action potential generation.

Notes: The stimulation waveforms are: 1) cathodal-only stimulus, duration 10 ms,

strength of cathodal stimulus 162 μA/cm^2, 2) duration 20 ms, strength 86 μA/cm^2, PAR 1:1, 3) duration 40 ms, strength 46 μA/cm^2, PAR 1:3, 4) duration 70 ms, strength 27 μA/cm^2, PAR 1:6, 5) duration 100 ms, strength 20 μA/cm^2, PAR 1:9, 6) duration 30 ms, strength 115 μA/cm^2, PAR 2:1, 7) duration 80 ms, strength 145 μA/cm^2, PAR 7:1, 8) duration 100 ms, strength 148 μA/cm^2, PAR 9:1. A red dot in each curve on each figure's left side means the beginning of cathodal stimulation, and a black dot on the right side denotes where the membrane potential exceeds its threshold.

Figure 3.6 shows the changes in I_{Na} in (A) and I_K in (B) with respect to the membrane potential calculated from the corresponding ion channel variables in Figure 3.5 in the prethreshold phase. The stimulation waveforms are the same as the waveforms in Figure 3.5 at their corresponding threshold strength. This is different from the experiment shown in Figure 3.4, in which the same following cathodal stimulus and different preceding anodal stimuli were used to investigate the effect of preceding anodal stimulation on C-selectivity. Despite the difference in waveforms and threshold strength, there is no significant difference between the I_{Na} (average: 10.22 μA, standard deviation: 1.15 μA), although there is a significant gap in I_K (average: 72.56 μA, standard deviation: 9.25 μA), in which the membrane potential exceeds its threshold. A lower PAR of 1:9 results in a higher I_{Na} or a smaller I_K. After the membrane potential reached the threshold potential, as shown in Figure 3.6.C, the I_K showed a different spatial relationship from those in the prethreshold phase, ie, the PAR (including no anodal stimulation) did not affect the spatial relationship of ion currents in the post-threshold phase.

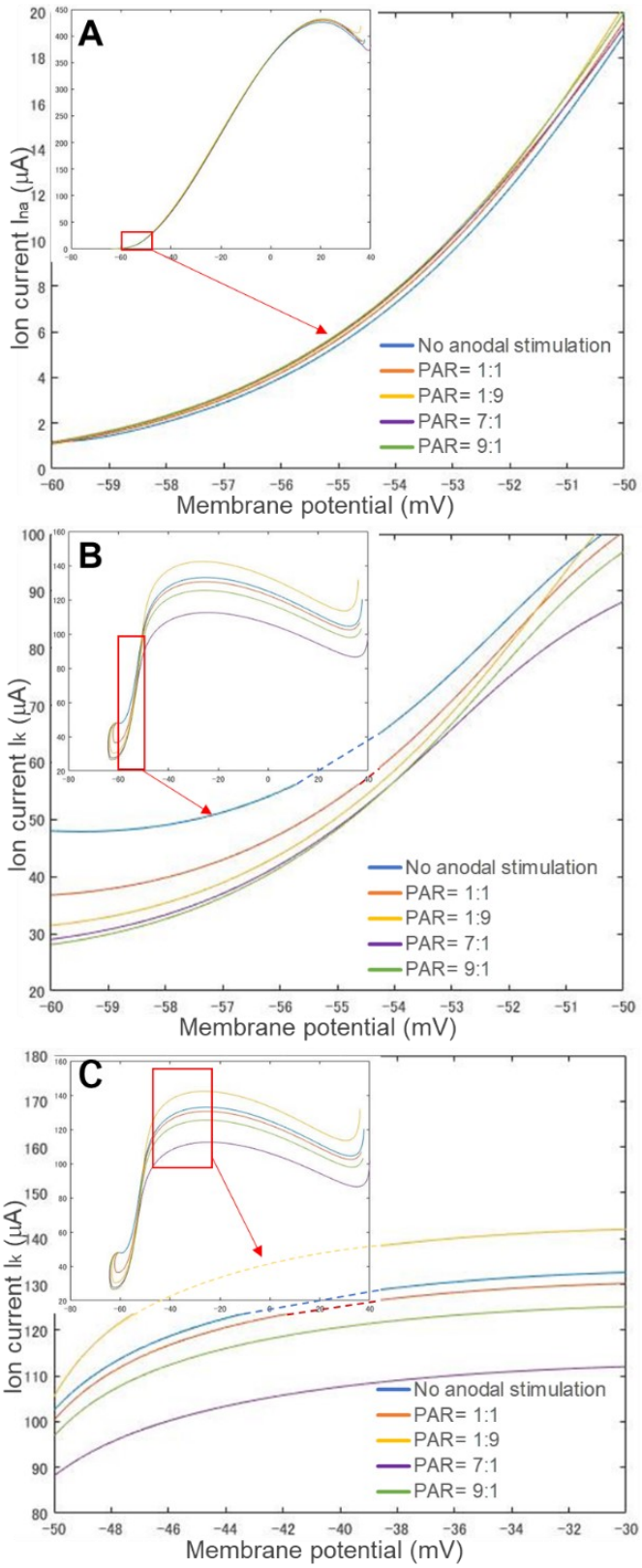

Figure 3.6 Changes in Na (I_{Na}) and K (I_K) ion channel currents and membrane potentials respond to different stimulation waveforms.

(A) Na^+ ion current. (B) K^+ ion current before firing. (C) K ion channel after firing. A lower PAR such as 1:9 results in a smaller I_K. Moreover, there is a significant gap in I_K, but no significant difference in I_{Na}.
Abbreviations: PAR, polarity asymmetry ratio.

3.3.3 The influence of waveform parameters on C-selectivity

The parameter setups are shown in Table 3.1 to explore optimal stimulation parameters.

Table 3.3.1 Parameter setups for C selective stimulation

Experiment (subsection no.)	Duration	PAR	ISI	Period/ Frequency
Duration effect (3.3.3.(1))	(Variable) Anodal: 1 – 10 ms	1:1 A.F&C.F	0 ms	One period
ISI effect (3.3.3.(2))	Anodal: 10 ms	1:1 A.F&C.F	(Variable) 0 – 10 ms	One period
PAR effect (3.3.3.(3))	Anodal: 10 ms	(Variable) 1:1 – 1:9 A.F	0 ms	One period
	Cathodal: 10 ms	(Variable) 1:1 – 9:1 A.F	0 ms	One period
Different duration with same PAR (3.3.3.(4))	(Variable) Anodal: 1 – 10 ms	1:9 A.F	0 ms	One period
Different pulse frequency with different PAR (3.3.3.(5))	Total: $\leq$ 50 ms	1:1; 1:3; 1:6 A.F	0 ms	(Variable) 1 – 50 Hz

Notes: Variables represents the parameters that are verified in every experiment, while other parameters remain constant.

(1) The effect of duration

Figure 3.7 shows the changes in the threshold strength of the C-fiber and Aδ-fiber models as the duration of anodal stimulus changes from 1 ms to 10 ms. Biphasic symmetrical square waves were used for stimulation. Polar precedence was investigated by comparing the cathodal-first (C.F) and anodal-first (A.F). The curve of duration-threshold strength of the C-fiber model and the Aδ-fiber model had an intersection at an approximately 4 ms duration, as shown in Figure 3.7.A (for the A.F case), ie, the threshold strength of the two models is reversed after 4 ms. However, there is no intersection in Figure 3.7.B (for the C.F case), ie, the threshold of the two models remains constant with a long duration. In Figure 3.7.C, the R_{th} decreases as duration increases. The R_{th} could be smaller than 1.0 only in the A.F stimulation case.

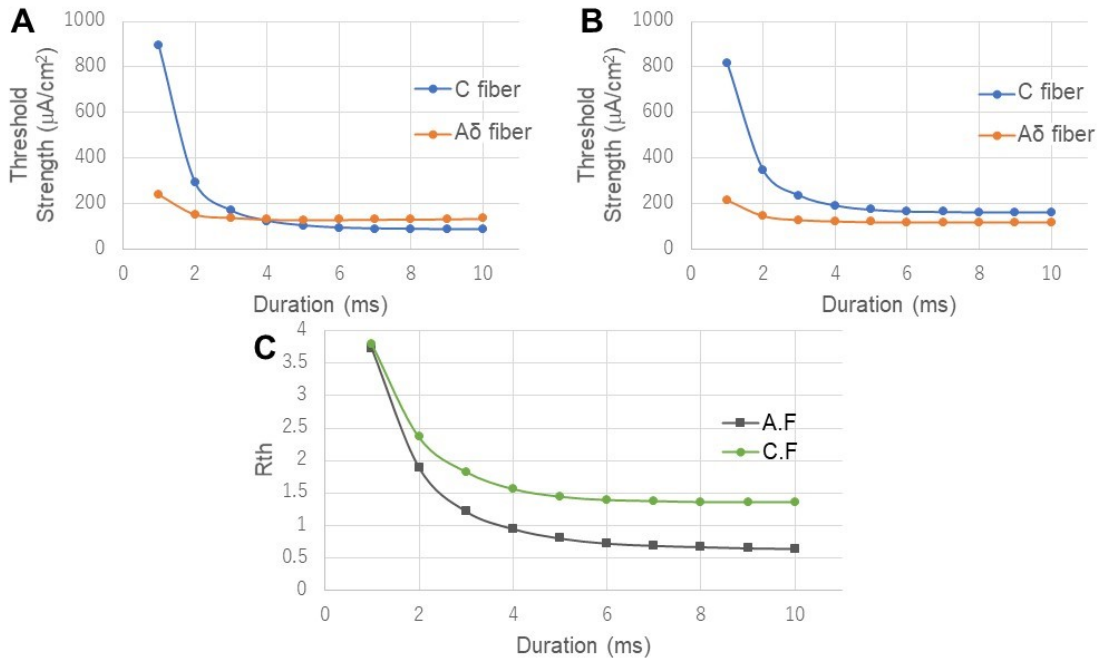

Figure 3.7 Stimulation with biphasic symmetrical waveforms with different durations.

(A) Anodal-first (Anodal stimulus before cathodal stimulus, A.F). (B) Cathodal-first (Cathodal stimulus before anodal stimulus, C.F). (C) R_{th} with different duration values. In A.F stimulation case, the threshold strength of the C-fiber model turns lower than the Aδ-fiber model after the duration is longer than 4 ms, but this does not occur in C.F stimulation case. That is, the A.F stimulation gives positive feedback on C-selectivity.

Notes: The horizontal axis shows anodal stimulus duration. The vertical axis represents the threshold strength. Fibers were stimulated with biphasic symmetrical square waves with no ISI.

(2) The effect of ISI

Figure 3.8.A and B shows the effect of the duration of ISI between an anodal stimulus and a following cathodal stimulus on the threshold changes in the C-fiber and Aδ-fiber models. When in the A.F stimulation, the threshold of the C-fiber model changed significantly with ISI changed. The threshold value starts to rise when the ISI is greater than 2 ms, and over 5 ms, it becomes larger than the threshold value of the Aδ-fiber model. In addition, with the C.F stimulation, the thresholds of the C-fiber model and the Aδ-fiber model did not change significantly. Figure 3.8.C shows the change in R_{th} with ISI. Note that, the C-fiber model threshold of the A.F stimulation is eventually even higher

than the threshold of C.F stimulation. Figure 3.8.D shows the phase portrait when the ISI is 4 ms A.F. The distance between two different curves *ΔdC_sep* is (0.1, 0.00154).

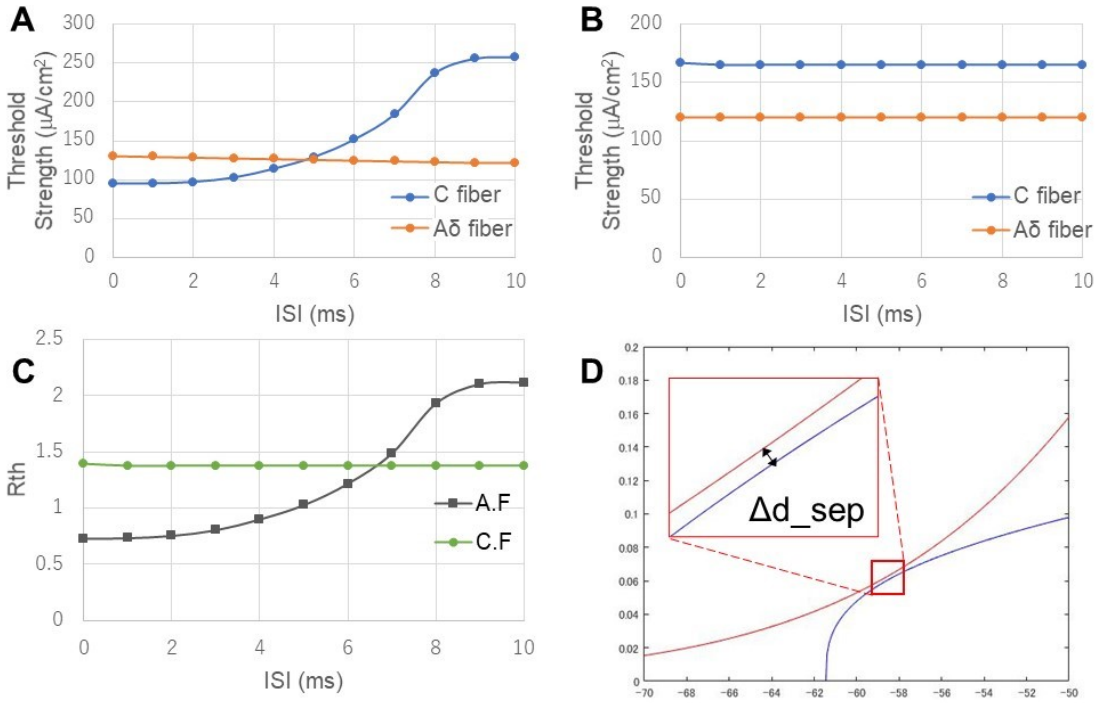

Figure 3.8 Relationship between ISI and threshold strength.

(A) the relationship of ISI-threshold strength in A.F. stimulation case. (B) the relationship of ISI-threshold strength in C.F stimulation case. (C) the relationship of ISI-threshold ratio R_{th} of both A.F, and C.F stimulation cases. (D) The phase portrait in A.F stimulation when the ISI is 4 ms. The threshold of the C-fiber model changed significantly with ISI in A.F stimulation. When using the A.F stimulation, a smaller ISI is more beneficial to C-selectivity.

Notes: Fibers were stimulated with biphasic symmetrical square pulses with a 10 ms anodal duration.

(3) The effect of PAR

The threshold ratio R_{th} changes significantly with the anodal and cathodal stimulus duration ratio when maintaining the charge balance of anodal and cathodal stimuli. For example, if the duration of anodal stimulation is 10 ms and the duration of cathodal is 90 ms, then to maintain charge balance, the strength of anodal needs to be 9 times larger than the strength of cathodal. Figure 3.9 shows the changes in threshold strength in (A) and (B), ratio R_{th} in (C), and required charge in (D) with different PAR values. Figure 3.9.A and B shows that the Aδ simulated by the Aδ-fiber model changed less than the C

simulated by the C-fiber model. In contrast, the threshold strength of C changes significantly. The anodal stimulation has higher strength than the cathodal stimulus, and the stimulation threshold of the C gradually decreases when the duration of the cathodal stimulus increases, which suggests the potential of polarity asymmetric stimulation for C-selectivity.

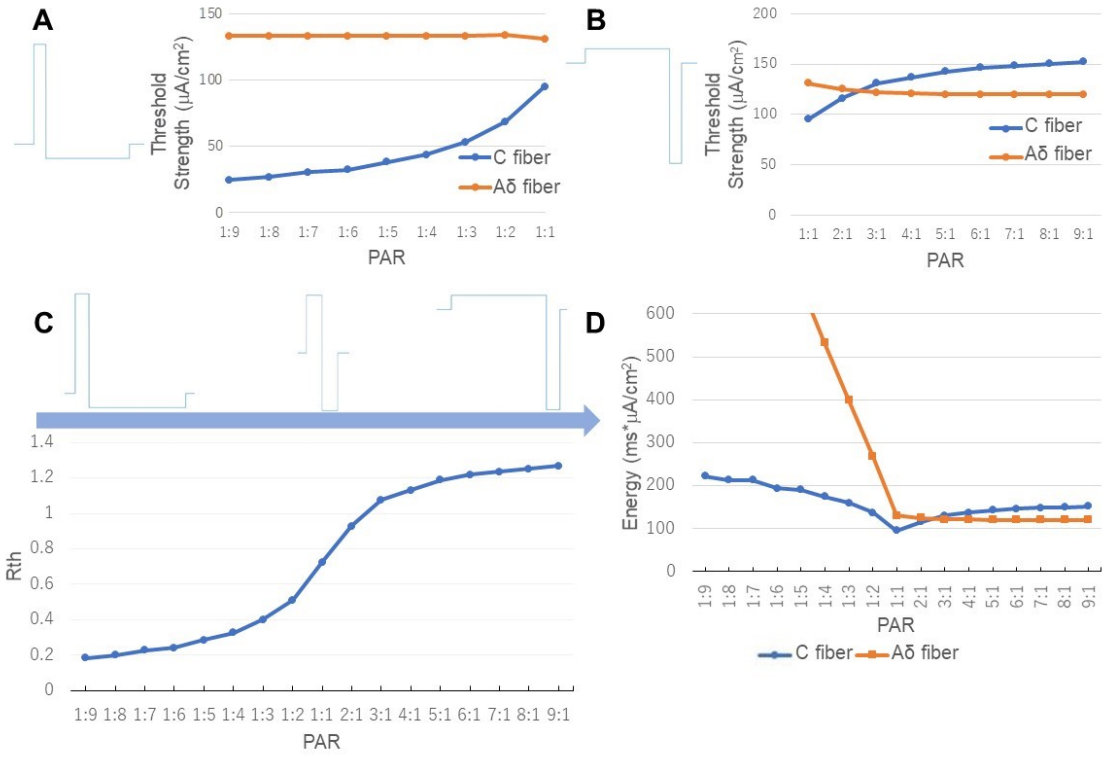

Figure 3.9 Relationship between PAR and threshold strength.

(A) Different duration of cathodal stimuli with the same duration of anodal stimulus. (B) Different duration of anodal stimuli with the same duration of cathodal stimulus. (C) the change of R_{th} over different PAR. (D) the changes in different PAR. According to the results, the threshold strength of C changes significantly. As the cathodal duration increases, the stimulation threshold of C gradually decreases, which suggests the potential of polarity asymmetric stimulation for improving C-selectivity. Notes: (A) The strength of the simulated activation threshold of C and Aδ stimulated by the waveform in which the anodal stimulus is higher than the cathodal stimulus. (B) The strength of the simulated activation threshold of C and Aδ stimulated by the waveform in which the anodal stimulus is lower than the cathodal stimulus. (C) shows the R_{th} with different PAR in (A) and (B). (D) In this experiment, the ISI between anodal and cathodal stimuli is zero.

(4) Different duration with same PAR

Figure 3.10 shows the threshold strength and R_{th} of the C-fiber and Aδ-fiber models when stimulated with an anodal stimulus with different duration values at a PAR of 1:9. Note that the horizontal axis represents the duration of anodal stimulus, which means that the total duration of the stimulus was 10 times that of the anodal stimulus. Since C.F waveforms unable to excite C before Aδ, as shown in Figure 3.7, only A.F waveforms were tested in this section. The threshold strength of the Aδ-fiber model does not change significantly as the duration increases, as shown in Figure 3.10.A. In addition, the threshold strength of the C-fiber model decreases rapidly when the duration is smaller than 4 ms, then slowly decreases from 5 ms, and becomes constant from 8 ms. As shown in Figure 3.10.B, the R_{th} changes from 0.62320 to 0.15833, favoring more C-selectivity, as the anodal duration increases from 1 ms to 10 ms.

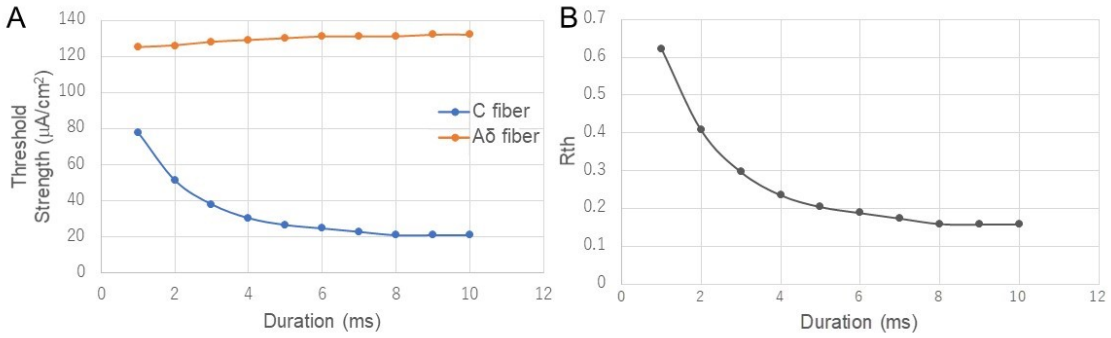

Figure 3.10 Relationship between threshold strength and anodal duration at the same PAR 1:9.

(A) The threshold strength of the C-fiber and Aδ-fiber models. (B) the change of R_{th}. The threshold strength of the C-fiber model decreases when the duration is smaller than 8 ms. Anodal stimulation favors more C-selectivity as the duration increases from 1 ms to 10 ms.

Notes: The horizontal axis shows anodal stimulus duration. Note that the total duration of the stimulus is 10 times the anodal stimulus duration. In this experiment, the ISI between anodal and cathodal stimuli was zero.

(5) Different pulse frequency with different PAR

In addition to duration, we consider that frequency is also a possible factor affecting C-selectivity. Two cases are shown in Figure 3.11. Figure 3.11.A1-C1 shows the changes in threshold strength and R_{th} as frequency increases from 1 Hz to 50 Hz, with no limitation to the total duration of stimulation, at PAR 1:6 1:3 and 1:1, respectively. Figure 3.11.A2-

C2 shows the changes in the same indexes, but with a limitation of 50 ms to the maximum total duration of each period (ie, when the frequency was less than 20 Hz, an ISI was inserted between each two stimuli periods). The stimulation duration was determined using the results shown in section 3.3.3.D, which indicated that the threshold strength of the C-fiber model became constant when the duration of anodal stimulation was longer than 8 ms. As shown in Figure 4.11.A1-C1, the threshold strength of the C-fiber model and the Aδ-fiber model did not change before reaching 20 Hz in all the PAR values, while the threshold strength of the Aδ-fiber model decreased and the C-fiber model increased after reaching 20 Hz. As shown in Figure 3.11.A2-C2, after 20Hz, the C-fiber model showed similar changes with those in Figure 3.11.A1-C1 even with the limitation to maximal duration of each period, except that the threshold strength of the Aδ-fiber model rose above 15 Hz and decreased again above 20 Hz. According to the change in R_{th} over frequency, a lower frequency amplifies PAR's effects.

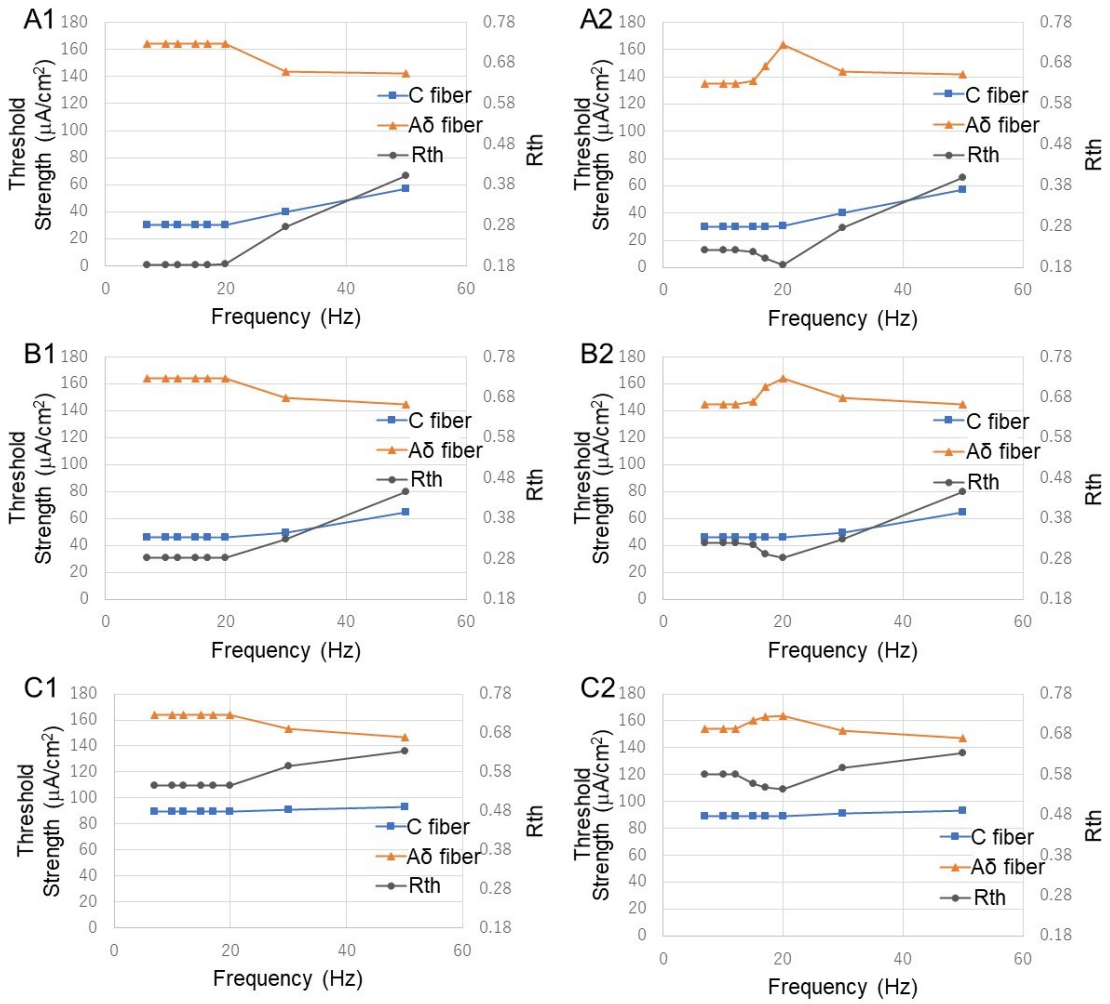

Figure 3.11 Relationship between pulse frequency, threshold strength, and R_{th}

over PAR.

(A1)&(A2) PAR with 1:6, (B1)&(B2) PAR with 1:3, (C1)&(C2) PAR with 1:1. The threshold strength of the C-fiber model increases, and that of the Aδ-fiber model decreases after 20 Hz. According to the change in R_{th} over frequency, a lower frequency amplifies PAR's effects.

Notes: (A1)-(C1) without any limitation to the duration of each period, (A2)-(C2) with a limitation of 50 ms to the maximum duration of each period.

Abbreviations: PAR, polarity asymmetry ratio; R_{th}, ratio of the excitation threshold of C to that of Aδ.

3.4 Discussion

3.4.1 The changes in the phase plane caused by preceding anodal stimulation

The threshold potential, changes, and relative position concerning the resting point can be visualized clearly in the phase portrait, as illustrated in Figure 3.2. When C is given anodal stimulation, the saddle point *b* of the C-fiber model moves downwards closer to rest point *a* until the two points disappear in the phase portrait of the C-fiber model in Figure 3.2. The threshold of C gradually decreases and eventually goes below the threshold of Aδ during this process. As the duration of anodal stimulation increases, *Δd_int* in Figure 3.2 decreases. When t_a = 6 ms, the intersections disappear; instead, the distance between two isocline curves, ie, *Δd_sep*, starts to increase. The decrease in *Δd_int* or the increase in *Δd_sep* reduces the activation threshold of C, which can be justified by the results of Figure 3.7.A and Figure 3.10.A, showing the relationship between the threshold strength of both nerves and the duration of polarity symmetric and asymmetric stimulation, respectively.

The disappearance of the intersections in phase portraits could be confirmed by comparing waveforms in the preceding anodal stimulation. In all the resultant phase portraits shown in Figure 3.3, the waveforms with anodal stimulation include C1 with PAR 1:1, D1 with PAR 1:9, and E1 with PAR 9:1; however, only C1 (*ΔdC_sep* = (0.2, 0.01187) in Figure 3.3.C2) and D1 (*ΔdC_sep* = (0.7, 0.02588) in Figure 3.3.D2) caused the intersection to disappear, whereas the intersections remained after the beginning of the cathodal stimulus (shows a red dot in figure) in the phase portrait of E1 (*ΔdC_int* = (0.0, 0.00066) in Figure 3.3.E2), as well as in those of the waveforms without anodal stimulus, ie, A1 (*ΔdC_int* = (2.7, 0.01402) in Figure 3.3.A2), B1, F1. In fact, intersections remain until PAR decreases from 9:1 to 7:1.

The *Δd_sep* in Figure 3.2.D (t_a = 10 ms) is larger than that in Figure 3.2.C (t_a = 6 ms), and

intersections occur in Figure 3.2.B (t_a = 2 ms), but its *Δd_int* is smaller than that in Figure 3.3.A (no anodal stimulation case). Referring to the comparison results regarding the duration of preceding anodal stimulation in Figure 3.7, ie, a longer duration causes a lower excitation threshold, it is reasonable to state that the stimulations resulting in the separation of the isocline curves in phase portraits benefit more excitability of C than those causing intersected isocline curves, and a larger *Δd_sep* indicates easier excitation of the nerve.

The importance of phenomenon could be made clear through crosschecking the ion currents shown in Figure 3.4, in which the transmembrane ion current right before the excitation of the nerves corresponding to that in Figure 3.3.E1 is almost the same as that in Figure 3.3.A1. Although very different from those in Figure 3.3.C1-D1, the case in Figure 3.3.E1 has a longer anodal duration than that in Figure 3.3.C1-D1 under the same charge constraint. The stimulation with PAR 7:1, which represents the threshold value for causing the disappearance of intersections, has a comparatively greater difference than that of PAR 9:1 (the difference of ΔI: 5.99 μA, larger than the maximal ΔI_{Na}: 4.49 μA, caused by any other PAR). Thus, it is reasonable to state that the disappearance of intersections *a* and *b* indeed play a role in reducing K^+ ion current, hence reducing the threshold of C.

Moreover, a larger *ΔdC_sep* in D2 (0.7, 0.02588) compared with that in C2 (0.2, 0.01187) is caused by its stronger anodal stimulus in D1 (V_a = 180 μA/cm^2) compared with that in C1 (V_a = 86 μA/cm^2), as the duration of the anodal stimuli of C1 and D1 is the same (t_a = 10 ms). This point was further confirmed by the fact that E1 has a lower intensity than both C1 and D1, thus could not cause the disappearance of intersections in the phase plane. In other words, the distance *ΔdC_sep* between the two isocline curves becomes larger as the intensity of the anodal stimulus increases, indicating a stronger effect on reductions in the activation threshold.

Furthermore, the polarity asymmetric waveforms do not affect the threshold of Aδ as much as that of C, as reflected by the comparison between their behavior in the phase plane shown in Figure 3.3.A3-F3 and Figure 3.3.A2-F2.

3.4.2 Ion channel variable and current analysis

Specifically, the threshold strength is affected by the state of each ion channel before the membrane potential reaches its threshold. Equation (1) in section 2.2.1 shows that a reduction of the external cathodal stimulation intensity means that it requires a higher current from the ion channel to compensate for generating the action potential. Thus, three gate variables of ion channel are the focus of the analysis in Figure 3.5.A, which

shows the phase portrait of membrane potential *v* and Na ion channel gate variable *m*. Whatever the initial value of *m* is at the end of the anodal stimulation, the trajectories from the beginning of the cathodal stimulation (denoted by red dots) to the generation of the action potential (denoted by black dots) are all on almost the same curve for different stimulation waveforms. Thus, anodal stimulation does not fundamentally affect the behavior of the variable m because the short time constant of m of both the C-fiber and Aδ-fiber models leads to their fast-changing Na ion channel, as shown in Figure 2.4. The difference caused by anodal stimulation makes it difficult to affect the increase in m during cathodal stimulation.

Compared with the variable *m*, the changes in the variables *h* and *n* are very significant. In the phase portraits of *V*-*h* and *V*-*n*, different stimulation waveforms (cathodal stimulation only, PAR from 1:1 to 1:9) resulted in clearly different trajectories. Equation (2) in section 2.2.1 shows that a higher *h* increases the current of Na ion channel, and a smaller *n* reduces the current of K ion channel, which increases the Na^+ current flowing from the outside to the inside of the membrane and reduces the K^+ current flowing outward from the membrane, respectively, so that the action potential can be achieved with lower cathodal stimulation.

As the stimulus changes from cathodal stimulation only to biphasic stimulation with PAR from 1:1 to 1:9, the gap between the phase portraits of each pair of neighboring stimulation waveforms gradually decreases, which consent with the decreasing trend in the threshold of the C-fiber model in Figure 3.9.A. Although a smaller PAR results in a larger reduction in the cathodal stimulation threshold, further decreasing the PAR may cause saturation of the improvement in C-selectivity.

Figure 3.6. shows the changes in Na and K ion channel current before the threshold potential. Compared with the significant gap of variable *h* in Figure 3.6.B, the gaps between the Na^+ ion currents at threshold potential corresponding to different stimulation waveforms in Figure 3.6.A are not apparent (10.21573 ± 1.14962 μA). In contrast, the gaps between K^+ ion currents in Figure 3.6.B are very significant (72.56375 ± 9.25445 μA). Equation (2) also shows that the Na^+ ion current is positively correlated with the cubes of *m* and *h*. Moreover, the cube of the variable *m* is an even small value since the value of *m* is already minimal before the threshold potential, greatly reducing the gap between different variables *h* (Figure 3.5.A). Alternatively, the K^+ ion current is positively correlated with the fourth power of *n*, which further enlarges the gap caused by the difference in the variable *n*. Therefore, it is the K ion channel (regulated by the variable *n*) that plays a decisive role in reducing the activation threshold of C.

One issue to note is that the K^+ ion currents (I_K) of different waveforms show different

behaviors after and before the membrane potential exceeds the threshold potential. As shown in Figure 3.6.C, after its membrane potential reaches the threshold potential, I_K corresponding to the waveform PAR 1:3 is much higher than that of the others, whereas all the K^+ ion currents did not show a difference before the threshold potential. Since the time to reach the action potential from its resting state changed only slightly with threshold strength, I_K does not affect the process after the model reaches the threshold potential, even though it does affect the speed from the threshold potential to the action potential.

In summary, an anodal stimulation before the input stimulation waveform can effectively lower the threshold of the unmyelinated nerve, while it does not greatly affect the threshold of Aδ. Although it has been suggested the anode break in peripheral sensory nerves may cause double peak potentials [61 62], previously thought to be elicited by depolarization of nerve terminal axons or skin receptors [63], the underlying ion mechanism has not yet been understood. Moreover, the double peak potentials were usually generated by low intensity, long duration stimulation, and the latency of the second peak was much longer than that of the first peak generated by cathodal stimulation [64]. These stimulation conditions are consistent with the favorable stimulation conditions for C in our research. Our study showed that if the double peak potentials are caused by anode breakage, then anodal stimulation to C generates them. A lower PAR can also widen the threshold strength gap. The use of asymmetric anodal polarity stimulation has a positive impact on the selective stimulation of nociceptive nerve fibers. However, as shown in Figure 3.4 and Figure 3.9, as the PAR decreases, the effect of polarity asymmetric stimulation on reducing the threshold strength of the unmyelinated nerves becomes saturated. For charge-balanced stimulation, a lower PAR requires a higher intensity of anodal stimulation, which might excite surrounding tissues such as muscle and Aβ nerve fibers related to the sensation of touch, pressure, and vibration.

3.4.3 The effect of stimulation waveform parameters on C-selectivity

Polar precedence, duration, polarity asymmetry related, and ISI to biphasic stimulation were investigated in detail.

(1) Polar precedence

In the experiment on polar precedence, the cathodal-first stimulation results (Figure 3.7.B) show that the threshold strength of the C is reduced and close to the threshold strength of Aδ but cannot be lower than it, which agrees with the results of other simulation studies and animal experiments [52 65], in which the anodal stimulus was

given after the cathodal stimulus to balance the charge injection for safety consideration. The results here were consistent with the general understanding that thicker fibers are more likely than thinner fibers to be stimulated to produce action potentials [26]. The threshold strength ratio of the responses to stimulation agrees well with the time constants of the ion channel variables of C and Aδ, which are shown in Figure 2.4. As shown in Figure 2.4, the time constants of *m* and *h* in the C-fiber model (the highest values are 0.5014 and 8.5820, respectively, in Figure 3.4.A) are higher than those of *m* and *h* in the Aδ-fiber model (the highest values are 0.2167 and 1.1510, respectively, in Figure 3.4.B), which means that the C-fiber model needs much more time to adapt to external stimuli.

In contrast, anodal-first stimulation favors C-selectivity and pushes the threshold of C to below that of Aδ. This phenomenon is similar to anode breakage [66], which showed the possibility of eliciting action potentials by only anodal stimulation. However, neither the role of charge balancing following cathodal stimulation nor the promotion of C excitation and C-selectivity over Aδ have been addressed. The phase portrait analysis shown in Figure 3.2 clearly shows that preceding anodal stimulation with a long enough duration, in conjunction with a following cathodal stimulation, can significantly promote C-selectivity.

(2) Duration

Although the duration of anodal stimuli strongly affects the promotion effect of C, the threshold strength of C is not linearly dependent on the duration. Comparing the results shown in Figure 3.7.A and Figure 3.10.A, a low PAR can greatly reduce the threshold strength of the C-fiber model (PAR: 1:1-1:9, threshold strength: 87.4-20.9 $\mu A/cm^2$), but they need the same duration (anodal duration: 8 ms) of stimulus to reach the minimum threshold strength. For the same total duration of stimulus such as 10 ms, the PAR 1:1 (anodal duration:5 ms, threshold strength: 95.0 $\mu A/cm^2$) and a much lower PAR, PAR 1:9 (anodal duration:1 ms, threshold strength: 77.9 $\mu A/cm^2$), did not show a large difference (17.1 $\mu A/cm^2$) in threshold strength. However, as the total duration becomes longer, such as 30 ms, the case of PAR 1:1 (anodal duration: 15 ms, threshold strength: 87.4 $\mu A/cm^2$, which is the same as all the cases with durations longer than 8 ms, according to the C threshold strength results shown in Figure 3.7.A) and the case with a lower PAR, PAR 1:9 (anodal duration: 3 ms, threshold strength: 38.0 $\mu A/cm^2$) showed a large difference (49.4 $\mu A/cm^2$). Thus, only when the anodal stimulation duration is long enough can PAR significantly improve C-selectivity.

On the other hand, neither anodal-first nor cathodal-first stimulation significantly promoted Aδ. When the stimulation duration increases, the charge of the anodal

stimulation also increases. That is, more cathodal stimulation charge is needed to counteract the anodal stimulation effect for Aδ; thus, the threshold strength of Aδ slightly increases. Although the effect of charge accumulation also affected C, it was offset by the promotion effect of anodal stimulation on C. In addition, the change in R_{th} shown in Figure 3.10.B gradually decreased, implying that stimulation with an extremely long anodal duration (ie, > 8 ms) hardly contributed to a further reduction in R_{th}. Note that for PAR 1:1 in Figure 3.7, the R_{th} also saturated at an 8 ms anodal duration, and it is reasonable to have a duration of anodal stimulation shorter than 8 ms.

(3) PAR

The PAR of stimulation is related to the preceding anodal stimulation in terms of both intensity and duration; thus, its effect on the threshold strength of C is nonlinear. There have been studies reporting the effects of pre-pulses with different intensities and durations on neurodynamics [34]. However, in the literature, PAR has not been studied as a comprehensive parameter of its effect on C-selectivity. In one relevant study [34], the effect of charge injection with asymmetrical waveforms was investigated through in vitro experiments. However, neither its effect on the excitability of C nor the underlying mechanism has been addressed. Thus, the role and underlying mechanism of PAR identified in this study can be a new dimension for designing effective selective stimulation.

Responding to stimulation with increasing anodal duration and decreasing intensity (a higher PAR value), the threshold strength of C gradually increases and exceeds that of Aδ, while the threshold strength of Aδ decreases slightly and remains unchanged after 5:1, as shown in Figure 3.9.B. Figure 3.9.C shows that R_{th} changes rapidly around PAR 1:1. This is also consistent with the change in ion current or K ion channel variable *n* in Figure 3.4.A and Figure 3.5.C. Since the duration of the cathodal stimulus is constant in the experiments shown in Figure 3.9.A, an increase in the threshold strength of C also indicates that the charge (or energy) accumulated by the cathodal stimulus is increased (Figure 3.9.D). In contrast, the threshold strength of Aδ decreases as the pulse width of the anodal stimulus increases and its intensity decreases. As shown in Figure 3.9.A, since the duration of the cathodal stimuli of all waveforms are the same, it was the anodal stimulus that made the difference. Furthermore, because the effect of duration saturated at a certain value, the intensity of the anodal stimulus played a major role, as shown in Figure 3.7. However, stronger anodal stimulation may have potential safety concerns. Regardless of anodal and cathodal stimuli, excessive stimulation intensity may affect other subcutaneous tissues or even cause damage to them [67]. From the anodal duration-R_{th} graphs for the PAR 1:1 (Figure 3.7.C) and PAR 1:9 cases (Figure 3.10.B), the

improvement of R_{th} might be saturated at an anodal duration of 8 ms. An anodal stimulus longer than 8 ms can have a better stimulation effect on C, and a lower asymmetric ratio can lead to better C-selectivity (Figure 3.9.C). However, when the above two conditions are met simultaneously, the stimulation waveform may be too long, which might cause safety issues [68]. Therefore, even though waveforms and parameters for achieving better C-selectivity were identified in this study, the range of the key parameters, such as the intensity and pulse width of the anodal stimulation, needs to be further investigated to ensure the safety and effectiveness of C-selectivity for surface stimulations.

As shown in Figure 3.11, the relationships between the threshold strength, R_{th}, and pulse frequency at three different PAR values are consistent with those shown in Figure 3.9. For the three PAR ratios of 1:6, 1:3, and 1:1, the value of R_{th} mostly depends on the threshold strength of the C-fiber model. In Figure 3.11.A1-C1, since there is no restriction on the stimulation duration, the threshold of the Aδ-fiber model remains the same as that of the C-fiber model at less than 20 Hz. On the one hand, long-term stimulation causes Faradaic charge transfer, leading to safety hazards [68]; on the other hand, a stimulation frequency less than 20 Hz does not further improve C-selectivity. We limited the stimulation duration to 50 ms in Figure 3.11.A2-C2. The result shows that the C-fiber model threshold is unchanged, but the Aδ-fiber model threshold is reduced at low frequencies and returns its maximum at 20 Hz, regardless of the PAR value. For the R_{th} of each PAR, the main changes came from the increase in threshold strength of the Aδ-fiber model when stimulated at frequencies larger than 15 Hz, 15 Hz and 12 Hz for PAR 1:6, 1:3, and 1:1, respectively. A shorter interstimulus interval results from the frequency band having a stronger effect on increasing the threshold strength of the Aδ-fiber model. This may be due to the extremely large time constant of parameter s in the Aδ-fiber model [48]. However, when the frequency is greater than 20 Hz, the threshold strength of the Aδ-fiber model begins to decrease, while the threshold strength of the C-fiber model increases. Especially at a low PAR (1:6), the magnitude of the change is the largest. As the frequency further increases, the R_{th} of Figure 3.11.A2 (PAR 1:6) changes more than that in Figure 3.11.B2-C2, leading to a smaller difference in their R_{th}. This reflects that when the frequency approaches the higher frequency band (>20 Hz), the influence of the frequency is larger; otherwise, it decreases. After comparing Figure 3.11.A2-C2, a lower frequency amplifies PAR's effects on R_{th} (the difference of R_{th}: 0.09616 between PAR 1:6 and 1:3 with 20 Hz, is larger than the difference of R_{th}: 0.04411 between PAR 1:6 and 1:3 with 50 Hz). Therefore, when using stimulation with a long total (anodal and cathodal stimulation) duration (50-100 ms from Figure 3.10.A),

selecting a low PAR and higher frequency (15 Hz-20 Hz) in the lower frequency band can improve C-selectivity. This is consistent with related experimental data [69], showing that stimulation at a frequency lower than 20 Hz is beneficial to the activation of unmyelinated nerves. Additionally, it is necessary to trade off the facilitative effect of C-selectivity and safety when performing stimulation below 15 Hz. However, as reported by other studies [60], in the higher frequency band (100-500 Hz), the frequency is an important factor to promote the excitation of Aδ while inhibiting C.

(4) ISI

Unlike the interval between two biphasic stimuli, the ISI between an anodal pulse and a cathodal pulse impacts stimulation safety. It has been shown that this ISI needs to be less than 10 ms and greater than 6 ms to meet the safety requirements of biphasic stimulation [68]. The aim of adding ISI into the cathodal-first stimulation waveform is to reduce the threshold strength of the following anodal stimulation [70]. However, to guarantee the safety of stimulation, the interval between cathodal and anodal stimuli cannot be too large. Therefore, choosing an appropriate duration of ISI is vital to improve the effect of cathodal-first stimulation. On the other hand, according to our results shown in Figure 3.8, a shorter ISI or even no ISI can maximize the selective stimulation effect for the biphasic anodal-first stimulation. A shorter ISI can not only improve C-selectivity but also reduce the impact on organs. This can be understood from the perspective of safety as follows. The anodal stimulation and cathodal stimulation should be as close as possible to ensure that the charge can be neutralized within a short time.

In addition, the interval between each biphasic pulse effects the stimulation results (such as the effect of the refractory period reported by Dudel [71]). For pulses with a low frequency of 1 Hz, nerves stimulated by the current biphasic pulse are less subjected to the influence of its previous biphasic pulse since there is enough time for the neuron to recover (Figure 3.11.A2-C2).

3.5 Conclusion

To clarify how a preceding anodal stimulation and a cathodal stimulation (called anodal-first stimulation) could lower the activation threshold of nociceptive C over myelinated nociceptive Aδ and to further clarify the landscape of the solution space, the C-fiber and Aδ-fiber models were employed to compare their responses to relevant waveforms in terms of both their behavior in the phase plane and C-selectivity. It was made clear that anodal-first polarity asymmetric stimulations are more likely to stimulate unmyelinated nerves because the preceding anodal stimulation could decrease their K^+ ion current for

the subsequent cathodal stimulation. The optimal parameters in terms of the activation threshold were identified in the low-frequency band, which showed an especially high possibility of C-selectivity. This is an important step towards long-term pain relief for chronic pain.

Chapter 4

Analysis of pre-pulse waveform

4.1 Overview

This chapter was written based on the paper which was under preparation “Gate mechanism and parameter analysis of pre-pulse waveform for selectivity stimulation”. I introduce the high frequency pre-pulse stimulation for increasing the threshold of Aδ.

4.2 Stimulation schemes

Figure 4.1 shows an example of the waveform under this study. The amplitude of the high frequency sine wave is *Vs*, whereas the duration of it is denoted using *Ts*. Figure 4.1.B presents an illustration of the change in membrane potential and K ion channel permeability variable *s* based on high-frequency sine wave stimulation. Three important moments a, b, and c are defined to explain the role of variable *s* in the Discussion section.

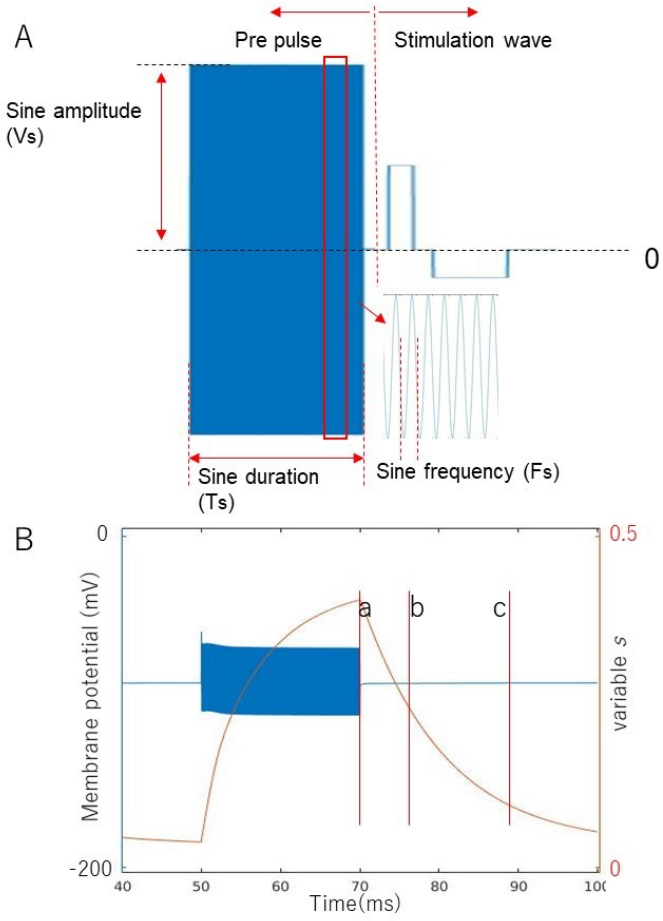

Figure 4.1 Waveforms of the stimulation schemes

A: inhibit-Aδ wave (i-Aδ) contains a high-frequency symmetric sine wave as its pre-pulse for Aδ inhibition. With frequency, intensity, and duration as the parameters, and BSW with optimal parameters identified through the investigation in the previous chapter as its main stimulation wave.
B: An illustration of the change in membrane potential and K ion channel permeability variable *s* by high-frequency sine wave stimulation. Marks *a*, *b*, and *c* were used to express the three moments after the high-frequency pre-pulse stimulation, *a*: 0 ms, *b* 10 ms, and *c* 30 ms.

4.3 Experiment results

4.3.1 Changes in ion current caused by the high frequency sine waveform

Figure 4.2 shows the phase portrait of the two nerve fiber models after applying a pre-pulse with 100 kHz and 29 mA/cm^2 sine waves for 20 ms, as illustrated in Figure 4.1.A. Three states are introduced in Figure 4.1.B, which are indicated as a, b, and c in Figure 4.2. These points represent the moment when the pre-pulse stimulation ended, 10 ms after sine stimulation ended, and 30 ms after sine stimulation ended and reached its resting state, respectively. The change of the threshold saddle point (from *c* to *a*) of the MRG model ($\Delta V_1 + \Delta V_2$ = 8.0 mV) is greater than that of the HH model (ΔV = 1.9 mV) with the same high-frequency sine stimulus. Regarding the recovery of the saddle point (expressing threshold) to its resting state, the MRG model (Δt_2 is approximately 35 ms) is slower than that of the HH model (Δt_1 is approximately 8 ms). Thus, the high-frequency sine wave stimulation has larger and longer effect on the change of the Aδ threshold than that of C. Phase portrait analysis disclosed the possibility that pre-pulses improve C-selectivity. In other words, pre-pulses may promote endogenous opioid secretion.

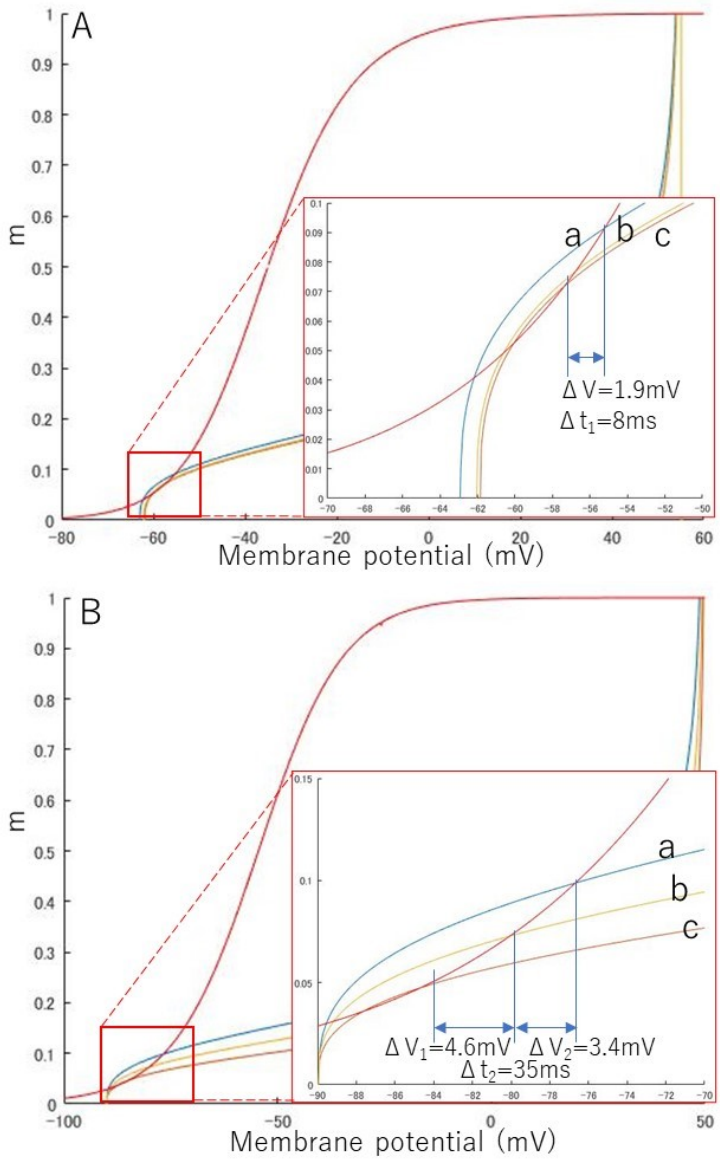

Figure 4.2 Phase portrait of the HH model and MRG model during pre-pulse stimulation with duration of 20 ms, frequency of 100 KHz and strength of 29 mA/cm^2

A: Phase portrait of the HH model, B: phase portrait of the MRG model. States a, b, and c were defined in Figure 4.1.B.

Figure 4.3 shows the ion current change by using high frequency sine waveform with 20 ms duration and 100k Hz frequency. Figure 4.2.A shows the Na^+ ion current, and Figure 4.3.B shows the K^+ ion current. Compare with A, the shape of B is more regular. Figure 4.3.C and D shows the K^+ ion current change by using high frequency sine waveform with 20 ms duration and 100k Hz frequency. The yellow mark and red mark denote the

current change at beginning and last of sine waveform. As the stimulation time increases, K^+ ion current deflects to the vertical direction.

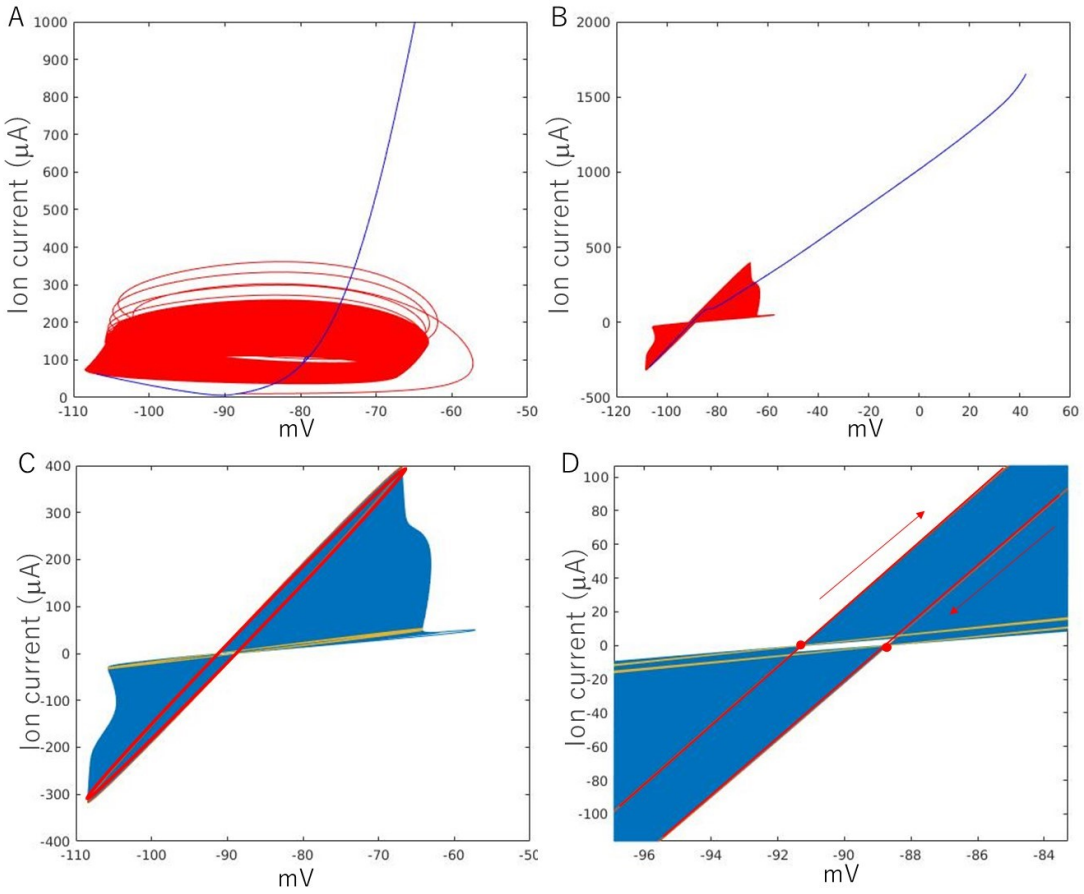

Figure 4.3 Changes in Na (I_{Na}) and K (I_K) ion channel currents with 20 ms duration and 100k Hz frequency sine waveform.

(A) Na^+ ion current. (B) K^+ ion current. In A and B, the red line shows the current change by pre-pulse with high frequency sine waveform, the bule line shows the current change with the main stimulation wave. (C) K^+ ion current with high frequency sine waveform. (D) An enlarged view of C near the rest potential (0, -90). The yellow line shows the current change at the beginning of high frequency sine waveform, and the red line shows the current change at the last of high frequency sine waveform.

4.3.2 The influence of waveform parameters for reducing Aδ excitability

In order to analyze the parameter effect of the high frequency sine stimulation, two experiments were designed by analyzing the effect of duration, frequency and a limited amplitude:

(1) The effect of duration and frequency

Figure 4.4 shows the gradient and R_{th} with different frequency and duration. The gradient was calculated from the results shown in Figure 4.3.C (the long diameter of the red ellipse). The stimulation wave was used for 5 ms DC stimulation, and the frequency of pre-pulse that uses high frequency sine wave was changed from 10k to 100k, and duration was changed from 5 to 20 ms for duration. The X-axis (duration) and Y-axis (frequency) in B is the opposite direction in Figure 4.4.A. This means that the maximum value in Figure 4.4.A corresponds to the minimum value in Figure 4.4.B.

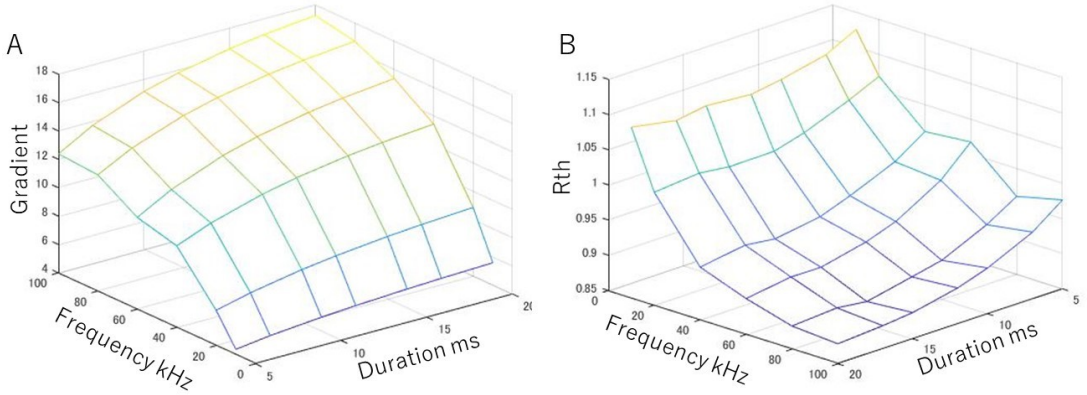

Figure 4.4 Relationship between (A) frequency, duration, and gradient, (B) frequency, duration, and R_{th}.

The gradient was calculated from the results shown in Figure 4.3.C. Note that the X-axis (duration) and Y-axis (frequency) in sub-graph B is the opposite direction in sub-graph A. The data in sub-graph B has the same trend as the data in sub-graph A.

(2) The effect of amplitude

Figure 4.5 shows that the R_{th} changes with different amplitude and frequency. The R_{th} change shows the change between the stimulation with and without pre-pulse waveform. Every pre-pulse waveform used 20 ms duration stimulation, and main stimulation waveform used a 5-ms duration cathodal DC stimulation. The maximum allowable current that will not adversely affect the human body is 5 mA, according to the relevant regulations of the International Electrotechnical Commission (IEC) [72]. Thus, I also limited the amplitude of every pre-pulse waveform lower than 5 mA/cm^2 to observe the effect under limited conditions. The frequency changed from 2 kHz to 20 kHz. Due to the limitation of intensity, the lower frequency shows a better R_{th} value. However, it needs to be careful that the pre-pulse shall not lead to the generation of action potentials in the C and Aδ.

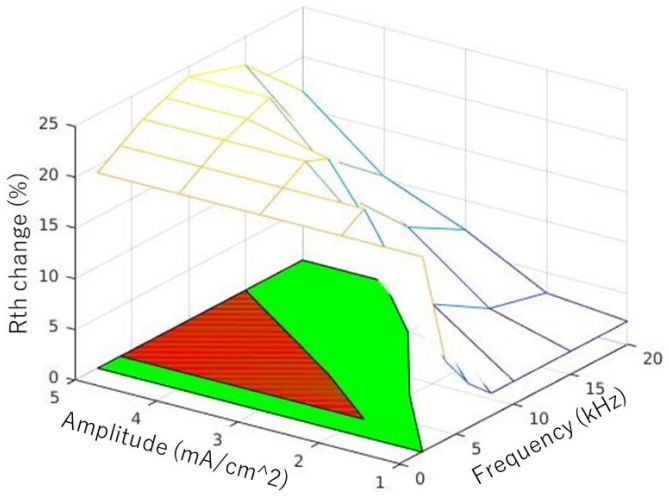

Figure 4.5 Relationship between frequency, duration, and R_{th} change.
The red area shows the amplitude and frequency parameters which can make the R_{th} change greater than 20%, and the green area shows the parameters which can make it greater than 10%.

4.3.3 The influence of different waveform with pre-pulse

Figure 4.6 shows the R_{th} with different frequency and duration by different polarity asymmetry ratio (PAR, anodal duration: cathodal duration) which was discussed in section 3.2. The PAR was set with (A) 1:1; (B) 1:3; (C) 1:6; (D) 1:9. The anodal duration of each stimulation waveform was fixed at 8 ms (refer to the results from Chapter 3, Figure 3.7 and Figure 3.10). This means the cathodal duration was set to (A) 8 ms; (B) 24 ms; (C) 48 ms; (D) 72 ms. The pre-pulse which using high frequency sine wave was changed from 10k to 100k for frequency and 5 to 20 ms for duration. Except for A, there is almost no change of R_{th} in the others. The change pattern of A is the same as that of Figure 4.4.B.

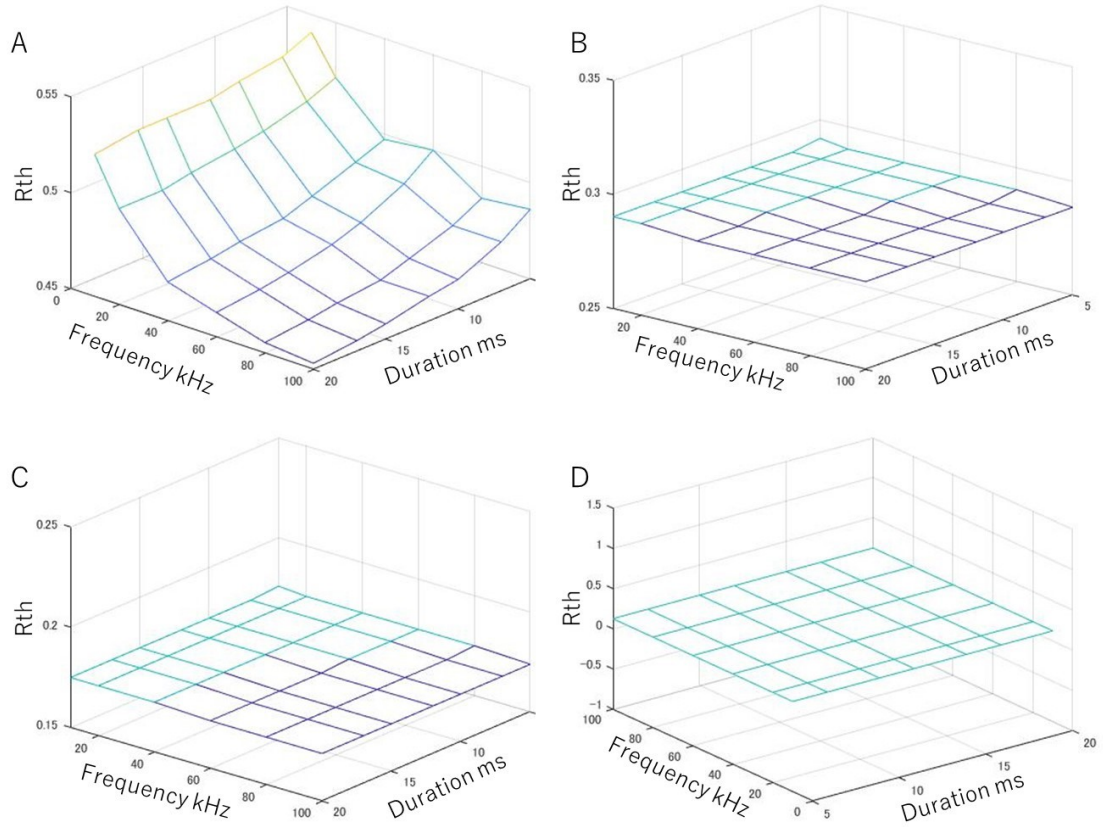

Figure 4.6 Relationship between frequency, duration, and R_{th} by different main stimulation waveform.

(A) PAR: 1:1; (B) PAR: 1:3; (C) PAR: 1:6; (D) PAR: 1:9. There is almost no change of R_{th} in B, C and D.

4.4 Discussion

4.4.1 The changes in ion current caused by the high frequency sine waveform

As shown in Figure 4.2, high-frequency sine pre-pulse waves cause the resting state isocline of dV_m/dt = 0 to increase from state c to state a. This effect increased the threshold of both the C and Aδ. The change in threshold of the Aδ is considerably increased compared with C ($\Delta V_1 + \Delta V_2$ = 8.0 mV vs. ΔV = 1.9 mV). In addition, the recovery time of the Aδ, which is the period of time for the threshold at state a to return to state c, is longer than that of C (35 ms vs. 8 ms). This difference in the phase portrait shows that the threshold of both C and Aδ increases after receiving the high-frequency sine stimulus, while the threshold of Aδ is more affected and longer. This feature greatly benefits C-selectivity, providing a powerful influencing factor that promotes the secretion of endogenous opioids.

From Figure 4.3.C and D, the K^+ ion current changed with the elliptical orbit. As the stimulation duration of the high frequency sine waveform increased, the long diameter of the ellipse rotated from horizontal to vertical. The rotation speed changes rapidly from the beginning of the sine waveform, and gradually slower after a long duration. From Figure 4.3.B, the ion current (blue line) still changes along the long diameter of the ellipse at the beginning of the main stimulation wave. At about -85mV (near threshold), the rate of ion current change decreases. The trend of this change is consistent with the change of the phase portrait in Figure 4.2.B. This result shows that the increase of K^+ ion current directly affects the threshold of Aδ, and it plays a key role in improving C-selectivity.

4.4.2 The effect of stimulation waveform parameters for reducing Aδ excitability

From Figure 4.4.A and B, under the same stimulus conditions, the gradient is completely opposite to R_{th}. It can completely correspond to the figure of B by flipping the figure of A. This result shows that the change of gradient can well reflect the change of R_{th}. It also consistent with the conclusion obtained in Figure 4.3. Back to the change in gradient in A, whether it is high frequency or long duration, it makes the impact of the other parameter increase. Secondly, the change in frequency direction is greater than the change in duration direction. At low frequency (such as 10k Hz), the gradient changes little over duration. In contrast, at short duration (such as 5 ms), the gradient changes will be much larger over frequency. Taking into account the safety limitations that may be added in the future, high-frequency stimulation should be given priority to improve the efficiency of stimulation for high C-selectivity .

From Figure 4.5, when the pre-pulse stimulation amplitude is low, it can be obtained a better result only when the frequency is also at a lower value. This trend is opposite to that in Figure 4.4.B. It also shows the contradiction between frequency and intensity. That is to say, although high frequency can bring better C-selectivity, it also greatly increases the demand for stimulus intensity, thereby leaving dangers in safety.

4.4.3 The influence of different waveform with pre pulse

From Figure 4.6, the experimental conditions combine the conclusions of the section 3.2 which shows lower PAR led to higher C-selectivity. However, when using stimulation conditions that are conducive to main stimulation waveform such as 1:9, the change of frequency and duration will not affect the change of R_{th}. Although the result is still lower than the R_{th} with only the main stimulation waveforms show in section 3.2 which shows it has a better C-selectivity, the magnitude of the change in R_{th} is smaller. In Figure 4.6.B,

the duration of main stimulation waveform was 32 ms, which shows a similar duration (Δt_2 = 35 ms) from a to c in Figure 4.2.B. In other words, when the main stimulation duration makes the phase portrait almost return to the rest state, the influence of K^+ ion current also almost disappears. High frequency sine wave stimulation does not affect the main stimulation with a long duration. It needs a trade-off between pre-stimulation wave, main stimulation wave and safety limitation.

4.5 Conclusion

In this section, to investigate the possibility to improve selectivity of C fibers over Aδ fibers by using a high frequency sine waveform, we compared and analyzed the effect with different frequency, duration and amplitude. We think that the K ion channel plays a key role in stimulation for high C-selectivity by phase portrait and ion current analysis. It is obtained parameters setting which improve C-selectivity when only considering the influence of pre-pulse stimulation. However, the result does not match very well with the result of Chapter 3. It needs a trade-off between pre-stimulation wave, main stimulation wave and safety limitation in the future.

Chapter 5

Analysis of BMAC waveform

5.1 Overview

This chapter was written based on the publication “A simulation study on selective stimulation of C-fiber nerves for chronic pain relief” on IEEE Access [60]. There are also some results from a paper under preparation, “Gate mechanism and parameter analysis of pre-pulse waveform for selectivity stimulation”. A carrier wave BMAC was used to carry both the anodal-first stimulation and high frequency pre-pulse to verify the influence of BMAC on the C-selectivity.

The stimulation waveforms of the BMAC (anodal-first stimulation with carrier wave) and high frequency pre-pulse were combined and the effect on C-selectivity was analyzed.

5.2 Potential stimulation schemes to realize selective stimulation for long-term pain relief

In this section, the waveforms, parameters, and features of the three potential stimulation schemes, including BSW, BMAC, and i-Aδ, are schematically explained.

(1) BSW

Figure 5.1.A shows the stimulation waveform of the BSW. The square wave was used based on the reason provided in Chapter 3. Each period contains a preceding anodal stimulus and a following cathodal stimulus. The polarity asymmetry ratio is the quotient of the amplitude of the cathodal stimulus and the anodal stimulus, which has not been investigated in depth in the literature. Square waves with different stimulus frequencies (from 5 to 500 Hz) and polarity asymmetry ratio values (from 1:6 to 6:1) were investigated in terms of C-selectivity.

(2) BMAC

Figure 5.1.B shows the stimulus waveform of the BMAC. Three decisive parameters are burst frequency， carrier frequency and the ratio of ISI. The investigated range of burst frequency is 5 to 500 Hz, while investigated range of the carrier waves is 100 to 10 kHz. In addition, their interaction with burst waves and subsequent effects on C-selectivity were investigated.

(3) I-Aδ

The inhibit-Aδ wave (i-Aδ) shown in Figure 5.1.C contains a high-frequency sine wave as its pre-pulse for Aδ inhibition; frequency, intensity, and duration as parameters; and BSW or BMAC with optimal parameters identified through the previous investigation as

its main pulse. In the chapter, the stimulation intensity, pulse duration and frequency of the pre-pulse are investigated. Table 5.1 provides the assessed parameters. BSW and BMAC waves as the main stimulation pulse with a burst frequency of 50 Hz and duration of 20 ms were tested.

Table 5.1 parameters for i-Aδ pre-pulse stimulation

Strength	Duration	Frequency
	20 ms	100 kHz
29 mA/cm^2		100 kHz
29 mA/cm^2	20 ms	

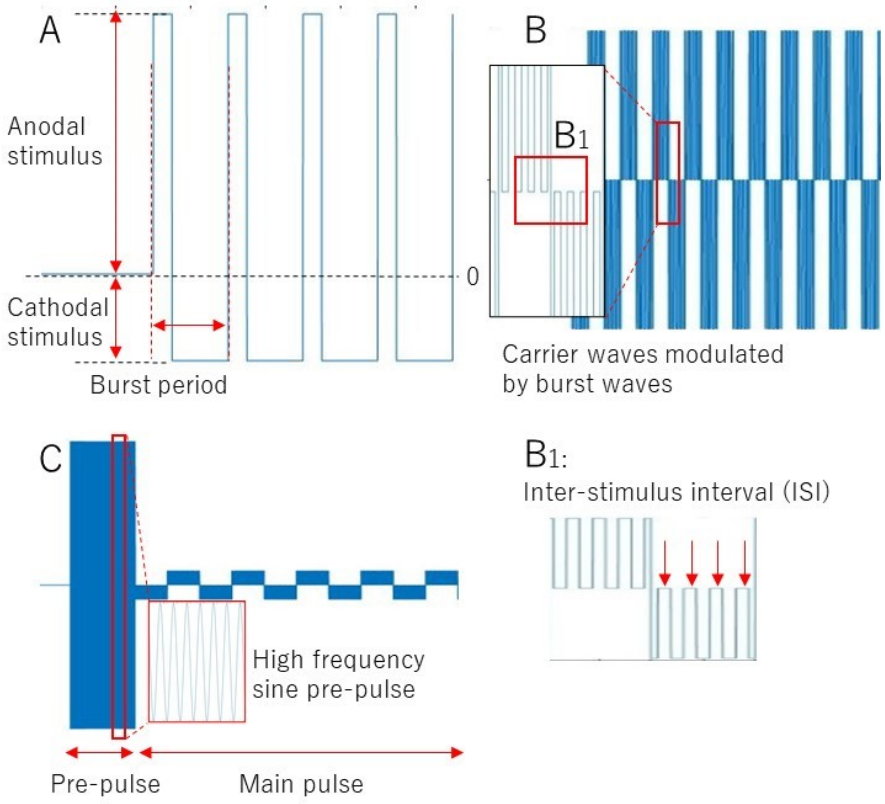

Figure 5.1 Waveforms of the three stimulation schemes

A: Bipolar Square Wave (BSW): each period contains an anodal stimulus and a cathodal stimulus. The polarity asymmetry ratio is the quotient of the amplitude of the cathodal stimulus and the anodal stimulus.

B: Burst-Modulated Alternating Current (BMAC): burst frequency, carrier frequency, and carrier waves modulated with burst waves. B1: Inter stimulus interval (ISI) describes the no stimulus duration of the carrier wave.

C: inhibit-Aδ wave (i-Aδ) contains a high-frequency symmetric sine wave as its pre-pulse for Aδ inhibition. With frequency, intensity, and duration as the parameters, and BSW or BMAC with optimal parameters identified through a previous investigation as its main pulse.

5.3 Experiment results

5.3.1 Effects of three stimulation schemes on C-selectivity

The three potential stimulation schemes, BSW, BMAC, and i-Aδ, were tested respectively:

(1) BSW

Figure 5.2.A shows the acquired thresholds of the C-fiber and Aδ-fiber models, marked with _HH and _MRG in the figure, respectively, stimulated by sine and square waves at a different frequency. As shown in the figure, C has a lower activation threshold than Aδ by square stimulation when the stimulation frequency is less than 100 Hz. However, C showed a lower activation threshold than Aδ by sine stimulation only for the frequency range of 50-100 Hz. In addition, the thresholds of the sine stimulus are always greater than those of square stimulation at the same frequency.

Figure 5.2.B shows the threshold of the C-fiber and Aδ-fiber models when PAR was changed. Note that the charge balance of BSW was maintained for stimulation safety, thus resulting in an equal integral value of the anodal and cathodal stimuli. The total stimulus duration is 20 ms. The trend of the threshold change caused by the sine stimulus and the square stimulus is similar, but the threshold values of the sine stimulus are always greater than it of the square stimulus. As PAR from 1:6 to 2:1, C showed a lower threshold than Aδ. There is a crossover between 2:1 and 3:1. After the crossover, C showed a higher threshold than Aδ, thus it is more difficult to activate C than Aδ.

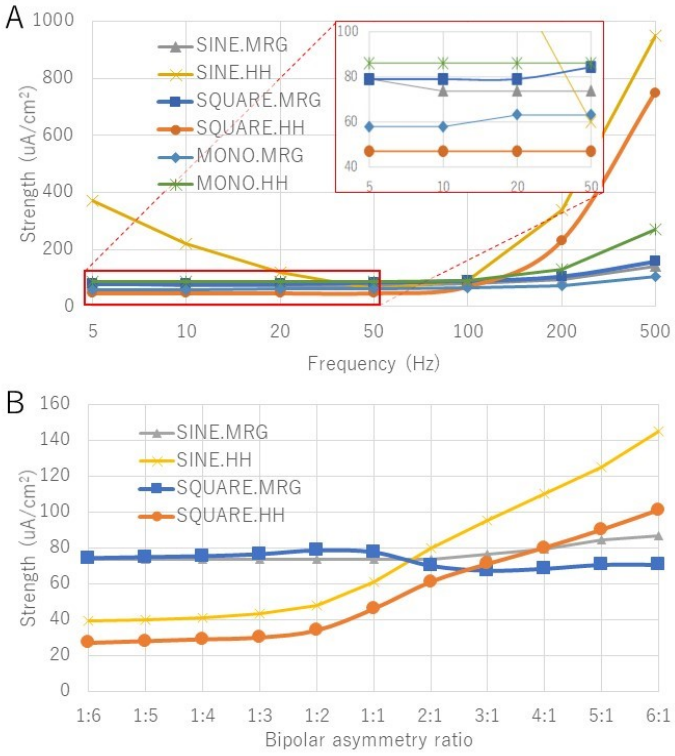

Figure 5.2 Activation threshold as a function of frequency and polarity asymmetry ratio for BSW and sine wave

A: The strength of the simulated activation threshold of C and Aδ by stimuli with different frequencies (5-500 Hz) using square and sine stimuli with the same duration of the anodal and cathodal stimulus.

B: The strength of the simulated activation threshold of C and Aδ using different polarity asymmetry ratio values with square and sine stimuli. Note the charge of the anodal stimulus and the cathodal stimulus is balanced for different polarity asymmetry ratio values.

(2) BMAC

It is necessary to verify the effect of the carrier waves on selective stimulation following the advantage of high-frequency waves in deep stimulation. Figure 5.3 shows the threshold change with 5, 20, and 50 Hz burst waves when pulses containing carrier waves were stimulated by different frequencies (100 Hz-50 kHz). The C and Aδ have a similar activation threshold at lower carrier frequencies. However, the threshold of the Aδ increases more than that of C during the carrier frequency increases. Figure 5.4 shows the activation threshold of the two models when they were stimulated by burst waves with different frequencies and PAR. The carrier frequency is set to 10 kHz. The

results are identical to those of the BSW shown in Figure 5.2.

Figure 5.5 shows the activation threshold of the two models when stimulated by the carrier waves with different ISI. The burst frequency of BMAC is set to 50 Hz, and the carrier frequency is set to 10 kHz. The activation threshold decreases as the stimulus duration of ISI increases. However, the charge required for stimulation remains the same.

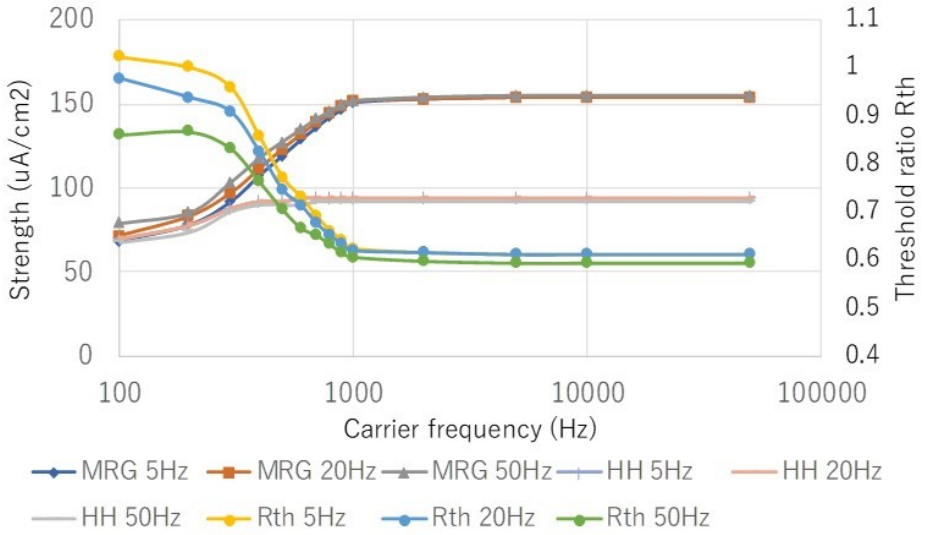

Figure 5.3 The strength of the excitation threshold of C and Aδ fibers changed with the frequency of carrier waves and burst waves. The horizontal axis represents carrier frequencies. Burst frequencies of 5, 20, and 50 Hz were simulated.

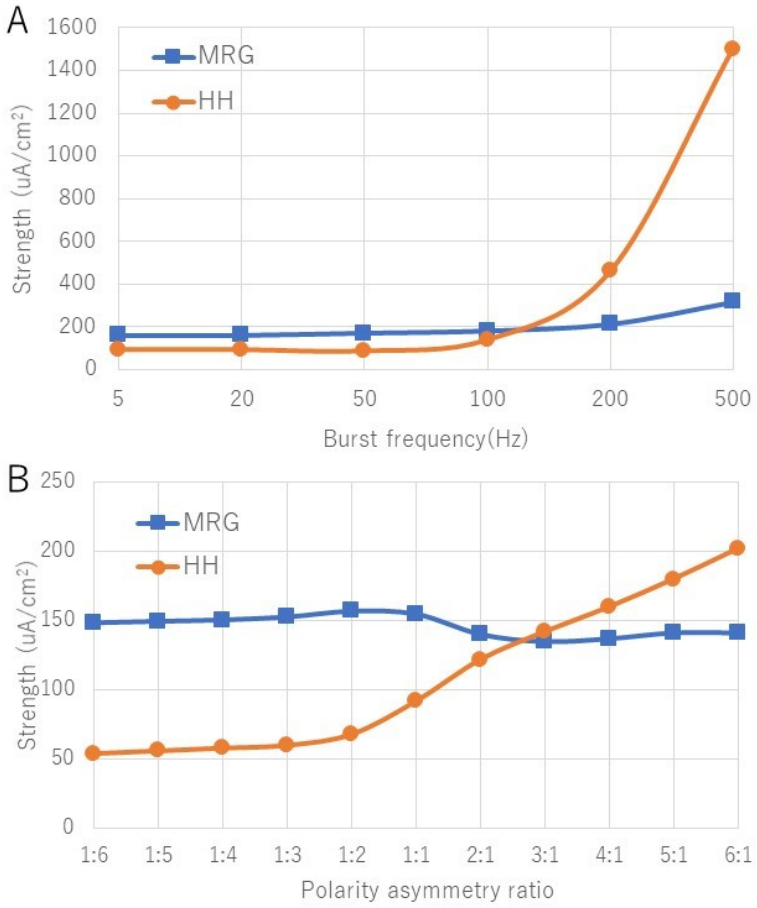

Figure 5.4 Activation threshold as a function of the frequency of burst waves, polarity asymmetry ratio, and BMAC. Carrier wave frequency is 10 kHz.

A: The strength of simulated activation threshold of C and Aδ by stimuli with different burst wave frequencies (5-500 Hz) using a stimulus with the same duration of the anodal and cathodal stimulus.

B: The strength of the simulated activation threshold of C and Aδ using different polarity asymmetry ratio values. Note the charge of the anodal stimulus and the cathodal stimulus is balanced for different polarity asymmetry ratio values.

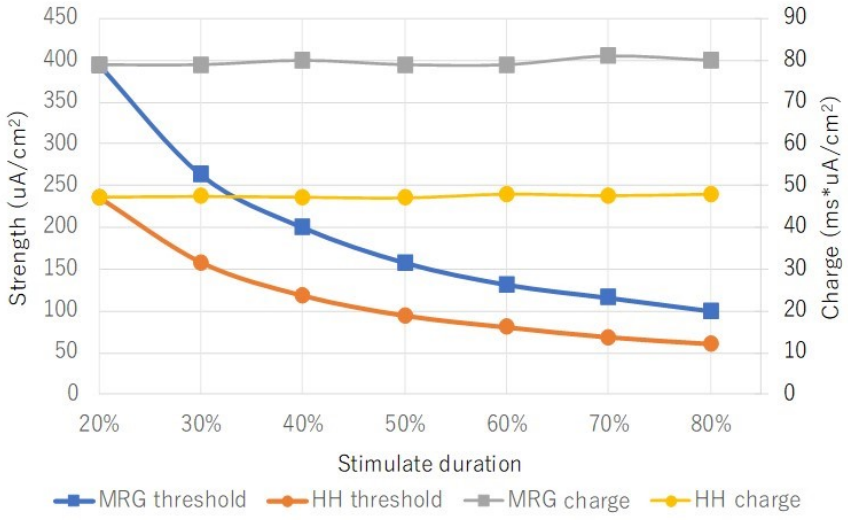

Figure 5.5 The first vertical axis shows the strength of the excitation threshold of different inter-stimulus intervals (ISI) of the carrier wave.
The horizontal axis shows the ratio of the stimulation carrier wave. The second vertical axis shows the stimulus charge with different ISI.

(3) i-Aδ

Figure 5.6 shows the effect on the K ion channel permeability variable *s* by different parameters of the pre-pulse: frequency, duration, and intensity. The opening of the K ion channel leads to an increase in the activation threshold.

As shown in Figure 5.6.A1-C1, stronger and more long-duration stimuli with a lower frequency result in a higher variable *s* of Aδ. BMAC is used as the stimulus with a duration of 20 ms, carrier frequency of 10 kHz, and PAR of 1:1. Using the strength-*s* and strength-R_{th} graphs (Figure 5.6.A1 and A2) as examples, the higher strength of high-frequency pre-pulse stimulation could increase the value attained by variable *s* of the myelinated nerves. The Aδ could be activated when the variable *s* reached a certain value. Therefore, the strength-*s* curve shows a plateau phase at high stimulation strength, indicating activation of the myelinated nerves by the pre-pulse stimulation. This situation should be avoided since the purpose of introducing the pre-pulse is to improve C-selectivity. As the duration of pre-pulses increases (Figure 5.6.B1 and B2), the variable *s* first increases rapidly then slowly, and eventually saturates at a certain value depending on the intensity and frequency of the stimulus. The change of the threshold ratio R_{th} is consistent with the change in variable *s*. The frequency-*s* and frequency-R_{th} curves (Figure 5.6.C1 and C2) exhibit an inverse tendency compared with graphs of strength and duration.

Figure 5.6.A2-C2 present the threshold ratio R_{th} with BMAC or BSW as the main stimulation pulses, and the parameters of pre-pulse that are the same as those explored in Figure 5.6.A1-C1, respectively. BMAC is used as a stimulus with duration of 20 ms, carrier frequency of 10k Hz, and PAR of 1:1.

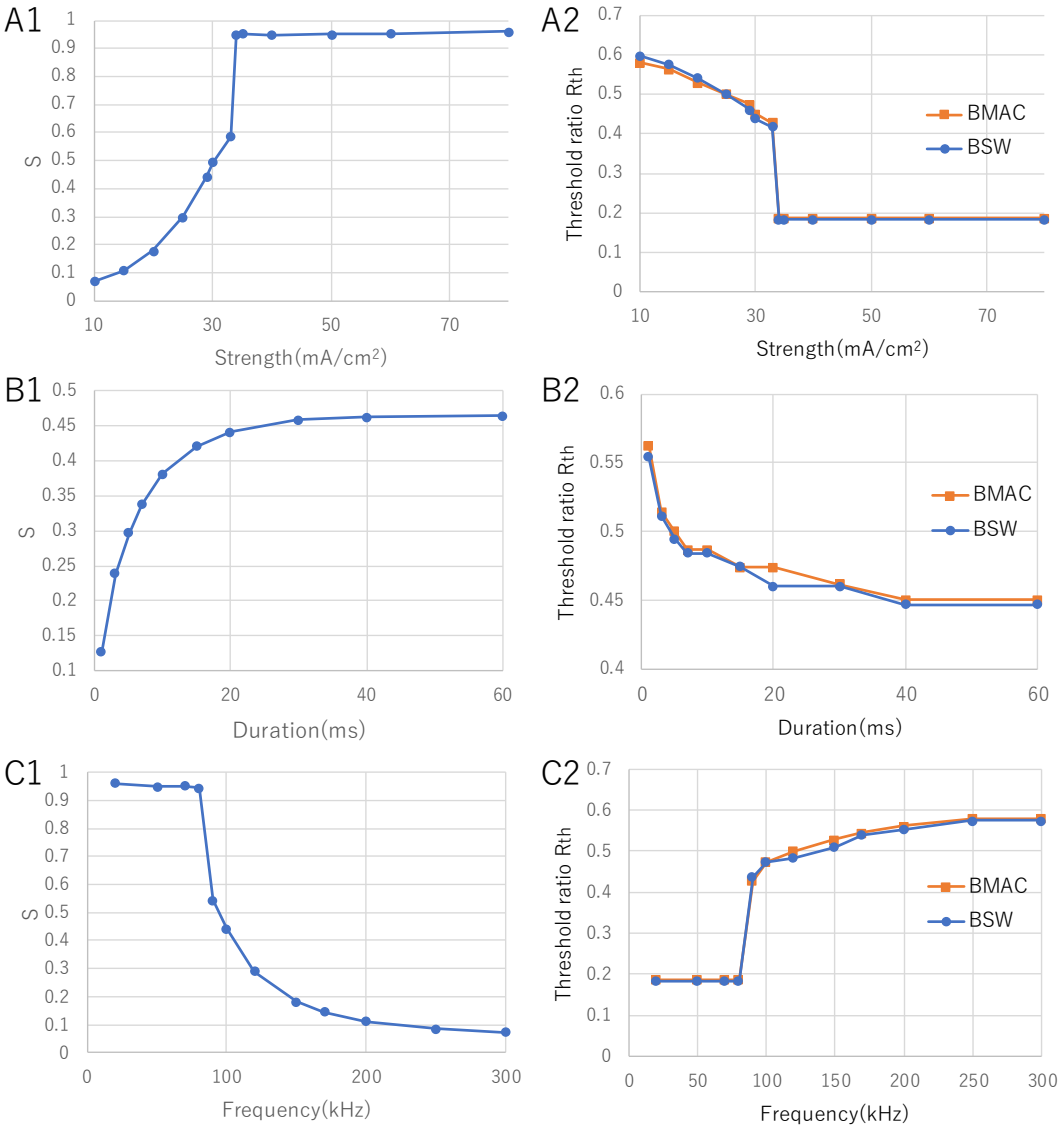

Figure 5.6 Changes of variable *s* and R_{th} with high-frequency pre-pulses of i-Aδ scheme

A1: The relationship between stimulation strength and K ion channel permeability variable *s*.

B1: The relationship between stimulation duration and variable *s*.

C1: The relationship between frequency of pre-pulses and variable *s*.

Figure 5.7 shows the change in R_{th} when stimulated by a pre-pulse wave with different strength values. The other parameters of the pre-pulse waves include duration of 20 ms and frequency of 100 kHz followed by an asymmetric BMAC wave with burst duration of 20 ms and different PAR (1:1, 1:3, and 1:6). The strength 0 means that there is no pre-pulse wave before the BMAC. The results are similar with the results shown in Figure 5.2.B and Figure 5.4.B. PAR of 1:3 and 1:6 exhibited reduced R_{th} values (0.3931 and 0.3638, respectively) compared with that of 1:1 (0.6075). Moreover, the three curves show the same tendency.

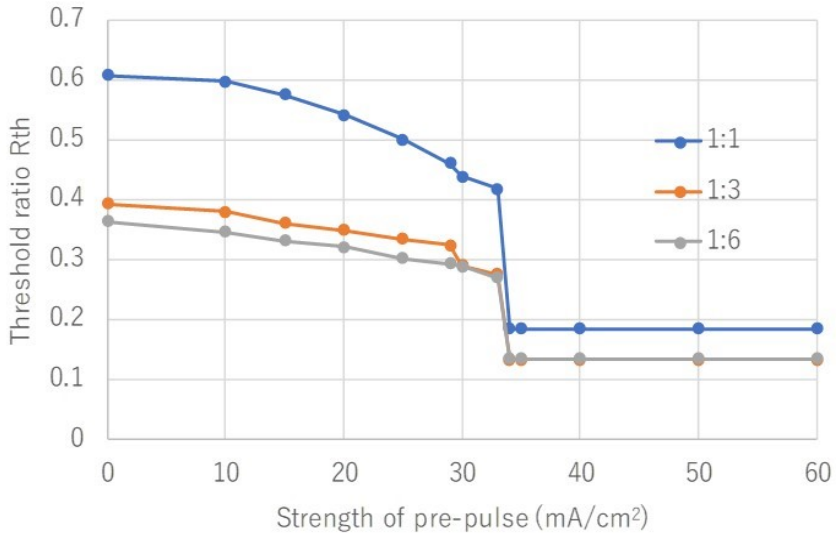

Figure 5.7 R_{th} results from main pulse BMAC with different polarity asymmetry ratio values, and pre-pulse stimulation with different stimuli strength with duration of 20 ms and a carrier frequency of 10 kHz

Figure 5.8 shows the change in R_{th} with BMAC used different total duration and different polarity asymmetry ratio when stimulated with a pre-pulse wave with different frequency. Figure 5.8.A and B show the same result with different views. There are different layers that show the change of R_{th} under different frequencies pre-pulse. The R_{th} decreases with frequency increasing. Follow the decreasing of R_{th}, the frequency of pre-pulse was 0, 2k, 5k, 10k, 20k, 40k, 60k, 80k, and 100k Hz, respectively. The pre pulse intensities were selected that do not generate action potentials, and they are 0, 0.93 mA/cm^2, 2.04 mA/cm^2, 3.69 mA/cm^2, 6.94 mA/cm^2, 12.80 mA/cm^2, 18.00 mA/cm^2, 23.20 mA/cm^2, and 28.30 mA/cm^2, respectively. All pre-pulses were applied by 20 ms duration. The R_{th} was greatly reduced by adding pre-pulse, and the change of R_{th} was gradually decreased with the frequency of pre-pulse increased. Figure 5.8.C shows the result in A with 20 ms duration and 1:1 PAR, and Figure 5.8.D shows the result in B with

32 ms duration and 1:9 PAR. The R_{th} remains constant after the frequency reaches 80k Hz in C. In contrast, R_{th} remains constant after the frequency reaches 10k Hz in D. There will be already a significant R_{th} changes by using low frequency pre-pulse when the stimulation waveform used a low PAR wave (such as 1:9).

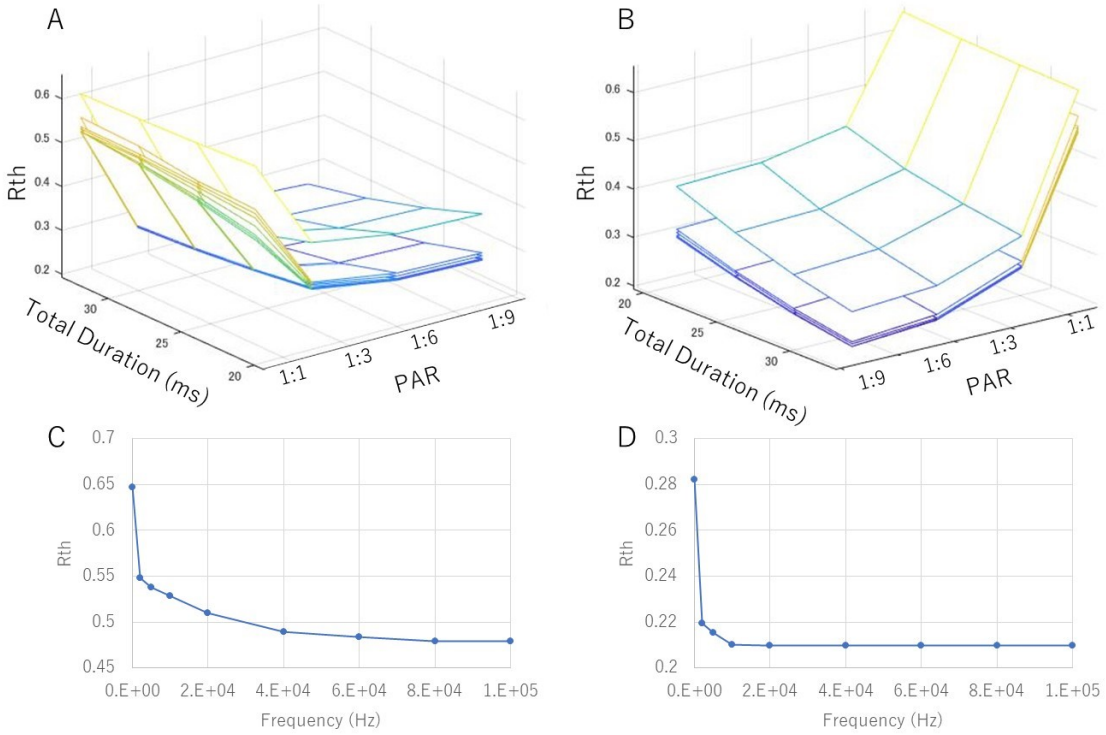

Figure 5.8 R_{th} with different total duration and different polarity asymmetry ratio by using different frequency pre-pulse.

A: The R_{th} by using different frequency pre-pulse. Different layers represent the results by different frequencies. Along the direction of R_{th} falling, the pre-pulse was applied by 1) no pre-pulse; 2) 0.93 mA/cm^2, 2k Hz; 3) 2.04 mA/cm^2, 5k Hz; 4) 3.69 mA/cm^2, 10k Hz; 5) 6.94 mA/cm^2, 20k Hz; 6) 12.80 mA/cm^2, 40k Hz; 7) 18.00 mA/cm^2, 60k Hz; 8) 23.20 mA/cm^2, 80k Hz; and 9) 28.30 mA/cm^2, 100k Hz. All pre-pulses were applied by 20 ms duration.

B: shows the same result with different view of A.

C: The R_{th} shows the result in A which the stimulation waveform was 20 ms duration and 1:1 PAR.

D: The R_{th} shows the result in B which the stimulation waveform was 32 ms duration and 1:9 PAR.

5.3.2 Phase portrait analysis results with BMAC

C-selectivity with BMAC could be explained and confirmed by phase portrait analysis. Figure 5.9 shows the phase portrait of the two nerve models for the Na ion channel variable *m* and the membrane potential V_m. The parameters of anodal stimuli are set as following, BMAC with duration of 20 ms, carrier frequency of 10 kHz, and PAR of 1:1. In Figure 5.9.C, points *d* and *f* express the resting state and the peak of an action potential, respectively. Point *e* is a saddle point, expressing the threshold of activation in a neural transmembrane system. The arrows shown in figure denote the state change trends.

Although the Aδ-fiber model has a lower polarization equilibrium point (V_m: -84.6 mV) than the C-fiber model (V_m: -57.3 mV) when the other channel variables are in their resting states (*h*: 0.5979 and *n*: 0.317 for C-fiber model; *h*: 0.9175, *p*: 0.0914, *s*: 0.007 for Aδ-fiber model), which means that it has a lower threshold and is more likely to be excited. On the other hand, the C-fiber model exhibits greater variability (>4 $\mu A/cm^2$). Thereby, when given an anodal stimulus with sufficient intensity, its equilibrium points that indicate the threshold of the nerve fiber disappear in the phase portrait. In contrast, the change in the Aδ-fiber model is minimal, and its equilibrium points show minimal changes, too. As shown Figure 5.9.E, when the anodal stimulus is not sufficient to cause unmyelinated threshold reduction, the equilibrium points of the phase portrait did not disappear. These findings demonstrate the behavior of the C-fiber model in response to a 4 $\mu A/cm^2$ anodal stimulus. The variability in the C-fiber model indicates that it is possible to change its activation threshold by controlling the stimulation parameters.

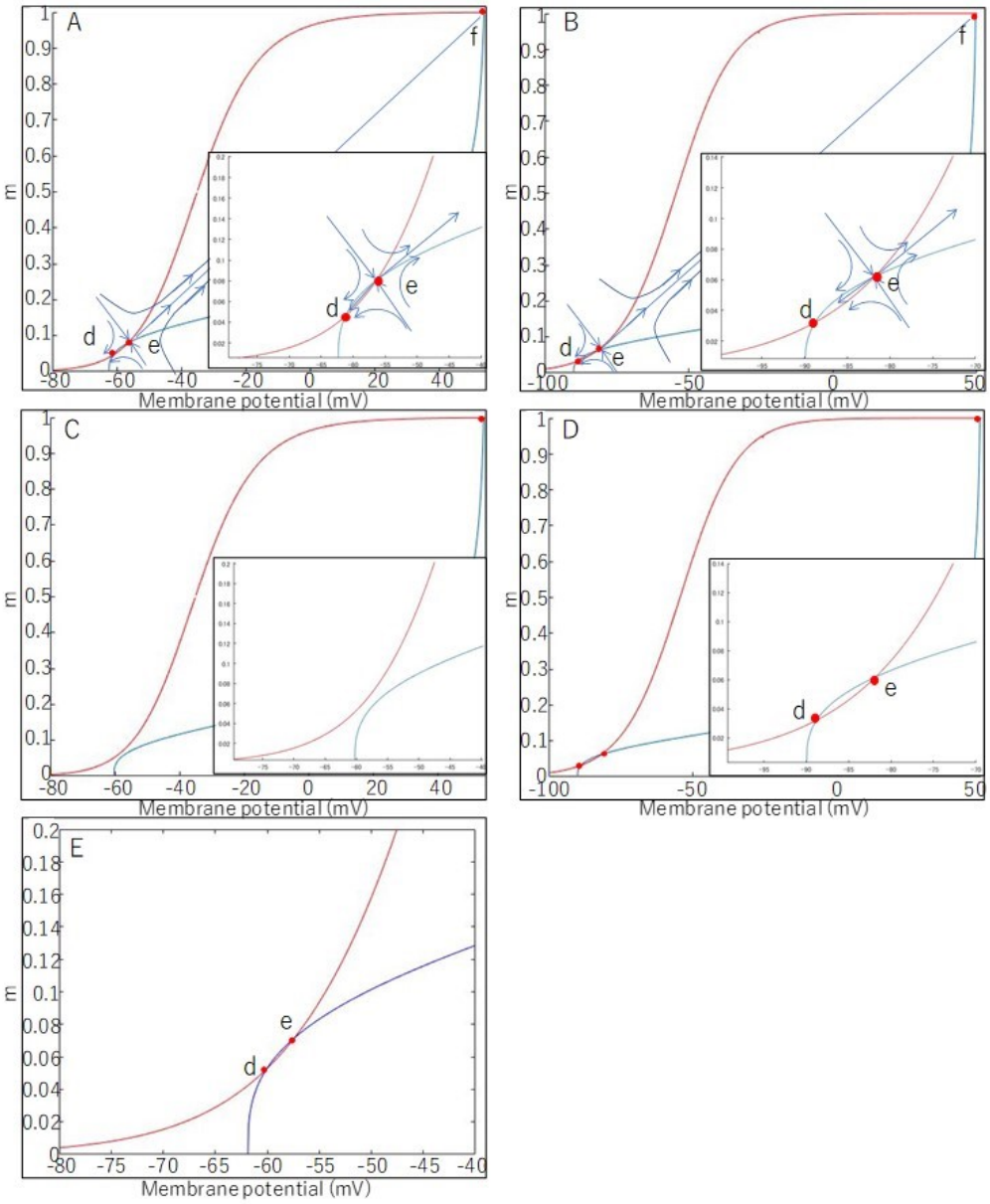

Figure 5.9 Phase portrait of the HH model and the MRG model in their resting state and during the anodal stimulus

A: The behavior of the HH model in the resting state. The red curve refers to the resting state isocline of dm/dt=0, and the blue curve refers to the resting state isocline of dV_m/dt=0. The three points *d*, *e* and *f* represent the resting point (i.e., dm/dt=0 and dV_m/dt=0, the status does not change over time). Points *d*, *e*, and *f* represent the situation at rest, activation threshold and peak action potential, respectively. Arrows refer to the trends of status change.

B: Behavior of the MRG model in the resting state.

C: Behavior of the HH model during the anodal stimulus.

D: Behavior of the MRG model during the anodal stimulus.

E: Behavior of the HH model with a low-intensity anodal stimulus (4 $\mu A/cm^2$).

5.4 Discussion

In the previous research, the effect of the pulse duration on different individual nerves was studied [55, 56]. The threshold of one single unmyelinated nerve (such as C) was greater than that of one single myelinated nerve (such as Aδ) at any pulse duration, and their threshold values became similar only stimulated with a longer duration [55, 56]. This difficulty is experienced in C-selective stimulation. Other decisive factors are needed to reduce the threshold of C over Aδ. Through the systematic investigation of the effect of the three stimulation schemes, we expected to identify such potential important factors for improving C-selectivity. The stimulus waveform that effectively facilitates the secretion of endogenous opioids was determined.

5.4.1 Effects of the three stimulation schemes

The three potential stimulation schemes, BSW, BMAC, and i-Aδ, were used to detect the influence on C-selectivity respectively.

(1) BSW

BSW was compared with sine waves and monopolar pulses in Figure 5.2, and the effect of PAR was assessed.

As shown in Figure 5.2.A, when the frequency is increased to greater than 100 Hz, which means that the duration of the bipolar BSW stimulus is less than 5 ms, the threshold of the C-fiber model is greater than that of the Aδ-fiber model. This requirement of long-duration and low-frequency stimulation is consistent with a previous report [28] that emphasized the effect of a sine wave with very low frequency (5 Hz) on C. However, sine waves have a reduced stimulation effect compared with square waves in this research. C activation relies on the difference between the values of the variables *m* and *h*, reflecting the opening and closing of the fast Na ion channels, respectively (Figure 2.4.A). Given its slowly increasing stimulation intensity, the low-frequency sine wave allows the variable *h* to change for a longer period, which led to a smaller difference between the *m* and *h*. Thereby, it is more difficult to activate C compare with square waves. Therefore, the square wave stimulus is more suitable for high C-selectivity.

Some researchers denoted that pre-pulses with different strength and duration have various effects on nerve dynamics [25, 34, 38]. Our simulation results in Figure 5.2.A showed that the anodal stimulus has minimal inhibitory effects on the Aδ-fiber model (SQUARE.MRG greater than MONO.MRG) but a significant excitation effect on the C-

fiber model (SQUARE.HH lower than MONO.HH). The anodal stimulus can reduce the threshold of the C, which can be further made clear by phase plane analysis in section 3.3.1. As shown in the figure, a greater effect is achieved by an anodal stimulus with increased strength and longer duration. Therefore, bipolar pulses are more effectively stimulate C fibers than monopolar pulses.

More importantly, the role of the PAR in C-selectivity was clarified through our systematical investigation of BSW; this is a necessary consequence of the following arguments.

First, considering the safety of the stimulus waveforms, the stimuli bipolarity is a necessity for both maintain the charge (the product of strength and duration) balance between the anodal and cathodal part of their stimulation waveforms [35]. It also benefits to improve nerve excitability [25]. Secondly, in the case of symmetric polarity balance, a strong anodal stimulus required the matching of a strong cathodal stimulus that is about to activate the Aδ and lead to unnecessary sharp pain. Third, the strength of stimulation has a greater influence on the threshold of C shown in Figure 5.2.B. When the strength of the anodal stimulus is strong and its duration is short (i.e., PAR of 1:6, as shown in Figure 5.2.B), the threshold of the C-fiber model is lower than the stimulation with weak strength but long duration. This simulation result indicated that the anodal stimuli with stronger and shorter duration resulted in a lower PAR, benefiting C-selectivity.

Since the role of PAR has not been proved in terms of C-selectivity ever, it is a new dimension for designing effective selective stimulation. However, it is not preferable to further increase PAR because it results in either a stronger anodal stimulus, which might be limited by the highest stimulation strength for human subjects, or weaker cathodal stimulus, which could not provide sufficient power to activate C. Thus, it could be optimized based on the details of the selective stimulation.

(2) BMAC

The thresholds of both C and Aδ increase as the carrier frequency increases when stimulated by carrier waves modulated by burst waves, i.e., BSW, as shown in Figure 5.3. However, the threshold of C increased and saturates more rapidly compared with Aδ. Thus, the threshold of C is considerably reduced than Aδ. The only exception is carriers with frequencies of 100 Hz to 200 Hz, at which point the values were similar. As reported in [73], low-frequency burst-modulated waveforms (burst frequency: 20 Hz with 2-5 pulses in each burst period) can reduce the activation of Aδ even if the equivalent carrier frequency was quite low [73]. Our results in Fig. 3.4.2 showed that the effect on selective

stimulation of C increased significantly when the carrier frequency increased from 200 Hz to 1 kHz. After 1 kHz, the stimulation effect increases very slowly, and the effect is saturated at 10 kHz. Therefore, based on our simulation results, the carrier waves with higher frequency (>10 kHz) favor much more increased C-selectivity.

Comparing the results of BMAC in Figure 5.4 with the results of BSW shown in Figure 5.2, the strength of the activation threshold of both fibers to BMAC (carrier frequency set at 10 kHz) is greater due to the reduced charge because of adding carrier waves. However, the shape of the curves in Figure 5.4 is similar to that of the BSW-only case (Figure 5.2), indicating that a high-frequency carrier (>10 kHz) has no further contribution to myelinated or unmyelinated nerve fibers simulated by the Aδ-fiber and C-fiber model, respectively.

This finding partially agrees with Grill et al.'s results regarding the fact that a high-frequency carrier (>2 kHz) does not further contribute to the activation of myelinated fibers [74]. However, for the C-fiber model, when simulating unmyelinated sensory nerves, there have not been any reports on their responses to high-frequency carriers to the best of our knowledge. Through this experiment, it is clear their activation threshold is not affected by the high-frequency carrier waves when their frequency is greater than a certain hertz (approximately 1 kHz), which is similar to that of the Aδ-fiber model.

Although the increase in duration causes a reduction in the thresholds, the overall required charge did not change, as shown in Figure 5.5. Concretely, the charge of BSW at 50 Hz to activate the C-fiber model is 47.4 ms×μA/cm^2. This value is exactly the same as it of BMAC with a burst frequency of 50 Hz and carrier frequency of 10 kHz. This finding is consistent with that reported in a previous study [75], revealing that the frequency of carrier waves does not contribute to the activation of the high-frequency band because it depends on the charge required for stimulating the Aδ-fiber model. This experiment demonstrates that this notion is also true for the C-fiber model. In summary, carrier waves in the carrier frequency range (2-10 kHz) favor C-selectivity. In addition, increasing the carrier frequency beyond 10 kHz does not further improve C-selectivity.

On the other hand, the electrical properties of human tissues are frequency dependent, as shown in Gabriel's research [30]. For percutaneous electrical stimulation, high-frequency stimulation could be effective to lower the conductivity of the epidermis to reduce the current consumption at the epidermis and enhance stimulation to targeted deep layers. Therefore, although the use of BMAC to improve C-selectivity saturated after a carrier frequency of 10 kHz, the findings could be helpful to select the correct carrier waves to realize the stimulation to C in deep layers while maintain the high C-

selectivity that resulted from BSW. Future studies are needed to confirm this point.

(3) i-Aδ

The feasibility of nerve conduction block by high-frequency stimulation was first confirmed in mammalian peripheral motor nerve experiments [24, 36]. However, when using a high-frequency stimulation with low intensity (compares with conduction block), the underlying mechanism is that the open-close function of the myelinated slow K ion channel, denoted by variable *s*, is slower than that of the other channels at rest potential as shown in Fig.2.4.B, and this rate slowly returns to normal after the high-frequency stimulation ends [40]. This mechanism was first investigated for nerve selective stimulation in this study, harnessing the differential effect of high-frequency stimulation on myelinated and unmyelinated nerves to increase the threshold gap between the two nerves and thereby improving the R_{th}.

The stimuli with stronger intensity, longer duration, and lower frequency increased the value of the variable *s* as shown in Figure 5.6. However, the stimulation parameters should be carefully selected to prevent activating the myelinated nerves by the pre-pulses of the i-Aδ. Moreover, as noted in Figure 5.7, the pre-pulses could work with the main pulses, especially the asymmetric polarity of BSW and BMAC, to contribute to C-selectivity. If no clear interaction occurred between different factors contributing to C-selectivity, the final R_{th} might reflect the product of multiple factors, such as those resulting from the pre-pulse and the polarity asymmetry ratio. It could reveal this notion by the results shown in Figure 5.7. When there was no pre-pulse (the strength of the pre-pulse was 0, only-BMAC case), the quotient of the R_{th} of the stimulation with PAR of 1:1 and 1:6 was 1.669 (0.6074:0.3638). When the strength of the pre-pulse was 20 and 25 mA/cm^2 (pre-pulse with BMAC cases), the quotients were 1.688 (0.5412:0.3206) and 1.657 (0.5000:0.3018), respectively. In other words, i-Aδ and BMAC waveform influence C-selectivity independently. However, this should be further investigated by exploring the different methods to combine the pre-pulses and main pulses, e.g., beginning main pulse stimulation at different levels of the variable *s*, connecting them with the anodal or cathodal stimulus at different intervals, etc.

In Figure 5.8, according to the changes on the X-axis and Y-axis in A and B, it can be seen that the change of R_{th} on duration is smaller than that on PAR. From Figure 5.8, the result of R_{th} with duration 20 ms is consistent with the result in fig 5.4B, and the change of R_{th} caused by the asymmetry ratio increases as the duration increases. After adding the pre-pulse before the stimulus waveform, the trend caused by PAR remains consistent. However, the change in the low-duration stimulation waveform (such as 20

ms) was greater than the change in the high-duration stimulation waveform (such as 32 ms) with pre-pulse, which shortened the gap caused by the PAR.

Since the PAR affects the stimulus waveform to lower the threshold of *C*, while the frequency affects the pre-pulse to raise threshold of the myelinated *Aδ*. The mechanisms of two selectivity waves are relatively independent, thus the consistency of the trend is predictable and reasonable. However, different frequencies of pre-pulses produce different rates of change of R_{th} at different PAR. For example, the results of R_{th} were 1) PAR 1:1, 0.5283(set as 100%); 2) PAR 1:3, 0.3401(R_{th} change: 64.4%); 3) PAR 1:6, 0.3021(R_{th} change: 57.2%); 4) PAR 1:9, 0.2950(R_{th} change:55.8%) by using 10k Hz frequency pre-pulse, and 1) PAR 1:1, 0.4787(set as 100%); 2) PAR 1:3, 0.3302(R_{th} change: 69.0%); 3) PAR 1:6, 0.2982(R_{th} change: 62.3%); 4) PAR 1:9, 0.2913(R_{th} change: 60.6%) by using 100k Hz frequency pre-pulse. This difference is mainly due to the difference in the duration of cathodal stimulation. That is, the effect of pre-pulse on stimulation waveform of PAR 1:1 is greater than the effect on PAR 1:9. From the results of C and D, it is clear that the R_{th} of PAR 1:1 with longer durations is still higher than that of PAR 1:9 with lower durations. Waveforms with low PAR should be prioritized to consider. A combination of pre-pulse above 10 kHz and BMAC with PAR 1:9 should be used to selectivity stimulate the *C* without considering other constraints and limitation.

5.4.2 Nerve model dynamics

To explain the phenomenon whereby the activation threshold of unmyelinated nerves is less than that of myelinated nerves, phase portrait analysis was used based on the investigation of the time constant of different ion channel variables (Figure 5.9). The phase portrait analysis of the C-fiber model has been described in detail in the study of Fitzhugh et al. [58]. However, there have been few reports on its application to the Aδ-fiber model, especially in terms of selective nerve stimulation.

The phase portrait of the C-fiber and Aδ-fiber models in Figure 5.9 demonstrate that given the anodal stimulus, the polarization equilibrium point *e* of the C-fiber model moves downwards close to the resting static equilibrium point *d* until the two equilibrium points disappear and only the hyperpolarization equilibrium point *f* remains in the phase portrait. In this situation, the state of the nerve model should have moved towards the hyperpolarization equilibrium point, causing the nerve to activate. However, given the influence of the external anodal stimulus, the neural state remains in its current state. When the external anodal stimulation is complete, the nerve terminates its equilibrium state and moves to the only equilibrium point left. Moreover, since the time constant of the closing of the Na ion channels variable *h* shown in Figure 2.4 is

greater than the opening variable *m*, C requires a longer time to close the Na ion channel for activation.

5.5 Conclusion

In this section, to investigate the increased selectivity of C fibers over Aδ fibers and subsequent secretion of endogenous opioids, we compared three stimulation waveforms, two canonical waveforms (BSW and BMAC), and one original scheme proposed based on the nerve block mechanism using an unmyelinated nerve fiber model and a myelinated nerve fiber model that was implemented based on HH equations and MRG equations, respectively. We verified the action potential propagation and their behavior in the phase plane. The ratio between the activation threshold of C and Aδ, namely R_{th}, was used as the C-selectivity index. The results of the computational experiments showed that the polarity asymmetry ratio of BSW, the carrier frequency of BMAC, and the pre-pulses represent important factors when designing stimulation schemes for C-selectivity. Moreover, i-Aδ takes advantage of all three factors to achieve high C-selectivity. This study is an important step towards effective noninvasive chronic-pain relief.

Chapter 6

Conclusion and future work

6.1 Overview

In this study, in order to improve the selectivity of C fibers over Aδ fibers and subsequent secretion of endogenous opioids, I modified and built two mathematical models referred as HH model and MRG model that can be used to compare the activity of C fibers and Aδ fibers. Through the two models, I have studied in detail about the parameters and the mechanisms of three waveforms, BSW, BMAC and i-Aδ, used in stimulation for high C-selectivity. I summarized the methods, results and provided the contributions and limitations of this research.

6.2 Comprehensive discussion

In this study, all waveforms are analyzed in terms of phase portrait analysis and the influence of stimulus parameters. In this section, we analyzed the relationship between different stimulation waveforms by these two aspects.

1) Phase portrait analysis - the role of K ion channel

In sections 3.3.1 and 4.3.1, I used phase portrait analysis to observe the effects of anodal-first stimulation and high frequency sine stimulation on ion channel currents. For anodal-first stimulation, the opening of K ion channel of C fibers is delayed by anodal stimulation, making it easier to reach action potentials with the subsequent cathodal stimulation. The anodal stimulation does not affect the activation threshold of Aδ as much as that of C. On the other hand, with high-frequency sine stimulation, more K ion channel of the myelinated nerve are thus opened earlier, which also causes the Aδ fibers to require higher stimulation to reach the action potential. The impact and persistence of high-frequency sine stimulation on C are much smaller than that of Aδ.

As can be seen, the waveforms presented in this study all used antecedent waveforms (high frequency pre-pulse or anodal stimulation) to change the electrical characteristics of the ion channels to improve C-selectivity. Therefore, a certain continuity of facilitative effect is needed to ensure that the subsequent cathodic stimulation is under the effect. This is why it is always the K ion channel that plays a decisive role in our proposed waveforms. The fundamental reason is, as shown in Figure 2.4, the time constant of the opening parameter of the K ion channel (HH model: *n*, MRG model: *s*) is higher than the Na ion channel (*m*), so the K ion channel is not as sensitive to membrane potential changes, as another important ion channel, i.e., Na ion channel.

2) Interaction between different stimulation modes

As shown in Figure 3.8, the addition of ISI between the anodal and cathodal stimulations significantly reduces C-selectivity. Also, the suppressive effect of MRG model by pre-pulse diminishes over time from the result in Figure 4.2 and Figure 5.6. This means that both pre-pulse and anodal stimulation waveforms should be placed as close as possible to cathodal stimulation waveform to achieve the optimal stimulation effect. This limits the joint use of prep-pulse and anodal-first stimulation in a sequential way.

The time constant of the variable *s* of the MRG model is much larger than the other parameters in Figure 2.4, and its effect is relatively more persistent. Thus, the high frequency pre-pulse waveform was placed before the anodal stimulation when the two waveforms were combined, as shown in Figure 4.6 and Figure 5.8.

Compared with the results in Figure 5.8, most of the R_{th} in Figure 4.6 (4.6.B, C, D) hardly vary with the parameters such as duration and frequency. In contrast to the case when only using high frequency pre-pulse in which the optimal parameters result in adequate improvement of C-selectivity (R_{th} 0.8784 vs. 0.2099) (Figure 4.4 and Figure 5.8), in the case of pre-pulse combined with anodal-first stimulation, the optimal parameters of the high frequency pre-pulse do not change the effect of anodal-first stimulation too much because the effect was diluted by the sufficiently long cathodal stimulation. Therefore, in the waveform design, the final stimulation waveform for C-selectivity was primarily considered by using asymmetric anode first stimulation and using high frequency pre-pulse to assist.

A pre-pulse with 10 kHz frequency, 20 ms duration applied before an anodal-first stimulation with PAR 1:9 and 32 ms duration could lead to a 25.5% change in R_{th} (0.2819 -> 0.2099).

6.3 Contributions and limitations

6.3.1 Contribution

The ultimate goal of our study is to selectively stimulate unmyelinated C near the sarcolemma with surface electrodes. In this study, potential stimulation waveforms were explored by investigating their threshold compared with myelinated Aδ and the dynamic behavior of the unmyelinated and myelinated nerve models responding to the stimuli from a point source near the two nerves. The major contributions of the study are summarized as follows.

1) By investigating the simulation model responses of two types of nociceptive nerve fibers in a phase plane and their ion currents, the effectiveness of anodal-first

stimulation for C-selectivity and its ion channel mechanism were clarified for the first time in this research area. Biphasic square waves are not just for charge balancing; with appropriate intensity and duration of anodal stimuli, they could significantly reduce the K^+ ion current flowing out through the membrane and thus lower the threshold strength of C. Moreover, by using the index for C-selectivity, R_{th}, and index in the phase plane, Δd_int and Δd_sep (Figure 3.2), it was clear that, for the polarity asymmetric pulses, the intensity of the anodal stimulus is a more important factor than its duration, though a specific duration of the anodal stimulus is necessary to guarantee C-selectivity.

2) The effects of the critical parameters for continuous periodic biphasic stimulation on C-selectivity over Aδ were first investigated. The parameters include frequency, duration, ISI, and polarity asymmetry ratio (PAR). The landscape of the solution space of stimulation for high C-selectivity was made clear. Specifically, the PAR was first identified and explored as a new dimension to design stimulation waveforms for C-selectivity. For symmetric polarity stimulation, 20 Hz is the best frequency for C-selectivity. Lower PARs are better for C-selectivity in terms of both R_{th} and K^+ ion currents.
3) For the stimulation with high frequency carrier wave (BMAC), a frequency band of carrier waves that improve C-selectivity was identified thorough investigations of the different carrier frequency-threshold characteristics of C and Aδ. The result is partially consistent with relevant studies on MRG in the literature. Regarding the effect of carrier frequency on C, our study is the first attempt to investigate these effects compared with Aδ to the best of our knowledge.
4) The feasibility of high-frequency stimulation, which was first confirmed by effective nerve conduction block in a mammalian peripheral motor nerve experiment [36], was first investigated for selective nerve stimulation in this study. It was demonstrated that high-frequency pre-pulse stimulation inhibits the activation of Aδ by increasing the value of the variable *s*, which plays a key role in the MRG model and can be used to design pre-pulses and its junction with main pulses. The mechanism was demonstrated by applying phase portrait analysis to both the HH and MRG models.

6.3.2 Limitations

In addition to contributions, limitations were noted.

1) Since the ultimate goal is to realize selective surface stimulation, the influence of skin should be taken into consideration. The effect of wave conduction from the

skin surface to deep layers and multiple factors affecting nerve activation and selectivity in actual stimulation cases, such as the distribution of free endings and nerve fibers, nerve fiber radius, and tissue morphology near the stimulation area, have not been investigated. This work is beyond the scope of this paper but needs to be clarified in the near future. Moreover, the influences of polarity asymmetric biphasic stimulation and high frequency sine pre-pulse on nerves and tissues other than C and Aδ were not apparent but must be considered and reflected in the simulation models. In another parallel study, a multilayer FEM (finite element method) transmission model was developed to study the effects of surface electrodes and various tissues on deep stimulation to ensure the possibility of surface stimulation in promoting the secretion of endogenous opioids. In the near future, the transmission model will be combined with the nerve fiber models of this study to verify the safety and effects of surface stimulation with different parameters.

2) The safety issue should be reconsidered. Studies have demonstrated that when a mammalian unmyelinated nerve is stimulated with an intensity several times its threshold, the nerve will lose its response [75], which clearly revealed the upper limit of unmyelinated nerve stimulation. The stimulation parameters should be optimized under this constraint.
3) The findings from the simulation study need to be carefully verified and further validated. Close cooperation with both subjective questionnaires and objective evaluations, such as studies on pain-related electrical stimulation-evoked electroencephalograms, is crucial [76].

6.4 Future work

In this study, the optimal solution for each potential stimulation waveform has been investigated. The combination of the facilitative factors of each two waveforms was explored too, though the C-selectivity can be improved further, the charge accumulation within a certain short period of time has not been sufficiently analyzed, which remains as safety issue. Moreover, in future, stimulation waveforms that integrate all the facilitative factors, i.e., anodal stimulation, high frequency sine pre-pulse, and high frequency carrier waves could be investigated too. In that case, the safety issues need to be carefully discussed.

In addition, in order to make sure the C-selectivity of percutaneous stimulation, the transmission of current from surface electrodes to the targeted nerves is necessary. Since a transmission model is being developed in our research group, in the future, we

need to combine current study with the transmission model to develop a complete simulation tool for clinically achievable stimulation with high C-selectivity.

6.5 Conclusion

In Chapter 3, I focused on the effect of anodal-first stimulus and polarity asymmetry ratio, and their mechanism, so as to identify the waveforms that can reduce the threshold strength of C. In chapter 4, I describe a high frequency sine pre-pulse proposed to increase the threshold of Aδ fibers, and its ion mechanism. And in chapter 5, I studied the carrier wave, which can increase the penetration depth of surface stimulation to the deep tissue stimulation.

I found the optimal parameters for anodal-first stimulus and high frequency sine pre-pulse in Chapter 3 and 4, respectively. Moreover, I combined these two waveforms with the high frequency carrier wave to find the parameters of carrier wave that does not reduce the facilitative effect of C-selectivity. Also, I discussed the optimal solution under the combined conditions of the two waveforms. Currently, in order for this study to be implemented clinically, it also needs further verification in terms of a lot of aspects such as safety. However, I believe that this study is an important step towards effective noninvasive chronic-pain relief.

Reference

1. Raja S. N., et al. "The revised International Association for the Study of Pain definition of pain: concepts, challenges, and compromises." Pain 161.9, pp. 1976-1982, 2020.
2. Apkarian A. V., Javeria A. Hashmi, and Marwan N. B. "Pain and the brain: specificity and plasticity of the brain in clinical chronic pain." Pain, vol. 152, no. 3 Suppl, pp. S49-S64, Mar. 2011.
3. Hattori S. “The prevalence of chronic pain in Japan." Folia Pharmacologica Japonica, vol. 127, no. 3, pp. 176-180, 2006.
4. Andrews P., Steultjens M., and Riskowski J. "Chronic widespread pain prevalence in the general population: a systematic review." European Journal of Pain 22.1, pp. 5-18, 2018.
5. Yabuki S., et al. "A Nationwide Survey of Chronic Pain Sufferers in Japan." Pain in japan. 2010
6. Breivik H., et al. "Survey of chronic pain in Europe: prevalence, impact on daily life, and treatment." European journal of pain, vol. 10, no. 4, pp. 287-287, Jan. 2006.
7. Murakawa K., et al. "Concept of Chronic Pain (Special Feature: Chronic Pain Treatment Guide)--(what is chronic pain)." The Journal of therapy, 90.7, pp. 2046-2051, 2008.
8. Koop L. K., and Prasanna T. "Neuroanatomy, Sensory Nerves." Apr. 2019.
9. https://academic-master.com/nervous-system/, As of July 11, 2021
10. Barnett M. W., and Philip M. L. "The action potential." Practical neurology, vol. 7, no.3 pp. 192-197, 2007.
11. https://teachmephysiology.com/nervous-system/synapses/action-potential/, As of July 19, 2021
12. Broderick J. E., et al. "Cognitive behavioral therapy for chronic pain is effective, but for whom?" Pain, vol. 157, no. 9, pp. 2115-2123, 2016.
13. Melzack R., and Wall P. D. "Pain mechanisms: a new theory." Science, vol.150, no. 3699, pp. 971-979, Nov. 1965.
14. Martell B. A., et al. "Systematic review: opioid treatment for chronic back pain: prevalence, efficacy, and association with addiction." Annals of internal medicine, vol.146, no. 2, pp. 116-127, Jan. 2007.
15. Stoeber M., et al. "A genetically encoded biosensor reveals location bias of opioid drug action." Neuron, vol. 98, no. 5, pp. 963-976, Jun. 2018.
16. Ali U., et al. "Acupuncture/Electroacupuncture as an Alternative in Current Opioid

Crisis." Chinese journal of integrative medicine, pp. 1-5, Oct. 2019.

17. Li H., et al. "Electroacupuncture decreases Netrin-1-induced myelinated afferent fiber sprouting and neuropathic pain through μ-opioid receptors." Journal of pain research, vol.12, pp. 1259-1268, Apr. 2019.
18. Martin-Schild S., et al. "Endomorphin-2 is an endogenous opioid in primary sensory afferent fibers." Peptides, vol. 19, no. 10, pp. 1783-1789, 1998.
19. Plaghki L., and Mouraux A. "How do we selectively activate skin nociceptors with a high power infrared laser? Physiology and biophysics of laser stimulation." Neurophysiologie Clinique/Clinical Neurophysiology, vol. 33, no.6, pp. 269-277, Dec. 2003.
20. Churyukanov M., et al. "Thermal detection thresholds of Aδ-and C-fibre afferents activated by brief CO2 laser pulses applied onto the human hairy skin." PloS one, vol. 7, no. 4, e35817, Apr. 2012.
21. Chen X., and Han J. "Analgesia induced by electroacupuncture of different frequencies is mediated by different types of opioid receptors: another cross-tolerance study." Behavioural brain research, vol. 47, no. 2, pp. 143-149, Apr. 1992.
22. Han J. "Acupuncture: neuropeptide release produced by electrical stimulation of different frequencies." Trends in neurosciences, vol. 26, no. 1, pp. 17-22, Jan. 2003.
23. Radhakrishnan R., and Kathleen A. S. "Deep tissue afferents, but not cutaneous afferents, mediate transcutaneous electrical nerve Stimulation–Induced antihyperalgesia." The Journal of Pain, vol. 6, no. 10, pp. 673-680, Oct. 2005.
24. Sorkin L. S., and Wallace M. S. "Acute pain mechanisms." Surgical Clinics of North America, vol. 79, no. 2, pp. 213-229, Apr. 1999.
25. Grill W. M., and Mortimer J. T. "Inversion of the current-distance relationship by transient depolarization." IEEE Transactions on Biomedical Engineering, vol. 44, no. 1, pp. 1-9, Jan. 1997.
26. Grill W. M., and Mortimer J. T. "Stimulus waveforms for selective neural stimulation." IEEE Engineering in Medicine and Biology Magazine, vol. 14, no. 4, pp. 375-385, Jul. 1995.
27. Goats G. C. "Interferential current therapy." British journal of sports medicine 24.2, pp. 87, 1990.
28. Pitei D. L., et al. "The value of the Neurometer in assessing diabetic neuropathy by measurement of the current perception threshold." Diabetic Medicine, vol.11, no. 9, pp. 872-876, Nov. 1994.
29. Ward A. R., and Shkuratova N. "Russian electrical stimulation: the early experiments." Physical therapy, vol. 82, no. 10, pp. 1019-1030, Oct. 2002.

30. Gabriel C. Compilation of the dielectric properties of body tissues at RF and microwave frequencies. KING'S COLL LONDON (UNITED KINGDOM) DEPT OF PHYSICS, 1996.
31. Koga K., et al. "Selective activation of primary afferent fibers evaluated by sine-wave electrical stimulation." Molecular Pain, vol.1, no. 1, pp. 13, Mar. 2005.
32. Dufour A., et al. "On the selective activation of unmyelinated C-fibers using sinusoidal electrical stimulation: an ERP study." Clinical Neurophysiology, vol.122, no. 5: pp. 1042-1047, May. 2011.
33. Harris G. W., Manabe Y., and Ruf K. B. "A study of the parameters of electrical stimulation of unmyelinated fibres in the pituitary stalk." The Journal of physiology, vol. 203, no. 1, pp. 67-81, Jul. 1969.
34. Bostock H., Cikurel K., Burke D. Threshold tracking techniques in the study of human peripheral nerve. Muscle & Nerve: Official Journal of the American Association of Electrodiagnostic Medicine. 21(2), pp. 137-158, 1998.
35. Ranjan R., et al. "Mechanism of anode break stimulation in the heart." Biophysical journal, vol. 74, no. 4, pp. 1850-1863, Apr. 1998.
36. Bhadra N., and Kevin L. K. "High-frequency electrical conduction block of mammalian peripheral motor nerve." Muscle & Nerve: Official Journal of the American Association of Electrodiagnostic Medicine, vol. 32, no. 6, pp. 782-790, Aug. 2005.
37. Schoenbach K. H., et al. "The effect of pulsed electric fields on biological cells: Experiments and applications." IEEE transactions on plasma science, vol. 25, no. 2, pp. 284-292, Apr. 1997
38. Hodgkin A. L., and Huxley A. F. "A quantitative description of membrane current and its application to conduction and excitation in nerve." The Journal of physiology, vol. 117, no. 4, pp. 500-544, Aug. 1952.
39. Best E. N. "Null space in the Hodgkin-Huxley Equations. A critical test." Biophysical journal, vol. 27, no. 1, pp. 87-104, Jul. 1979.
40. Dean D., and Lawrence P. D. "Application of phase analysis of the Frankenhaeuser-Huxley equations to determine threshold stimulus amplitudes." IEEE transactions on biomedical engineering, vol. BME-30, no. 12, pp. 810-818, Dec. 1983.
41. Stein R. B., and Pearson K. G. "Predicted amplitude and form of action potentials recorded from unmyelinated nerve fibres." Journal of theoretical biology, vol. 32, no. 3, pp. 539-558, Sep. 1971.
42. Pinto R. D., et al. "Synchronous behavior of two coupled electronic neurons." Physical Review E, vol.62, no. 2, pp. 2644, Aug. 2000.

43. Krouchev N. I., et al. "From squid to mammals with the HH model through the Nav channels' half-activation-voltage parameter." PloS one, vol. 10, no. 12, e0143570, Dec. 2015.
44. Bekkouche B. "Functional Implications from Changes in Volume and Periaxonal Space of C-fibers.", 2012.
45. Bhadra N., et al. "Simulation of high-frequency sinusoidal electrical block of mammalian myelinated axons." Journal of computational neuroscience, vol. 22, no. 3, pp. 313-326, Jan. 2007.
46. Tarotin I., Aristovich K., and Holder D. "Model of impedance changes in unmyelinated nerve fibers." IEEE Transactions on Biomedical Engineering, vol. 66, no. 2, pp. 471-484, Feb. 2019.
47. Frankenhaeuser B., and Huxley A. F. "The action potential in the myelinated nerve fibre of Xenopus laevis as computed on the basis of voltage clamp data." The Journal of Physiology, vol. 171, no. 2: pp. 302-315, Jun. 1964.
48. McIntyre C. C., Richardson A. G., and Grill W. M. "Modeling the excitability of mammalian nerve fibers: influence of afterpotentials on the recovery cycle." Journal of neurophysiology, vol. 87, no. 2, pp. 995-1006, Feb. 2002.
49. Sweeney J. D., Mortimer J. T., and Durand D. "Modeling of mammalian myelinated nerve for functional neuromuscular stimulation." IEEE 9th Annual Conference of the Engineering in Medicine and Biology Society, vol. 3, 1987.
50. Bourbeau D. J., et al. "A computational model for estimating recruitment of primary afferent fibers by intraneural stimulation in the dorsal root ganglia." Journal of neural engineering, vol. 8, no. 5, pp. 056009, Aug. 2011.
51. Åström M., et al. "Relationship between neural activation and electric field distribution during deep brain stimulation." IEEE Transactions on Biomedical Engineering, vol. 62, no. 2, pp.664-672, Feb. 2015.
52. Gaines J. L., et al. "A model of motor and sensory axon activation in the median nerve using surface electrical stimulation." Journal of computational neuroscience, vol. 45, no. 1, pp. 29-43, Jun. 2018.
53. Wongsarnpigoon A., Woock J. P., and Grill W. M. "Efficiency analysis of waveform shape for electrical excitation of nerve fibers." IEEE Transactions on Neural Systems and Rehabilitation Engineering, vol. 18, no. 3, pp. 319-328, Jun. 2010.
54. Otsuru N., et al. "Selective stimulation of C fibers by an intra-epidermal needle electrode in humans." Open Pain J, vol. 2, no.1, pp. 53-56, Oct. 2009.
55. Koslow M., Bak A., and Li C. L. "C-fiber excitability in the cat." Experimental neurology, vol. 41, no. 3, pp. 745-753, Dec. 1973.

56. McNeal D. R. "Analysis of a model for excitation of myelinated nerve." IEEE Transactions on Biomedical Engineering, vol. BME-23, no. 4, pp. 329-337, Jul. 1976.
57. Li C. L., and Bak A. "Excitability characteristics of the A-and C-fibers in a peripheral nerve." Experimental neurology 50.1: 67-79, 1976.
58. Fitzhugh R. "Thresholds and plateaus in the Hodgkin-Huxley nerve equations." The Journal of general physiology, vol.43, no. 5, pp. 867-896, May. 1960.
59. He S., et al. "Gate Mechanism and Parameter Analysis of Anodal-First Waveforms for Improving Selectivity of C-Fiber Nerves." Journal of Pain Research. 14, pp. 1785, 2021.
60. He S., Yoshida Y., Tripanpitak K., Takamatsu S., Huang S. Y., Yu W. A simulation study on selective stimulation of C-fiber nerves for chronic pain relief. IEEE Access. 2020.
61. Pereira P., Leote J., Cabib C., Casanova-Molla J., Valls-Sole J. Stimulus waveform determines the characteristics of sensory nerve action potentials. Clinical Neurophysiology. 127(3), pp. 1879-1885, 2016.
62. Therimadasamy A., Chan Y. C., Wilder-Smith E. P. Skin receptors and intradermal nerves do not generate the sensory double peak. Muscle & Nerve. 52(1), pp. 103-106, 2015.
63. Aprile I., Tonali P., Stalberg E., et al Double peak sensory responses: effects of capsaicin. Neurological Sciences. 28(5), pp. 264-269, 2007.
64. Aprile I., Tonali P., Stalberg E., Di Stasio E., Caliandro P., Foschini M., Padua L. Double peak sensory responses at submaximal stimulation. Clinical neurophysiology. 114(2), pp. 256-262, 2003.
65. Boyd I. A., Kalu K. Scaling factor relating conduction velocity and diameter for myelinated afferent nerve fibres in the cat hind limb. The Journal of physiology. 289(1), pp. 277-297, 1979.
66. Ranjan R., Chiamvimonvat N., Thakor N. V., Tomaselli G. F., Marban E. Mechanism of anode break stimulation in the heart. Biophysical journal. 74(4), pp. 1850-1863, 1998.
67. Mallik A., Weir A. I. Nerve conduction studies: essentials and pitfalls in practice. Journal of Neurology, Neurosurgery & Psychiatry. 76(suppl 2), pp. ii23-ii31, 2005.
68. Merrill D. R., Bikson M., Jefferys J. G. Electrical stimulation of excitable tissue: design of efficacious and safe protocols. Journal of neuroscience methods. 141(2), pp. 171-198, 2005.
69. Grill W. M., Veraart C., and Mortimer J. T. "Selective activation of peripheral nerve fascicles: use of field steering currents." Proceedings of the Annual International

Conference of the IEEE Engineering in Medicine and Biology Society, Vol. 13, no. 1991, Nov. 1991.

70. Mohamed M. A., Islas J. F., Schwartz R. J., Birla R. K. Electrical Stimulation of Artificial Heart Muscle: a look into the electrophysiological and genetic implications. ASAIO journal (American Society for Artificial Internal Organs: 1992). 63(3), pp. 333, 2017.
71. Dudel J., Schmidt R. F., Thews G. Human physiology. 1983.
72. IEC 60364-7-710-Electrical installations of buildings−Part 7-710: Requirements for special installations or locations−Medical locations, 2002.
73. Qing K. Y., Ward M. P., and Irazoqui P. P. "Burst-modulated waveforms optimize electrical stimuli for charge efficiency and fiber selectivity." IEEE Transactions on Neural Systems and Rehabilitation Engineering, vol. 23, no. 6, pp. 936-945, Nov. 2015.
74. Medina L. E., and Grill W. M. "Nerve excitation using an amplitude-modulated signal with kilohertz-frequency carrier and non-zero offset." Journal of neuroengineering and rehabilitation, vol. 13, no. 1, Jul. 2016.
75. Maclver M. B., and Tanelian D. L. "Structural and Functional Specialization of A6 and C Fiber Free Nerve Endings Innervating Rabbit Cornea1 Epithelium." The Journal of Neuroscience, vol. 13, no. 10, pp. 4511-4524, Oct. 1993.
76. Tripanpitak K., Viriyavit W., Huang S. Y., Yu W. Classification of Pain Event Related Potential for Evaluation of Pain Perception Induced by Electrical Stimulation. Sensors. 20(5), pp. 1491, 2020.